

PIEZOELECTRIC ENERGY HARVESTING DEVICES FOR LOW
FREQUENCY VIBRATION APPLICATIONS

Except where reference is made to the work of others, the work described in this dissertation is my own or was done in collaboration with my advisory committee. This dissertation does not include proprietary or classified information.

Dongna Shen

Certificate of Approval:

Zhongyang Cheng
Associate Professor
Materials Engineering

Dong-Joo Kim, Chair
Associate Professor
Materials Engineering

Barton C. Prorok
Associate Professor
Materials Engineering

Song-Yul Choe
Associate Professor
Mechanical Engineering

George T. Flowers
Dean
Graduate School

PIEZOELECTRIC ENERGY HARVESTING DEVICES FOR LOW
FREQUENCY VIBRATION APPLICATIONS

Dongna Shen

A Dissertation

Submitted to

the Graduate Faculty of

Auburn University

in Partial Fulfillment of the

Requirements for the

Degree of

Doctor of Philosophy

Auburn, Alabama
May 9, 2009

PIEZOELECTRIC ENERGY HARVESTING DEVICES FOR LOW
FREQUENCY VIBRATION APPLICATIONS

Dongna Shen

Permission is granted to Auburn University to make copies of this dissertation at its discretion, upon request of individuals or institutions and at their expense. The author reserves all publication rights.

Signature of Author

Date of Graduation

VITA

Dongna Shen, daughter of Shishui Shen and Shuzhen Wang, was born on January 11, 1977, in Beijing, P. R. China. She attended Beijing University of Technology (formerly known as Beijing Polytechnic University) in August 1995 and graduated with a Bachelor of Engineering degree and a Master of Engineering degree in Materials Science and Engineering in 2000 and 2003. She joined Auburn University in August 2004 to pursue her doctoral degree in Materials Engineering and started her second master degree in Probability and Statistics in January 2007. She married Kai Xu, son of Fengliang Xu and Zhaohong Fang and has one child, Alex Xu.

DISSERTATION ABSTRACT

PIEZOELECTRIC ENERGY HARVESTING DEVICES FOR LOW
FREQUENCY VIBRATION APPLICATIONS

Dongna Shen

Doctor of Philosophy, May 9, 2009
(M.S., Beijing University of Technology, 2003)
(B.S., Beijing University of Technology, 2000)

194 Typed Pages

Directed by Dong-Joo Kim

Energy harvesting, a process of capturing ambient waste energy and converting it into usable electricity, has been attracting more and more researchers' interest because of the limitations of traditional power sources, the increasing demands upon mobile devices such as wireless sensor networks, and the recent advent of the extremely low power electrical and mechanical devices such as microelectromechanical systems (MEMS).

In this research, bulk- and wafer-scale of piezoelectric power generator prototypes were developed.

The Lead Zirconate Titanate (PZT) bimorph cantilever in bulk scale with a big proof mass at the free end tip was studied to convert ambient vibration energy of 100 Hz and above 1g ($1g = 9.81 \text{ m/s}^2$) acceleration amplitudes. The optimal design was based on matching the resonant frequency of the device with the environmental exciting frequency, and balancing the power output and the fracture safety factor. The fabricated PZT power generator with an effective volume of 0.0564 cm^3 and a safety factor of 10g can produce $6.21 \text{ V}_{\text{pk}}$, $257 \text{ }\mu\text{W}$, or $4558 \text{ }\mu\text{W}/\text{cm}^3$ with an optimal resistive load of $75 \text{ k}\Omega$ from 1g acceleration at its resonant frequency of 97.6 Hz. To overcome the high fragility of PZT, substitute piezoelectric materials, Macro Fiber Composite (MFC) and polyvinylidene fluoride (PVDF), and alternative operational ambient for power generators were investigated for high vibration amplitude applications.

Before fabricating piezoelectric power generators in wafer scale, interlayer effects on the properties of PZT thin film were surveyed. The fabricated device based on Si wafer, with a beam dimension about $4.800 \text{ mm} \times 0.400 \text{ mm} \times 0.036 \text{ mm}$ and an integrated Si mass dimension about $1.360 \text{ mm} \times 0.940 \text{ mm} \times 0.456 \text{ mm}$ produced $160 \text{ mV}_{\text{pk}}$, $2.13 \text{ }\mu\text{W}$, or $3272 \text{ }\mu\text{W}/\text{cm}^3$ with the optimal resistive load of $6 \text{ k}\Omega$ from 2g acceleration at its resonant frequency of 461.15 Hz.

To precisely control the resonant frequency of the power generator, Si on insulator (SOI) wafer substitutes for Si wafer. The resonant frequency of the fabricated device is as low as about 184 Hz. The difference between the calculated and measured resonant frequency has been decreased to 4.25%.

ACKNOWLEDGEMENTS

I would like to express my deepest gratitude to my major advisor, Dr. Dong-Joo Kim, for his complete support and guidance throughout my graduate career. I warmly appreciate his passion, patience and kindness that have made working at Auburn University a truly pleasure.

I would also like to extend my thanks to my advisory committee members, Dr. Zhongyang Cheng, Dr. Barton C. Prorok, and Dr. Song-Yul Choe for their important suggestions and kindly help. Thanks are also due to Dr. Bryan A. Chin, Dr. Alex Simonian, and Dr. Jeffrey Fergus for their kindly support.

I appreciate my colleagues and friends who have helped and collaborated with me: Dr. Howard C. Wikle, L.C. Mathison, Roy Howard, Charles Ellis, Jung-hyun Park, Sang H. Yoon, Jyoti Ajitsaria, Jung-Gi Lee, Shichu Huang, Dan Liu, and others too many to mention, for their long-term support and kindly help. A special thank I would like to extend to Jung-hyun Park, Ph.D. candidate, for his help throughout my research.

Finally, I would like to thank my dearest husband, my son, my parents, my grandparents, my brother, my sister in law, my nephew, my parents in law, and all other family members for their support and love throughout my graduate career.

Style manual or journal used:

IEEE

Computer software used:

Microsoft Word 2007, Excel 2007, PowerPoint 2007, Visio 2007,
OriginPro7.5, Endnote X, Peakfitting™

TABLE OF CONTENTS

LIST OF FIGURES	xiii
LIST OF TABLES	xvii
CHAPTER 1	
INTRODUCTION	1
1.1 Motivation—an overview of the problem.....	1
1.2 A potential solution—energy harvesting	3
1.2.1 Energy harvesting	3
1.2.2 Potential energy harvesting sources.....	4
1.3 Research objective and dissertation structure	11
1.3.1 Research objective	11
1.3.2 Dissertation structure	12
References.....	14
CHAPTER 2	
GENERAL BACKGROUND.....	18
2.1 Theoretical foundations	18
2.1.1 Piezoelectricity.....	18
2.1.2 Piezoelectric materials	22
2.2 Piezoelectric power generator.....	25
2.3 Literature review on piezoelectric power generator	28
2.3.1 Bulk scale Piezoelectric Power Generators (PPG)	28
2.3.2 Piezoelectric Micro Power Generator (PMPG)	38
References.....	44

CHAPTER 3

DESIGN, OPTIMIZATION AND DEMONSTRATION OF BULK PROTOTYPES....	50
3.1 Material selection, configuration design, analytical modeling, and dimension optimization	50
3.1.1 Material selection and configuration design	50
3.1.2 Analytical modeling and optimization on the dimension of bulk PZT prototype	53
3.1.2.1 Analysis on the resonant frequency of the piezoelectric cantilever.....	54
3.1.2.2 Analysis on the output power of the piezoelectric cantilever	60
3.1.2.3 Analysis on the safety factor and the dimension optimization of the piezoelectric cantilever	64
3.2 Experimental setup and measurement	68
3.3 Results and discussion	71
3.4 Chapter summary	82
References.....	83

CHAPTER 4

DESIGN, INVESTIGATION AND COMPARISON OF BULK PROTOTYPES MADE OF OTHER MATEIRALS	84
4.1 Introduction.....	84
4.2 Material selection and experimental procedure	86
4.2.1 Material selection.....	86
4.2.2 Prototype fabrication and evaluation	88
4.3 Results and discussion	89
4.4 Chapter summary	103
References.....	104

CHAPTER 5

SAFETY FACTOR IMPROVEMENT FOR HIGH AMPLITUDE VIBRATION

APPLICATION	105
5.1 Mechanical behavior of a cantilever in a fluid.....	106
5.2 Experimental setup and measurement	107
5.3 Results and discussion	108
5.4 Chapter summary	113
References.....	114

CHAPTER 6

DESIGN AND DEMONSTRATION OF MEMS-SCALE POWER GENERATOR

PROTOTYPES BASED ON A SI WAFER.....	115
6.1 Substrate effects on sol-gel PZT thin film	115
6.2 Device design and fabrication.....	122
6.2.1 Device design.....	122
6.2.2 Device fabrication and equipment	126
6.3 Evaluation and measurement	131
6.4 Results and discussion	132
6.4.1 Designed mask and fabricated PZT micro power generators	132
6.4.2 Property of PZT thin film and power output of PZT micro power generators	134
6.4.3 Comparison with other published MEMS energy harvesting devices.....	142
6.5 Chapter summary	144
References.....	145

CHAPTER 7

DEMONSTRATION OF MEMS-SCALE PZT POWER GENERATOR PROTOTYPES BASED ON A SOI WAFER

149	
7.1 Introduction.....	149
7.2 Device design, fabrication flow, and measurement	152
7.2.1 Device design.....	152

7.2.2 Device fabrication flow.....	153
7.2.3 Device measurement.....	155
7.3 Results and discussion	156
7.4 Chapter summary	166
References.....	167
CHAPTER 8	
CONCLUSIONS AND FUTURE WORK.....	168
8.1 Conclusions.....	168
8.2 Future work.....	169
8.2.1 Power output improvement.....	169
8.2.2 Safety factor improvement.....	170
References.....	171
APPENDIX A.....	172
APPENDIX B.....	175
APPENDIX C.....	177

LIST OF FIGURES

1- 1	Architecture of a sensor node.	2
1- 2	Comparison of the output power density and the lifetime among battery, solar and vibration energy sources [18].....	6
1- 3	Schematic diagrams of the three types of electromechanical transducers: (a) electrostatic; (b) electromagnetic; (c) piezoelectric.....	8
2- 1	A rectangular cantilever in a Cartesian coordinate system.....	21
2- 2	Atomic structure of PZT at MPB.....	24
2- 3	Phase graph of PZT.....	25
2- 4	Working modes of piezoelectric power harvester.	26
2- 5	Configuration of a bimorph power harvester.....	27
2- 6	Operations of two-layer cantilever power harvester.....	28
2- 7	Schematic diagram of the bulk piezoelectric generator [11].	29
2- 8	Shoe insert power generator in two positions: PZT dimorph and PVDF stave [28].	32
2- 9	QuickPack® Actuator [44].	36
2- 10	Schematic diagram of a thick-film piezoelectric micro-generator [57].....	39
3- 1	Schematic diagrams of three common configurations (a) diaphragm (b) bridge (c) cantilever of piezoelectric power harvester.	51
3- 2	(a) Picture of bimorph cantilever bender; (b) schematic diagram of the layer structure of bimorph cantilever bender [1].	52
3- 3	Schematic diagram of bimorph cantilever configuration and notations.	53
3- 4	Resonant frequency as a function of lengths of PZT and proof mass in the dimensions of cantilever beam.....	57
3- 5	Resonant frequency as a function of thicknesses of PZT and shim in the dimensions of cantilever beam.....	58
3- 6	Resonant frequency as a function of PZT width and height of proof mass in the dimensions of cantilever beam.....	59
3- 7	Schematic diagram of the electronic equivalent circuit.....	60

3- 8	Power density as a function of lengths of PZT and proof mass in the dimensions of cantilever beam.....	62
3- 9	Power density as a function of thicknesses of PZT and shim in the dimensions of cantilever beam.....	63
3- 10	Power density as a function of PZT width and height of proof mass in the dimensions of cantilever beam.....	63
3- 11	Safety factor as a function of lengths of PZT and proof mass in the dimensions of cantilever beam.....	66
3- 12	Safety factor as a function of thicknesses of PZT and shim in the dimensions of cantilever beam.....	67
3- 13	Safety factor as a function of PZT width and height of proof mass in the dimensions of cantilever beam.....	68
3- 14	Picture of Impedance analyzer 4294A (Agilent Technologies).....	69
3- 15	(a) Schematic diagram and (b) picture of experimental setup with a simple resistive load.....	70
3- 16	Picture of the optimized PZT cantilever prototype.....	72
3- 17	Measured resonant frequency of the optimized PZT bulk prototype.....	73
3- 18	Output peak voltage and power vs. the resistive load.....	74
3- 19	AC voltage output at (a) 1g (b) 3g and (c) 5g acceleration amplitudes vs. vibration frequency.....	76
3- 20	Peak voltages obtained from the AC voltage output and the average power vs. vibration frequency at different acceleration amplitudes.....	77
3- 21	Power density and voltage vs. vibration frequency of the PZT prototype.....	78
3- 22	Peak frequency of the bulk PZT power generator prototype vs. acceleration amplitude.....	79
3- 23	Comparison of power output between experiment and calculation at different acceleration amplitudes.....	81
3- 24	Measured and calculated power vs. the square of acceleration amplitude.....	82
4- 1	Comparison of AC output before and after damage of PZT prototype.....	85
4- 2	Three types of piezoelectric transducers [2-4].....	86
4- 3	Picture of fabricated prototypes using three types of piezoelectric materials.....	89
4- 4	Measured resonant frequencies of devices from three types of piezoelectric materials.....	90
4- 5	Optimal resistive loads of three prototypes: (a) PZT, (b) PVDF, and (c) MFC... ..	92
4- 6	Power density and peak voltage of (a) PZT, (b) PVDF, and (c) MFC vs. current density obtained using various external resistors.....	94

4- 7	Output voltage waveforms of three piezoelectric devices as a function of vibration frequency.....	96
4- 8	Power density and voltage of prototypes at (a) 1g, (b) 3g, and (c) 5g vs. vibration frequency.....	98
4- 9	Estimation on the output voltage and power density of PVDF and MFC prototypes at high-g vibration conditions.	102
5- 1	(a) Picture of the device and (b) schematic diagram of the device submerged in Si oil (not to scale).	107
5- 2	Measured resonant frequency of cantilever in air and in Si oil.	109
5- 3	Damping ratio in air and Si oil vs. the exciting vibration acceleration.....	111
5- 4	Power output in air and Si oil vs. the exciting vibration frequency.....	112
6- 1	Hillock generation between bottom and top electrode (Pt) layers [27].	120
6- 2	Schematic diagram of the side view of a MEMS piezoelectric power harvesting device.	121
6- 3	Schematic diagram and notations of the simplified configuration of a piezoelectric power harvesting device.	122
6- 4	Schematic diagram used to calculate the maximum stress in PZT film.	124
6- 5	Fabrication flow chart: (a) multilayer deposition; (b) top electrode patterning by liftoff (mask 1) (c) bottom electrode opening via RIE (mask 2) (d) cantilever patterning by RIE (mask 3) (e) proof mass patterning and cantilever release via backside RIE (mask 4).	128
6- 6	PZT thin film deposition flow chart.....	129
6- 7	TF analyzer 2000 measurement system (axiACCT).....	131
6- 8	SEM pictures of a fabricated PZT cantilever energy harvesting device: (a) front side; (b) back side.	133
6- 9	Piezoelectric hysteresis loop measured from the wire-bonded PZT cantilever device.	135
6- 10	Measured impedance and phase angle of the PZT cantilever vs. frequency.	136
6- 11	AC output at 1g vibration with a 6 k Ω resistive load.	137
6- 12	(a) Peak voltage and (b) average power vs. resistive load.....	139
6- 13	(a) peak voltage (b) average power vs. vibration frequency.....	141
6- 14	Damping ratio increases with acceleration amplitude.	142
7- 1	Schematic diagram of the side view of a piezoelectric energy harvesting cantilever based on a SOI wafer.	153
7- 2	SEM pictures of a cantilever (a) front and (b) back side 45 $^{\circ}$ view fabricated on a SOI wafer.....	157

7- 3	Piezoelectric hysteresis loop measured from the wire-bonded PZT cantilever device.	159
7- 4	Measured impedance and phase angle of the PZT cantilever vs. frequency.	160
7- 5	(a) Peak voltage and (b) average power vs. resistive load at 0.50, and 0.75g acceleration amplitudes.	162
7- 6	Peak voltage and average power vs. current at (a) 0.50, and (b) 0.75g acceleration amplitudes.	1644
7- 7	(a) Peak voltage and (b) average power vs. exciting vibration frequency at 0.50, and 0.75g acceleration amplitudes.	165

LIST OF TABLES

1. 1	Power density comparison of ambient energy sources.	5
1. 2	Peak frequency and acceleration amplitude of various vibration sources [18, 20-23].	7
1. 3	Comparison of three types of transducers [18, 44].	10
2. 1	Relationship between tensor notations and compressed matrix notations.	20
2. 2	Properties of some piezoelectric materials.	23
2. 3	Summary among current PMPG.	43
3. 1	Dimensions and frequency of the optimized PZT bulk power generator prototype with a safety factor over 10.	72
4. 1	Characteristic comparison among three types of piezoelectric materials.	87
4. 2	Finally designed dimensions of three types of power generators.	88
4. 3	Characteristic comparison of three prototypes.	101
5. 1	Comparison between different accelerations and mediums.	112
6. 1	Comparison of PZT thin film fabrication methods.	116
6. 2	Dependence of the residual stress of PZT thin film on the substrate conditions.	118
6. 3	The characteristics of materials used for calculation.	125
6. 4	Fabrication details of PZT micro-cantilever power generator.	130
6. 5	Measured dimensions and effective volume of the PZT device (μm).	134
6. 6	Comparison among MEMS piezoelectric energy harvesting devices.	143
7. 1	Dimensions of the cantilever (μm).	158

CHAPTER 1

INTRODUCTION

1.1 Motivation—an overview of the problem

With the recent advances in microelectromechanical systems (MEMS), portable electronics and wireless sensors have become ubiquitous because of their apparent advantages over wired devices, such as small size, flexibility—can be placed almost anywhere, ease of implementation—without the expense and trouble of cabling, low power consumption, etc [1]. These application characteristics of wireless devices decide that the development trend in electronic technology is multi-function, light-weight, miniaturization, low costs, short response time, high accuracy, and high reliability as well [2].

However, the miniaturization of wireless devices has been hindered by conventional batteries, which are the traditional power sources of many portable electronics and wireless sensors in current technology. For example, a wireless sensor node is generally composed of micro control electronics, wireless communication components or transceivers, integrated sensor, and battery as shown in Figure 1-1. The size of a sensor node has been scaling down because the sizes of the integrated sensor, the transceiver, and other control electronics continue to be scaled down with the advances in MEMS and related technologies, but the big size and heavy weight battery is

still one of the discouraging issues. The size of the sensor node is therefore depending on the size of the battery.

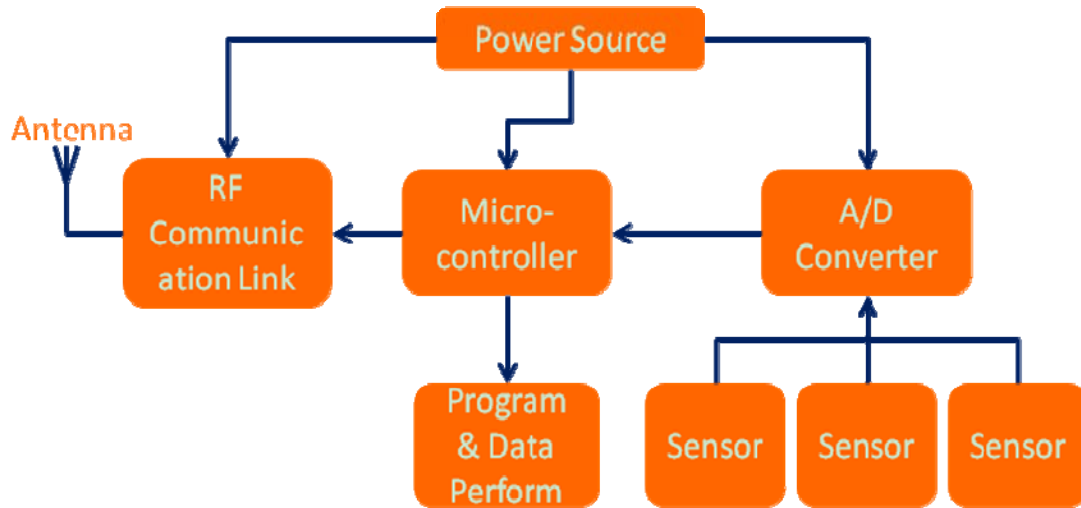


Figure 1- 1 Architecture of a sensor node.

Most commercial wireless sensor nodes use the big size of AA batteries as the power sources [3]. This strictly limits the further scale down of wireless devices. Besides, the disadvantages of batteries also include finite amount of energy or limited time span, large maintenance requirements, very high mass to electrical power ratio, and possible hazardous chemicals and environmental effects. The limited time span of a battery makes a device not so reliable because it may stop working at any time without a notice due to the sudden dead of the battery. The dead battery has to be replaced that is a tedious and expensive task, especially when the device is located in a remote location. The very high mass to electrical power ratio of a battery impedes the development of

light-weight wireless devices. Most batteries often involve hazardous chemicals, so inappropriate disposal or recycling may induce dangerous elements into environment. More dangerously, a battery explosion caused by the misuse or malfunction of a battery may cause vital and property loss. Consequently, batteries have to be replaced in miniature wireless devices.

Renewable or sustainable power sources are therefore required to either replace or to augment the capacity of battery to increase the lifespan and the reliability of a wireless device or to realize small volume and fully self-powered electronics and to mitigate the environmental pollution caused by inappropriate disposal and recycling of batteries.

1.2 A potential solution—energy harvesting

1.2.1 Energy harvesting

The concept of energy harvesting, which is a process of capturing ambient waste energy and converting it into useable electricity, was proposed and related research has been highly developed since the past decade to achieve small volume and completely self-powered electronics especially with the recent advent of the extremely low power electrical and mechanical devices such as microelectromechanical systems (MEMS) make such renewable power sources very attractive.

The earliest energy harvesting can be traced back to windmills in the ninth century. People have been started utilizing light, heat, vibration, and others ambient energy for many decades.

Since small autonomous wireless devices such as wireless sensors developed in MEMS technology demand a little power, small scale energy harvesting devices show that potential to replace the conventional batteries by converting ambient waste energy into electricity and power these low power consumption and small size of devices.

1.2.2 Potential energy harvesting sources

A variety of ambient sources such as solar, thermal, acoustic noise, acoustic energy, nuclear power, human, and mechanical vibration have been studied as an additional energy supplier for the last decades. Among them, thermoelectric generators, vibration/kinetic driven power generator, and solar cells are more widely studied because of their ubiquity, high efficiency, and potentials to miniaturization.

Thermal gradient can be conveniently converted to electricity, and there are many potential sources such as geothermally heated ocean water (85 °C), solar ponds (50 °C), natural lake thermoclines (10-20 °C), and utility power plant waste heat (15 °C) [4]. As far as 1979, Henderson analyzed a heat exchanger-thermoelectric generator system [5]. Benson et al in 1980 proposed to use bulk scale thermoelectric generator to produce electricity from low grade heat sources [6], and later in 1982 the same group proposed thin film thermoelectric generator [7]. Lemley in 1980 proposed to convert long wave infrared radiation leaving the earth surface to electricity [8]. Wu studied the performance of a generator converting energy from a solar pond in 1995 [9], and from industrial waste heat sources in 1996 [10]. Kish et al in 2000 successfully fabricated micro thermoelectric modules with an overall size of $2 \times 2 \times 1.3 \text{ mm}^3$ consisting of more than 50 pairs of

elements used to power wristwatches [11]. Qu et al in 2001 fabricated thermoelectric generators on flexible foil substrate as a power source for autonomous Microsystems [12]. Strasser et al in 2002 reported miniaturized thermoelectric generators (TEGs) developed to convert waste heat into a few microwatts of electrical power, sufficient to supply microelectronic circuitry [13]. However, thermal energy is hard to control, cannot be used for medical implant, and the conversion efficiency is lower comparing with solar and vibration energy sources as shown in Table 1.1.

Table 1. 1 Power density comparison of ambient energy sources.

Energy source	Power density ($\mu\text{W}/\text{cm}^3$ or cm^2)	Reference
Solar	Outdoor: 15000 Indoor: 10	[14]
Vibration	Electrostatic: 50~100 Electromagnetic: 119 Piezoelectric: 250	[15, 16] [17] [18]
Thermal	60 (5°C gradient)	[19]

We can also see from Table 1.1 that outdoor solar energy has the highest power density, but indoor solar energy has a rather low energy density. Solar cells are a mature technology and a mature research area. Vibration energy shows a relatively high power density. Figure 1-2 depicts the power densities and the lifetime of various batteries and two potential ambient energy sources, solar and vibration, which show a high power

density and an infinite lifetime. Among these, batteries expose their biggest disadvantage, limited life span. Solar lighting has the highest output power density in direct sunshine, but it is not applicable to embedded applications (such as medical implant) where no or not enough light available [18]. Mechanical vibration has been demonstrated to offer great potential, limited life span and relatively high power density where there is an insufficient light source [15-18].

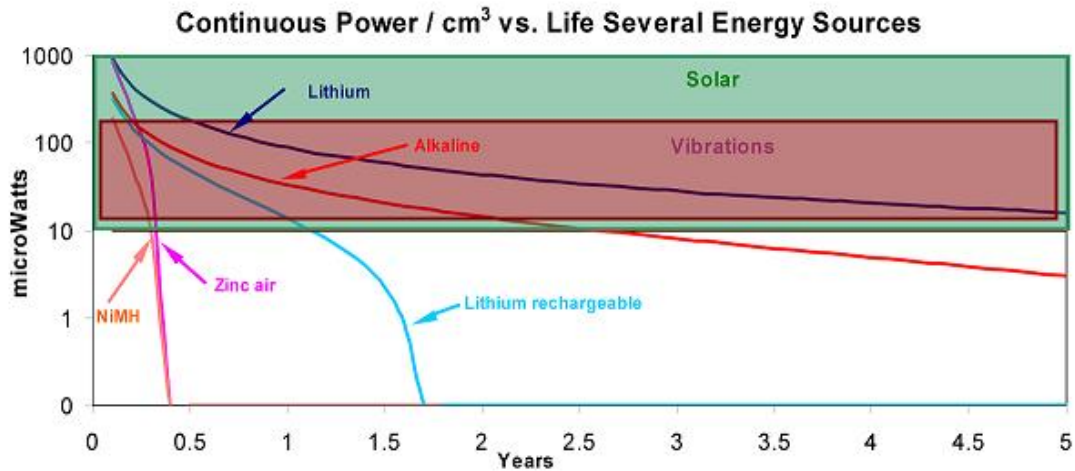


Figure 1- 2 Comparison of the output power density and the lifetime among battery, solar and vibration energy sources [18].

As shown in Table 1.2, vibration sources are generally ubiquitous and can be readily found in accessible locations such as air ducts and building structures. From Table 1.2 we can see that most vibration sources show a peak frequency below 200 Hz, and acceleration amplitude of a dozen m/s^2 . But, some vibration sources show a relatively high peak frequency and much higher acceleration amplitude.

Table 1. 2 Peak frequency and acceleration amplitude of various vibration sources [18, 20-23].

Vibration source	Frequency of peak (Hz)	Acceleration amplitude (m/s ²)
Kitchen blender casing	121	6.4
Clothes dryer	121	3.5
Door frame just after door closes	125	3
Small microwave oven	121	2.25
HVAC vents in office building	60	0.2 ~ 1.5
External windows next to a busy street	100	0.7
Washing machine	109	0.5
Notebook computer while CD is being read	75	0.6
Second story of wood frame office building	100	0.2
Refrigerator	240	0.1
Car engine compartment	200	12
Handheld tools	8 ~ 500	0.1 ~ 80
Vehicles	5-2000	0.5~110

The three types of electromechanical transducers including electrostatic, electromagnetic, and piezoelectric have been utilized to design and build vibration-based energy harvesting devices, as shown in Figure 1-3 [18, 24].

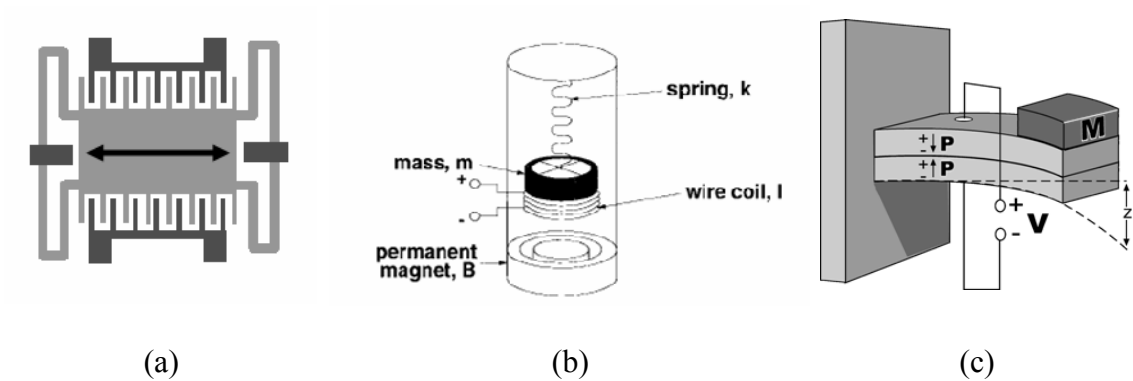


Figure 1- 3 Schematic diagrams of the three types of electromechanical transducers: (a) electrostatic; (b) electromagnetic; (c) piezoelectric.

Amirtharajah et al. in 2000 used a MEMS capacitive transducer to convert vibration energy to power a micro device [24]. Meninger et al. in 2001 proposed a variable capacitor to convert ambient mechanical vibration into electrical energy the simulated power density is about $3.8 \mu\text{W}/\text{cm}^3$ [25]. Roundy et al. in 2002 designed a MEMS electrostatic vibration-to-electricity converter, and the expected power density is about $116 \mu\text{W}/\text{cm}^3$ from an input vibration of 2.25 m/s^2 at 120 Hz [26]. Miyazaki et al. in 2003 capitalized on a variable-resonating capacitor to convert the vibration energy to electricity [16].

Williams et al. in 1995 designed an electromagnetic micro-generator with a dimension of $5 \times 5 \times 1 \text{ mm}^3$, and the predicted power output is about $40 \text{ } \mu\text{W}/\text{cm}^3$ at 70 Hz, and $4000 \text{ } \mu\text{W}/\text{cm}^3$ at 330 Hz assuming a deflection of $50 \text{ } \mu\text{m}$ [27]. Shearwood et al. in 1997 developed an electromagnetic micro-generator and power density is about $2.4 \text{ } \mu\text{W}/\text{cm}^3$ [28]. Amirtharajah et al. in 1998 designed a moving coil electromagnetic transducer used as a power generator, and the calculated power is on the order of $400 \text{ } \mu\text{W}$ [29]. Li et al. in 2000 did modeling and simulation of a micromachined vibration-based electromagnetic power generator [30]. El-hami et al. in 2001 fabricated an electromagnetic transducer to convert vibration energy to electricity and it can generate $4167 \text{ } \mu\text{W}/\text{cm}^3$ at a vibration frequency of 320 Hz [31]. Ching et al. in 2002 presented a laser-micromachined springs to convert mechanical vibration energy into electric power and the output power density is about $830 \text{ } \mu\text{W}/\text{cm}^3$ with a loading resistance of $1 \text{ k}\Omega$ from an input of 60-100 Hz and $\sim 200 \text{ } \mu\text{W}$ amplitude [32]. Beeby et al. in 2006 utilized an electromagnetic transducer to realize a vibration-based electromechanical power generator [17].

Piezoelectric energy harvesting devices have been more intensively studied and present many advantages over than other two mechanisms such as simple configuration, high converting efficiency, and precise control [1, 18, 33-43]. The detailed literature review will be presented in Chapter 2.

The approximate power density comparison of the above three conversion mechanisms can be found in Table 1.1. Table 1.3 presents the comparison among these three power generating mechanisms. Piezoelectric power generators present higher

power output, simpler configuration, and potential of miniaturization. It is therefore chosen as the study objective of this dissertation.

Table 1. 3 Comparison of three types of transducers [18, 44].

	electrostatic	electromagnetic	piezoelectric
Advantages	Easily integrated into micro-systems small size; precise control of the mechanical resonance	No voltage source required; relatively high power output	No voltage source required; higher output voltage; small size; simple structure, high efficiency; precise mechanical control
Disadvantages	Require separate voltage source; need higher frequency than piezoelectric	Complex design; difficult to integrated into micro-system	Difficult to integrated into micro-system; need high frequency and stress; limited material selection
Governing equation*	$U = \frac{1}{2} \epsilon E^2$	$U = \frac{B^2}{2\mu_0}$	$U = \frac{\sigma_y^2 k^2}{2Y}$
Practical max. energy density (mJ/cm ³)	4	25	35

* U = energy density, ϵ = vacuum permittivity, E = electric field, B = magnetic field, μ_0 = magnetic permeability of free space, σ_y = yield stress, k = coupling coefficient, Y = Young's modulus.

1.3 Research objective and dissertation structure

1.3.1 Research objective

The objective of this research is to achieve an applicable, from the point of both power density and mechanical strength, MEMS-based piezoelectric power harvesting device applied to lower frequency (100 – 200 Hz) and higher acceleration amplitude (> 1g, gravitational acceleration) vibration environments.

This objective will be fulfilled through two phases:

1. Optimally design, fabricate and evaluate a bulk scale prototype of piezoelectric energy harvester to demonstrate the practicability of the device in the targeted environments, and then based on the performance of the bulk prototype, the necessity of the study on MEMS piezoelectric energy harvester will be determined. The optimization will be fulfilled through theoretical analysis on the resonant frequency, the power density, and the safety factor of the device. Several potential piezoelectric materials will also be compared.

2. Design and fabricate an MEMS piezoelectric energy harvester. The performance of the MEME device will be systematically analyzed to determine the feasibility of the micro-fabrication process, the fulfillment of the dimensional precise control, the effectiveness of the resonant frequency simulation model, and the practicability of the device in the targeted application environments.

1.3.2 Dissertation structure

Chapter 1 states the motivation or an overview of the problem about power sources in wireless technology and the concept of energy harvesting. The piezoelectric energy harvesting device has been found a smart choice to convert mechanical vibration energy into electricity and accordingly the focus of this research. The objective of this research and the dissertation structure are presented at the end.

Chapter 2 introduces the theoretical and research background, including the theory of piezoelectricity, the introduction to piezoelectric energy harvesting devices, and a comprehensive literature review on the current research on piezoelectric energy harvesting devices.

Chapter 3 describes the optimization, design and experiment on bulk-scale PZT prototype, including material selection, configuration design, experimental setup and measurement.

Chapter 4 investigates two other alternative higher mechanical strength piezoelectric materials (PVDF and MFC) and compares their working behaviors with the optimized PZT-based prototype.

Chapter 5 discusses a potential method, operation in higher density ambient, to improve the safety factor of fragile cantilever structure at high amplitude vibration environments.

Chapter 6 investigates the interlayer effects on the properties of PZT thin film and describes the design and experiment on MEMS prototypes based on Si wafer, including material study, device design, micro-fabrication, and device evaluation.

Chapter 7 describes the design and experiment on MEMS prototypes based on SOI wafer, including device design, micro-fabrication, and device evaluation.

Chapter 8 concludes the achievements and proposes the future work to improve power output and safety factor.

References

- [1] S. P. Beeby, M. J. Tudor, and N. M. White, "Energy harvesting vibration sources for microsystems applications," *Measurement Science and Technology*, vol. 17, pp. 175-195, 2006.
- [2] H. R. Trankler and O. Kanoun, "Recent advances in sensor technology," Budapest, 2001, pp. 309-316.
- [3] N. S. Hudak and G. G. Amatucci, "Small-scale energy harvesting through thermoelectric, vibration, and radiofrequency power conversion," *Journal of Applied Physics*, vol. 103, p. 101301, 2008.
- [4] J. W. Stevens, "Heat transfer and thermoelectric design considerations for a ground-source thermoelectric generator," Baltimore, MD, USA, 1999, pp. 68-71.
- [5] J. Henderson, "Analysis of a Heat Exchanger-Thermoelectric Generator System," in *the 14th intersociety Energy Conversion Engineering Conference*, Boston, MA, 1979, pp. 1835-1840.
- [6] D. K. Benson and T. S. Jayadev, "Thermoelectric energy conversion: economical electric power from low grade heat," *Proceedings of the International Conference on Thermoelectric Energy Conversion*, pp. 27-56, 1980.
- [7] D. K. Benson and C. E. Tracy, "Design and fabrication of thin film thermoelectric generators," Atlantic City, NJ, USA, 1982, pp. 238-240.
- [8] L. W. Lemley, "Radiation thermoelectric power converter," *Proceedings of the International Conference on Thermoelectric Energy Conversion*, pp. 20-26, 1980.
- [9] C. Wu, "Performance of solar-pond thermoelectric power generators," *International Journal of Ambient Energy*, vol. 16, pp. 59-66, 1995.
- [10] J. Chen, "Thermodynamic analysis of a solar-driven thermoelectric generator," *Journal of Applied Physics*, vol. 79, pp. 2717-2721, 1996.
- [11] M. Kishi, H. Nemoto, T. Hamao, M. Yamamoto, S. Sudou, M. Mandai, and S. Yamamoto, "Micro thermoelectric modules and their application to wristwatches as an energy source," in *Thermoelectrics, 1999. Eighteenth International Conference on*, 1999, pp. 301-307.
- [12] W. Qu, M. Plotner, and W. J. Fischer, "Microfabrication of thermoelectric generators on flexible foil substrates as a power source for autonomous microsystems," *Journal of Micromechanics and Microengineering*, vol. 11, pp. 146-152, 2001.

- [13] M. Strasser, R. Aigner, M. Franosch, and G. Wachutka, "Miniaturized thermoelectric generators based on poly-Si and poly-SiGe surface micromachining," *Sensors and Actuators A: Physical*, vol. 97-98, pp. 535-542, 2002.
- [14] S. Roundy, E. S. Leland, J. Baker, E. Carleton, E. Reilly, E. Lai, B. Otis, J. M. Rabaey, P. K. Wright, and V. Sundararajan, "Improving power output for vibration-based energy scavengers," *IEEE Pervasive Computing*, vol. 4, pp. 28-36, 2005.
- [15] P. D. Mitcheson, T. C. Green, E. M. Yeatman, and A. S. Holmes, "Architectures for vibration-driven micropower generators," *Journal of Microelectromechanical Systems*, vol. 13, pp. 429-440, 2004.
- [16] M. Miyazaki, H. Tanaka, G. Ono, T. Nagano, N. Ohkubo, T. Kawahara, and K. Yano, "Electric-Energy Generation Using Variable-Capacitive Resonator for Power-Free LSI: Efficiency Analysis and Fundamental Experiment," Seoul, South Korea, 2003, pp. 193-198.
- [17] R.N.Torah, S.P.Beeby, M.J. Tudor, T.O'Donnell, and S.Roy, "Development of a Cantilever Beam Generator Employing Vibration Energy Harvesting," 2006.
- [18] S. Roundy, P. K. Wright, and J. Rabaey, "A study of low level vibrations as a power source for wireless sensor nodes," *Computer Communications*, vol. 26, pp. 1131-1144, 2003.
- [19] H. Bottner, J. Nurnus, A. Gavrikov, G. Kuhner, M. Jagle, C. Kunzel, D. Eberhard, G. Plescher, A. Schubert, and K.-H. Schlereth, "New thermoelectric components using microsystems technologies," *Journal of Microelectromechanical Systems*, vol. 13, pp. 414-420, 2004.
- [20] Ikeda K, Ishizuka H, Sawada A, and U. K., "Vibration acceleration magnitudes of hand-held tools and workpieces," *Industrial Health*, vol. 36, pp. 197-208, 1998.
- [21] Y. Aiba, S. Ohshiba, H. Ishizuka, K. Sakamoto, I. Morioka, K. Miyashita, and H. Iwata, "A study on the effects of countermeasures for vibrating tool workers using an impact wrench," *Industrial Health*, vol. 37, pp. 426-431, 1999.
- [22] M. M. Frechin, S. B. Arino, and J. Fontaine, "ACTISEAT: Active vehicle seat for acceleration compensation," *Proceedings of the Institution of Mechanical Engineers, Part D: Journal of Automobile Engineering*, vol. 218, pp. 925-933, 2004.
- [23] S. Roundy, "On the effectiveness of vibration-based energy harvesting," *Journal of Intelligent Material Systems and Structures*, vol. 16, pp. 809-823, 2005.

- [24] R. Amirtharajah, S. Meninger, J. O. Mur-Miranda, A. Chandrakasan, and J. Lang, "A micropower programmable DSP powered using a MEMS-based vibration-to-electric energy converter," San Francisco, CA, 2000, pp. 362-363.
- [25] S. Meninger, J. O. Mur-Miranda, R. Amirtharajah, A. P. Chandrakasan, and J. H. Lang, "Vibration-to-electric energy conversion," *IEEE Transactions on Very Large Scale Integration (VLSI) Systems*, vol. 9, pp. 64-76, 2001.
- [26] S. Roundy, P. K. Wright, and K. S. J. Pister, "Micro-electrostatic vibration-to-electricity converters," New Orleans, LO, United States, 2002, pp. 487-496.
- [27] C. B. Williams and R. B. Yates, "Analysis of a micro-electric generator for microsystems," Stockholm, Sweden, 1995, pp. 369-372.
- [28] C. Shearwood and R. B. Yates, "Development of an electromagnetic micro-generator," *Electronics Letters*, vol. 33, pp. 1883-1884, 1997.
- [29] R. Amirtharajah and A. P. Chandrakasan, "Self-powered signal processing using vibration-based power generation," *IEEE Journal of Solid-State Circuits*, vol. 33, pp. 687-695, 1998.
- [30] W. J. Li, G. M. H. Chan, N. N. H. Ching, P. H. W. Leong, and H. Y. Wong, "Dynamical modeling and simulation of a laser-micromachined vibration-based micro power generator," *Int. J. Nonlinear Sci. Simulation*, vol. 1, pp. 345-353, 2000.
- [31] M. El-hami, P. Glynne-Jones, N. M. White, M. Hill, S. Beeby, E. James, A. D. Brown, and J. N. Ross, "Design and fabrication of a new vibration-based electromechanical power generator," *Sensors and Actuators, A: Physical*, vol. 92, pp. 335-342, 2001.
- [32] N. N. H. Ching, W. J. Li, P. H. W. Leong, Z. Wen, and H. Y. Wong, "A laser-micromachined multi-modal resonating power transducer for wireless sensing systems," Munich, 2002, pp. 685-690.
- [33] P. Glynne-Jones, S. P. Beeby, and N. M. White, "Towards a piezoelectric vibration-powered microgenerator," *IEE Proceedings: Science, Measurement and Technology*, vol. 148, pp. 68-72, 2001.
- [34] H. A. Sodano, J. Lloyd, and D. J. Inman, "An experimental comparison between several active composite actuators for power generation," *Smart Materials and Structures*, vol. 15, pp. 1211-1216, 2006.
- [35] H. W. Kim, A. Batra, S. Priya, K. Uchino, D. Markley, R. E. Newnham, and H. F. Hofmann, "Energy harvesting using a piezoelectric "cymbal" transducer in dynamic environment," *Japanese Journal of Applied Physics, Part 1: Regular Papers and Short Notes and Review Papers*, vol. 43, pp. 6178-6183, 2004.

- [36] S. Priya, C.-T. Chen, D. Fye, and J. Zahnd, "Piezoelectric Windmill: A novel solution to remote sensing," *Japanese Journal of Applied Physics, Part 2: Letters*, vol. 44, pp. 104-107, 2005.
- [37] Y. B. Jeon, R. Sood, J. H. Jeong, and S. G. Kim, "MEMS power generator with transverse mode thin film PZT," *Sensors and Actuators, A: Physical*, vol. 122, pp. 16-22, 2005.
- [38] H.-B. Fang, J.-Q. Liu, Z.-Y. Xu, L. Dong, L. Wang, D. Chen, B.-C. Cai, and Y. Liu, "Fabrication and performance of MEMS-based piezoelectric power generator for vibration energy harvesting," *Microelectronics Journal*, vol. 37, pp. 1280-1284, 2006.
- [39] N. M. White, P. Glynne-Jones, and S. P. Beeby, "A novel thick-film piezoelectric micro-generator," *Smart Materials and Structures*, vol. 10, pp. 850-852, 2001.
- [40] M. J. Konak, I. G. Powlesland, S. P. van der Velden, and S. C. Galea, "Self-powered discrete time piezoelectric vibration damper," in *Smart Materials, Structures, and Integrated Systems*, Adelaide, Australia, 1997, pp. 270-279.
- [41] V. H. Schmidt, "Theoretical electrical power output per unit volume of PVF2 and mechanical-to-electrical conversion efficiency as functions of frequency," Bethlehem, PA, USA, 1986, pp. 538-542.
- [42] N. S. Shenck and J. A. Paradiso, "Energy scavenging with shoe-mounted piezoelectrics," *IEEE Micro*, vol. 21, pp. 30-42, 2001.
- [43] G. K. Ottman, H. F. Hofmann, and G. A. Lesieutre, "Optimized Piezoelectric Energy Harvesting Circuit Using Step-Down Converter in Discontinuous Conduction Mode," *IEEE Transactions On Power Electronics*, vol. 18, 2003.
- [44] S. Roundy and P. K. Wright, "A piezoelectric vibration based generator for wireless electronics," *Smart Materials and Structures*, vol. 13, pp. 1131-1142, 2004.

CHAPTER 2

GENERAL BACKGROUND

2.1 Theoretical foundations

2.1.1 Piezoelectricity

Piezoelectric ceramics has been used to convert mechanical energy into electricity for many years [1]. A brief introduction about piezoelectricity will help to understand the theoretical background of piezoelectric power harvesting.

Piezoelectric materials can become electrically polarized or undergo a change in polarization when subjected to a stress because the slight change in the dimension of a piezoelectric material results in the variation in bond lengths between cations and anions caused by stress. This phenomenon was discovered on many crystals, for instance, tourmaline, topaz, quartz, Rochelle salt, and cane sugar, by Jacques and Pierre Curie brothers in 1880, and named as piezoelectricity or piezoelectric effect, which describes a relationship between stress and voltage. Conversely, a piezoelectric material will have a change in dimension when it is exposed in an electric field. This inverse mechanism is called electrostriction. Those devices utilizing the piezoelectric effect to convert mechanical strain into electricity are called transducers, which can be used in sensing applications, such as sensors, microphones, strain gages, etc.; while those devices

utilizing the inverse piezoelectric effect to generate a dimension change by adding an electric field are called actuators and used in actuation application, such as positioning control devices, frequency selective device, etc.

The constitutive equations of an unbounded piezoelectric material are given in Equations (2-1) to (2-4) [2]:

$$S_{ij} = s_{ijkl}^E T_{kl} + d_{kij} E_k \quad (2-1)$$

$$D_i = d_{ikl} T_{kl} + \varepsilon_{ik}^T E_k \quad (2-2)$$

$$S_{ij} = s_{ijkl}^D T_{kl} + g_{kij} D_k \quad (2-3)$$

$$E_i = -g_{ikl} T_{kl} + \beta_{ik}^T D_k \quad (2-4)$$

where i, j, k, l take the values 1, 2, 3 and are tensor notations, S is the strain component, s is the elastic compliance constant (m^2/N), T is the stress component (N/m^2), superscript T means at constant stress, d is the piezoelectric constant (m/V or C/N), E is the electric field component (V/m), superscript E means at constant electric field, D is the electric displacement component (C/m^2), superscript D means at constant electric displacement, ε is the dielectric constant of the piezoelectric material (F/m), g is the piezoelectric constant ($\text{V}\cdot\text{m}/\text{N}$ or m^2/C), β is the impermittivity components (m/F).

These constitutive equations can be simplified by a single subscript with compressed matrix notations:

$$S_p = s_{pq}^E T_q + d_{kp} E_k \quad (2-5)$$

$$D_i = d_{iq} T_q + \varepsilon_{ik}^T E_k \quad (2-6)$$

$$S_p = s_{pq}^D T_q + g_{kp} D_k \quad (2-7)$$

$$E_i = -g_{iq}T_q + \beta_{ik}^T D_k \quad (2- 8)$$

where p, q are related to ij or kl as shown in Table 2.1, and they take the values 1, 2, 3, 4, 5, and 6.

Table 2. 1 Relationship between tensor notations and compressed matrix notations.

ij or kl	p or q
11	1
22	2
33	3
23 or 32	4
31 or 13	5
12 or 21	6

Equation set (2-5) and (2-6) and Equation set (2-7) and (2-8) can be chosen to use for different geometrical, mechanical, and electrical conditions. In this research, we are interested in the relationship between the electrical field and the strain. And, the object is cantilever as shown in Figure 2-1, whose top and bottom surfaces are fully electrode, that is, the electrical condition can be approximated to $E_1 = E_2 = 0$, and the constitutive equation become

$$S_1 = s_{11}^E T_1 + d_{31} E_3 \quad (2- 9)$$

$$D_3 = d_{31} T_1 + \epsilon_{33}^T E_3 \quad (2- 10)$$

The piezoelectric material properties that we concern are therefore d_{31} and ϵ_{33} . From Equations (2-9) and (2-10), we can see that if the electric field is negligible, or there is no piezoelectric coupling term dE , Equation (2-9) becomes the Hook's law; similarly, if there is no stress or no term dT , Equation (2-10) becomes the Gauss' law for electricity or the dielectric equation.

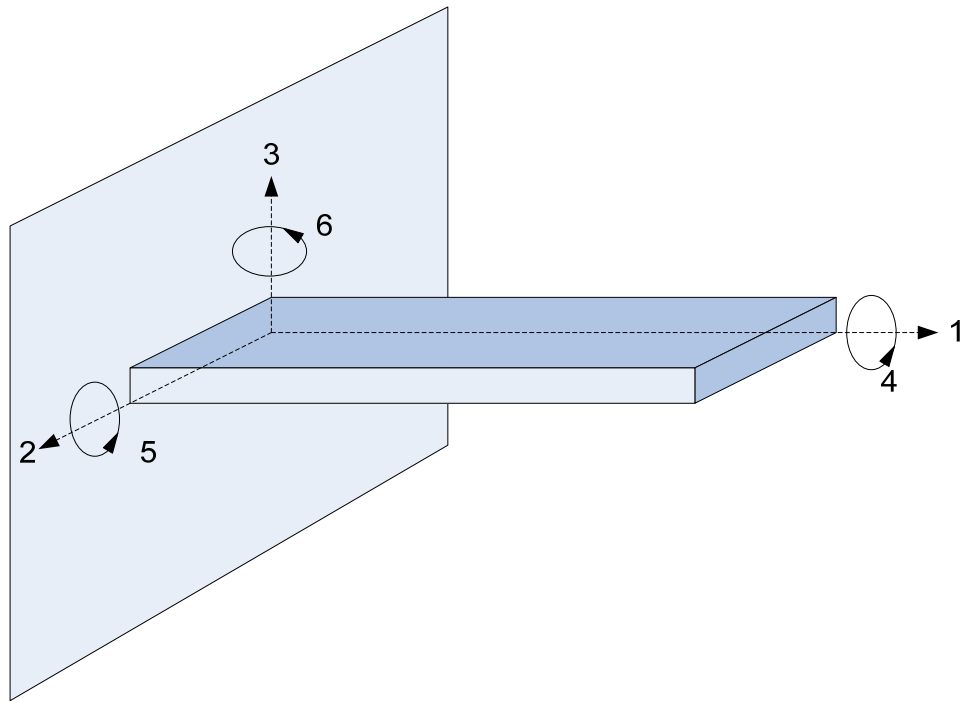


Figure 2- 1 A rectangular cantilever in a Cartesian coordinate system.

In this research, the piezoelectric material will be used to convert mechanical energy into electricity, that is, the piezoelectric effect will be used. Besides the d_{31} and ϵ_{33} , another property of a piezoelectric material used to evaluate its property is the electromechanical coupling coefficient (k_{31}) which is an indicator of the effectiveness with

which a piezoelectric material converts mechanical energy into electrical energy or electrical energy into mechanical energy and defined in Equation (2-11):

$$k^2 = \frac{\text{Input mechanical energy converted to electric energy}}{\text{Input mechanical energy}} \quad (2- 11)$$
$$= \frac{\text{Input electric energy converted to mechanical energy}}{\text{Input electric energy}}$$

2.1.2 Piezoelectric materials

Different types of piezoelectric materials are available such like single crystals (e.g. quartz SiO_2 and Rochelle salt), ceramics (e.g. lead zirconate titanate or PZT and BaTiO_3 or BTO), thin films (e.g. ZnO and PZT), thick films (e.g. PZT), and polymers (e.g. polyvinylidene fluoride or PVDF).

Table 2.2 lists the properties of some popular piezoelectric materials.

Table 2. 2 Properties of some piezoelectric materials.

Material and form	d_{31} (pm/V)	$\epsilon_{33} / \epsilon_0^a$	k_{31}	T_c (°C) ^b	Ref.
Quartz (single crystal)	2.3	4.4	-	-	[3]
BTO (polycrystalline)	-79	1900	0.21	120	[4]
PZT (polycrystalline)	-190~-320	1800~3800	0.32~0.44	230~350	[5]
PVDF (film)	23	12~13	0.12	80~100	[6]
PZT (sol-gel thin film)	190-250	800-1100	-	-	[7]
PZT (sputtered thin film)	100	-	-	-	[8]
ZnO (sputtered thin film)	10.5-11.5	10.8-11	-	-	[7]
AlN (thin film)	-	8.6	-	-	[9]

^a $\epsilon_0 = 8.854 \times 10^{-12}$ F/m, permittivity of empty space (vacuum)

^b Curie or maximum temperature

From Table 2.2 we can see that PZT has a higher electromechanical coupling coefficient and higher Curie temperature, which is the highest temperature in which a piezoelectric material has the piezoelectric property. Additionally, PZT is easily poled and has a wide range of dielectric constant. The superior properties of PZT decide its popularity in piezoelectric material family.

PZT are a solid solution of lead zirconate and lead titanate, $\text{Pb}(\text{Zr}_x\text{Ti}_{1-x})\text{O}_3$. The perovskite structure of PZT as shown in Figure 2-2 decides the piezoelectric property of PZT. Under a strong electric field, dipole forms because the Ti^{4+} or Zr^{4+} deviates from the neutral position which is the center of the unit cell. These electric dipoles can be reversed in an electric field. The reversion of dipoles can deform a PZT material. Or, a

deformed PZT material can produce electric charge on its surface electrodes due to the deviation of dipoles. Commercially, PZT ceramic was doped with either acceptor dopants, which create oxygen (anion) vacancies and generate hard PZT, or donor dopants, which create metal (cation) vacancies and generate soft PZT. The cation vacancies facilitate the domain wall motion, so soft PZT has a higher piezoelectric constant, but larger loss due to internal friction. The hard PZT has a lower piezoelectric constant and also lower loss because the domain wall motion is pinned by the impurities.

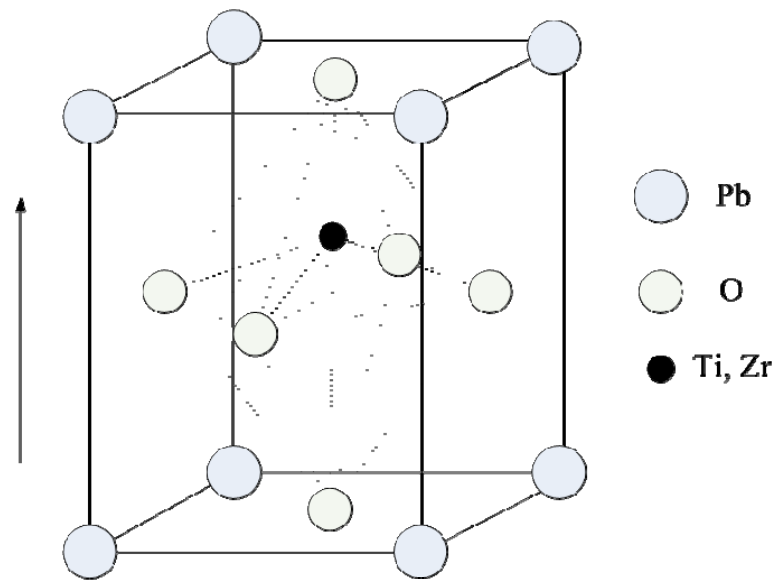


Figure 2- 2 Atomic structure of PZT at MPB.

When $x = 0.52$, the PZT ceramic shows an extremely large dielectric constant. This composition is called morphotropic phase boundary (MPB). The increased allowable domain states at MPB result in enhanced piezoelectric property, as shown in

Figure 2-3. There are 6 possible domain states from ferroelectric tetragonal phase $\langle 100 \rangle$ and 8 possible domain states from ferroelectric rhombohedral $\langle 111 \rangle$. At the MPB, there are totally 14 possible domain states.

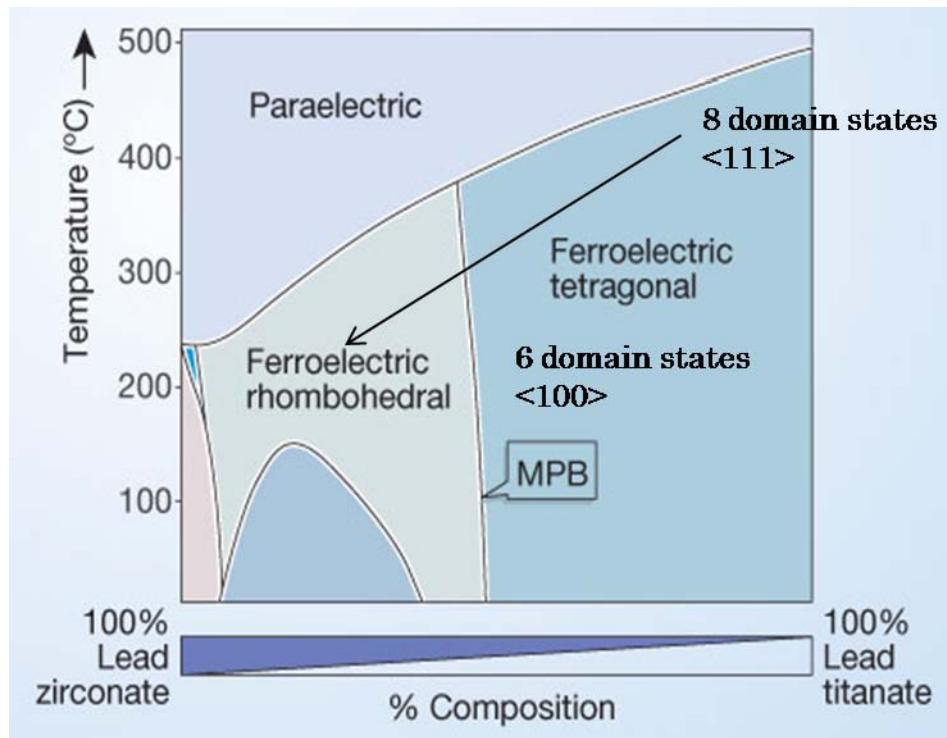


Figure 2- 3 Phase graph of PZT.

2.2 Piezoelectric power generator

In general, there are two different modes in which piezoelectric materials used as energy harvesters. When a mechanical stress is applied to a piece of piezoelectric material in the longitudinal direction (parallel to polarization), a strain is generated in the longitudinal direction or in the thickness of the piezoelectric material; and then a voltage

is generated which tries to return the piece to its original thickness, shown in Figure 2-4 (a). Similarly, when a stress is applied to a sheet in a transverse direction (perpendicular to polarization), a strain is generated in the transverse direction or in the length of the piezoelectric material; and then a voltage is generated which tries to return the piece to its original length and width, shown in Figure 2-4 (b).

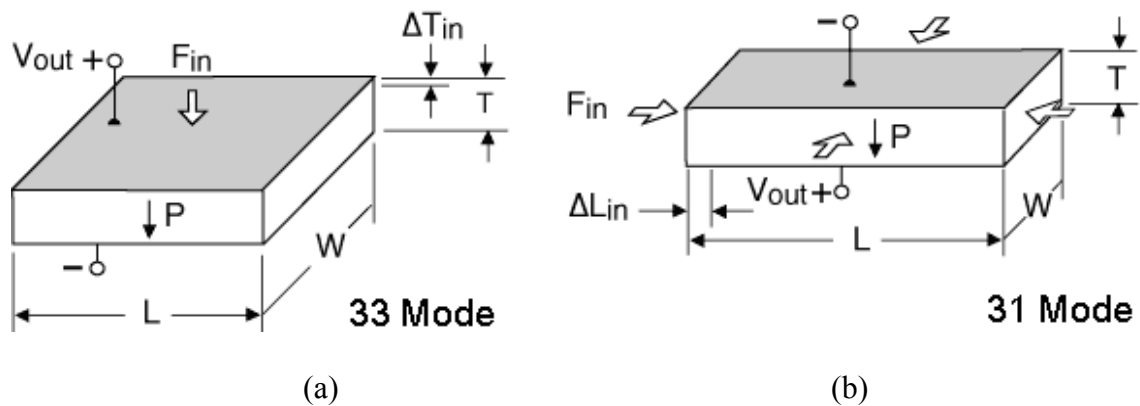


Figure 2- 4 Working modes of piezoelectric power harvester.

Although the 33 mode has higher converting coefficient than the 31 mode, for example, $k_{31}=0.44$ and $k_{33}=0.75$ for PZT 5H, other advantages of the 31 mode determine the priority of operating 31 mode, or the fixed-free cantilever configuration in our application. First, cantilever is an effective configuration to generate the largest strain when having the same force input. Second, the cantilever configuration has fewer limits than 33 modes, that is, it is much easier to realize low resonant frequency (< 100 Hz). So, the cantilever configuration was used to design the piezoelectric power harvester in this research.

Bimorph cantilever, as shown in Figure 2-5, a center shim laminated between two piezoelectric layers can improve the mechanical strength, although reducing motion, which improves the safety. Bimorph refers to the two layers of piezoelectric materials. A "2-layer" element actually has nine layers: four layers of electrode, two layers of piezoelectric material, two layers of adhesive, and a center shim.

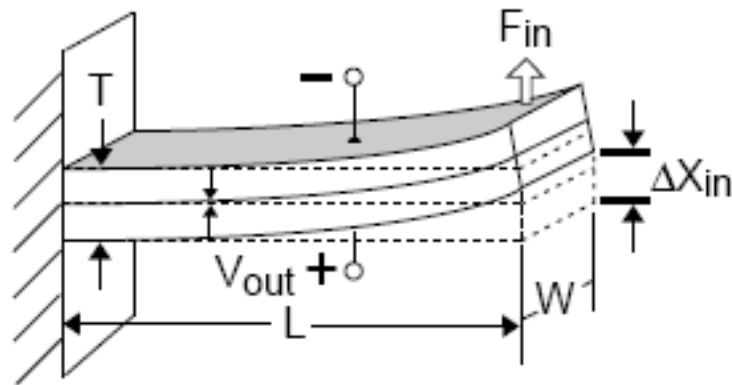


Figure 2- 5 Configuration of a bimorph power harvester.

Depending on the polarization and wiring configuration of the layers, there are two operations, series and parallel. *Series operation* refers to the case where supply voltage is applied across all piezoelectric layers at once. The voltage on any individual layer is the supply voltage divided by the total number of layers. A two-layer device wired for series operation uses only two wires (one attached to each outside electrode), as shown in Figure 2-6 (a). *Parallel operation* refers to the case where the supply voltage is applied to each layer individually. This means accessing and attaching wires to each layer. A two-layer bending element wired for parallel operation requires three wires (one

attached to each outside electrode and one attached to the center shim), as shown in Figure 2-6 (b). For the same motion, a two-layer element poled for parallel operation needs only half the voltage required for series operation. The two layers offer the opportunity to reduce output voltage by half and to increase output current twice when configured for parallel operation, which was used in this research.

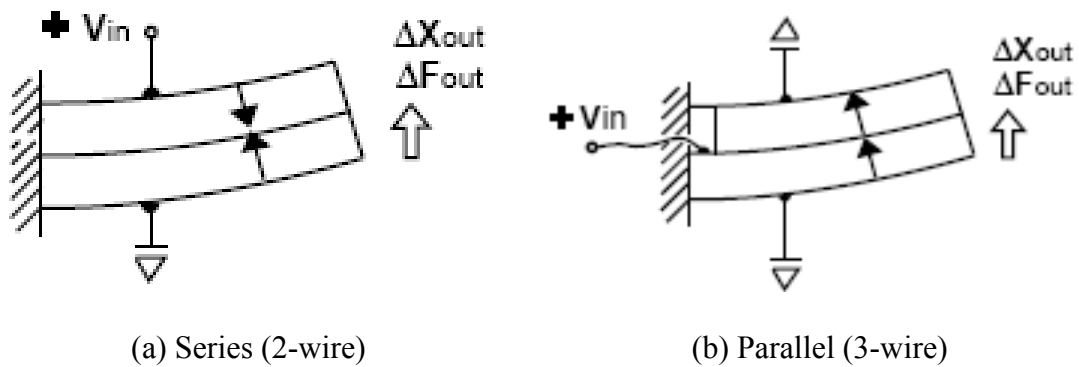


Figure 2- 6 Operations of two-layer cantilever power harvester.

2.3 Literature review on piezoelectric power generator

2.3.1 Bulk scale Piezoelectric Power Generators (PPG)

Piezoelectric power generator under mechanical quasi-static and dynamic stress

It's been decades that people have started using piezoelectric transducers to convert mechanical energy to electric energy [10]. Piezoelectric ceramics attract people's interest because of their high electromechanical coupling coefficient. At the early stage, people investigate more on the bulk piezoelectric generator as shown in Figure 2-7.

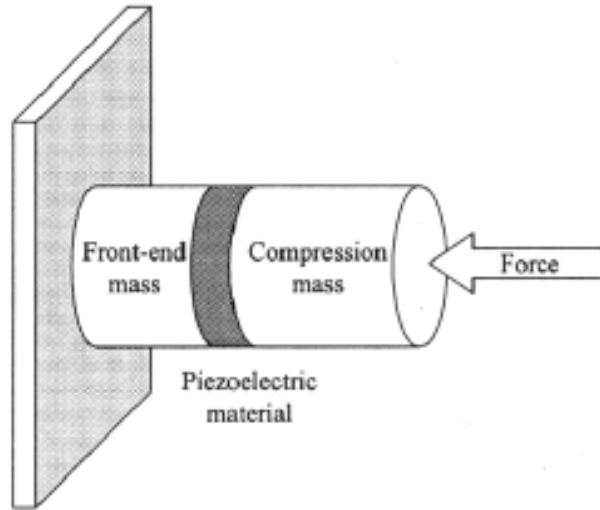


Figure 2- 7 Schematic diagram of the bulk piezoelectric generator [11].

Umeda et al in 1996 reported the mechanism of power generation in which mechanical impact energy is transformed to electricity with a steel ball impacting a piezoelectric vibrator [12]. The piezoelectric generator consists of 0.25 mm thick piezoelectric ceramic with a diameter of 19 mm and a 0.25 mm thick bronze disk with a diameter of 27 mm. These two disks are bonded together and fixed by a holder at the edge. The output of this generator over a resistive load was studied when a free steel ball (mass = 5.5 g) fell onto it from different height. The transformation efficiency, defined by the ratio of impact energy and electric energy, at heights of 20, 25, and 30 mm were measured with different resistive loads, and the optimal transformation efficiency at every height obtained with a 10 k Ω resistive load are about 5, 7, and 9%. The low efficiency results from the bouncing off of the steel ball. If the steel ball does not bounce off from the generator, the efficiency calculated could be over 50%. Ideally, it will close

to 100% if an inelastic collision occurs and the mechanical quality factor Q of the generator is higher than 1000. The same group presents the theoretical and experimental results of the energy storage using an equivalent circuit by the similar piezoelectric generator developed previously in 1997 [13]. A maximum efficiency over 35% was achieved by investigating the effect of the capacitance and the initial voltage.

Funasaka et al in 1998 investigate the transformation efficiencies of piezoelectric power generators made of a single LiNbO_3 plate or a multilayer LiNbO_3 under a hammer impact [14]. The thin plate generator has an efficiency of 78% comparing with a conventional PZT generator with an efficiency of 65% due to the much higher Q -factor (2640 vs. 580); the multilayer generator has an efficiency of 70%.

After a lot of work on the electric response of piezoelectric ceramics under high impact stress [12-17], people's interest was diverted to low mechanical stress conditions due to brittle fracture of piezoelectric ceramics [18]. Xu et al in 1996 and 1998 presented their study results on the power generation characteristics of Mn-doped PZT ceramics under both slow mechanical stress (constant-rate loading) and impact stress (free falling ball impacts on PZT) [19, 20]. They found by comparing these two types of stresses that slow stress generates two output current peaks with opposite directions, but the impact stress generates nearly one-directional signal, moreover, the output charge and energy by slow stress are two orders of magnitude higher than that generated by impact stress.

Keawbooncliny in 2002 studied the relationship between the power output of a bulk piezoelectric material, as shown in Figure 2-7 and the thickness to area ratio [11]. Both theoretical and experimental results have shown that power output linearly increase with the thickness to area ratio of the piezoelectric element. The peak power output of

the generator ranges from 7 – 28 kW or 173 kW/cm³. In 2003, he investigated the power generation characteristics of piezoelectric generator under quasi-static (stress duration > 100 ms) and dynamic (stress duration < 10 ms) stress condition [21]. He found from simulation that a quasi-static stress produced a bidirectional voltage output, and a dynamic stress produced a unidirectional voltage output. He also found the dynamic stress produced a 10 times higher voltage output than the quasi-static stress because the piezoelectric capacitance has enough time to charge in the quasi-static case.

Poulin et al. in 2004 investigated the power generation of a PZT ceramic bar polarized in the longitude direction embedded at one end and vibrating at 33-mode [22]. The maximum power output is 7.7 μW or 86 W/m³, and the corresponding conversion coefficient is about 0.52 at resonance. The maximum conversion coefficient is about 0.76, and the corresponding power output is 5.6 μW or 63 W/m³ at resonance.

Piezoelectric power generator —Shoe insert

As early as 1995, Antaki et al proposed to extract useful energy from people's ambulation to provide supplemental power for operating electrically powered artificial organs using shoe generator system made of piezoelectric ceramic transducer [3]. The piezoelectric transducer within midsole consists of a single cylindrical stack of 18 PZT ceramic slugs, each having a diameter of 0.31 inch and a thickness of 0.245 inch. The output powers of midsole generator from a man weighted 75 kg are 625, 676, and 2100 mW respectively corresponding to flat foot, heel-toe, and simulated jogging.

Starner in 1996 investigate various human activities including footfalls, arm motion, blood pressure, body heat, exhalation, breathing band, and finger motion [23]. He found that the most plentiful power (5.0-8.3 W) can be generated while walking at a brisk pace (two steps per second with the foot moving 5 cm vertically) and even a small part of this power would provide enough power to operate many of the body-worn systems.

A lot of research accordingly had been done based on Starner's results [24-29]. Because of the hardness and fragility of piezoelectric ceramics, Shenck et al in 2001 from the MIT Media Laboratory had been focusing on embedding flexible piezoelectric materials (PVDF) into shoes to result in minimal impact on the shoe's design or feel although the conversion efficiency of PVDF is much lower than PZT [28]. Two approaches were used in the shoe insert power generator: PZT dimorph under heel and PVDF stave under the ball of the foot as shown in Figure 2-7.

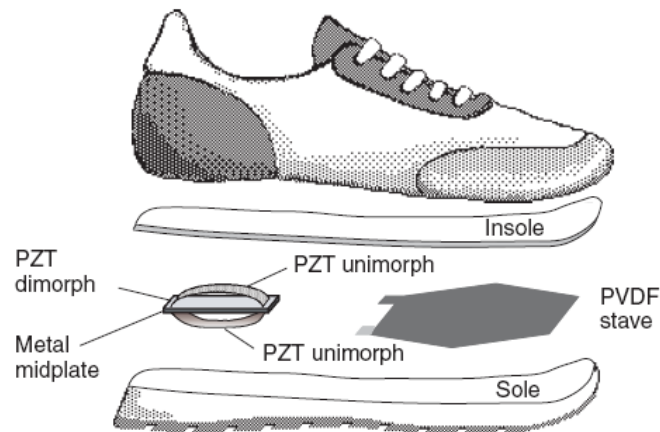


Figure 2- 8 Shoe insert power generator in two positions: PZT dimorph and PVDF stave [28].

Piezoelectric power generator—plate or diaphragm

Ichiki et al. in 2002 studied the output behavior of piezoelectric disk under 40 N input applied load [30]. Output peak power of the PZT transducer is about 3 μ W.

Kim Sunghwan et al. in 2005 investigated the influence of geometric design parameters and electrode configuration on the power output from a clamped circular unimorph piezoelectric plate under an applied pressure source [31, 32]. It has been found that the piezoelectric layer / substrate layer thickness ratio and the electrode pattern have a significant effect on energy conversion. The thickness ratio can change the location of the neutral surface, which can change the stress distribution in the piezoelectric layer. Additionally the substrate thickness can also change the boundary conditions of the piezoelectric material and the capacitance of the energy harvesting device. But, the capacitance change is so small at this experimental condition that it has little effect on the power generation.

Cymbal and moonie are two popular metal-ceramic composite transducers. They are composed of a piezoelectric disk with a hollow metal cap bonded on the top and the bottom of the piezoelectric disk. The difference between these two structures is that the displacement in a cymbal is combination of flexural and rotation motions, and in a moonie is a pure flexural motion of the end caps. Comparing with moonie transducer, cymbal transducer has higher displacement and stability under loading, and lower cost. It is therefore studied more. Kim Hyeoung woo et al. in 2004 investigated a piezoelectric cymbal transducer under higher loading force amplitude (1k N, automobile engine vibration level) and lower frequency (50-150) as a energy harvesting device [33]. They

found that the cymbal transducer is a promising transducer under the above conditions. The power output of the designed cymbal under a force of 7.8 N is 39 mW or 60 mW/cm³. Kim Hyeoung woo in 2005 reported the performance of a piezoelectric cymbal transducer under even higher AC force (70 N) with a pre-stress load of 67 N at 100 Hz [34]. A thicker steel cap enhanced the mechanical strength or endurance of the ceramic structure. The generated power measured across a 400 kΩ is about 52 mW or 44 mW/cm³. The same group in 2006 developed a theoretical model to determine the magnitude of power as a function of resistive load and frequency [35]. The simulated results were validated by experimental data. The power output is proportional to the frequency and the displacement of vibration at high frequency. More than 100 mW power was expected under wide range of vibration sources.

Piezoelectric power generator —cantilever

Although cantilever piezoelectric power generator has many drawbacks such as weak mechanical strength, piezoelectric voltage coefficient is low, maximum displacement is limited by limited maximum applied force, fatigue caused by bending shorten its lifetime, it cannot stop people's interest in it because of their high strain and high power output even under lower acceleration amplitudes. Until now, cantilever structure for piezoelectric power generation has been extensively studied. The cantilever transducer has different configurations such as bimorph, unimorph, and rainbow.

Roundy et al. in 2003 compared the power output of between a capacitive or electrostatic power generator and a piezoelectric power generator [36]. The simulations

show that the potential power output of the bimorph cantilever PZT power generator is significantly higher. And the demonstrated PZT prototype can generate a power density of $70 \mu\text{W}/\text{cm}^3$. Moreover, the simulated power density of an optimized device would be able to generate $250 \mu\text{W}/\text{cm}^3$ from vibration with frequency of 120 Hz and acceleration amplitude of 2.5 m/s^2 . In 2004, they optimized the piezoelectric power generator, and the optimized device can generate a power density of $375 \mu\text{W}/\text{cm}^3$ from a vibration with a frequency of 120 Hz and an acceleration amplitude of 2.5 m/s^2 [37]. Furthermore, this generator has been used to power a custom designed 1.9 GHz radio transmitter [38]. In 2005, they proposed new designs about piezoelectric cantilever-based energy scavengers, which can be tuned to the frequency of the host surface to expanding the flexibility of the device, or the different geometries of the device can improve the power output by making the stress evenly distributed in the PZT cantilever beam [39]. In 2005, Roundy proposed a general effective theory and compared the output behaviors of different vibration-based generators, including electrostatic, electromagnetic, and piezoelectric generators [40, 41]. He concluded that the power output depends on the system coupling coefficient, the quality factor of the device, the density of the device, and the degree to which the electrical load maximizes power transmission. He also found that the electromagnetic generator tends to produce very low AC voltages. The voltage output will be even lower as the size scales down. Piezoelectric generator tends to produce high voltages and low currents. For both piezoelectric and electrostatic generator, current instead of the voltage output will be lower as the size scales down because of the decreased capacitance of the device.

Ottman et al. in 2002 reported the study on the adaptive piezoelectric energy harvesting circuit and optimized circuit using step-down converter in discontinuous conduction mode for wireless remote supply [42, 43]. During the experiment, he used a Quickpack[®] QP20W piezoelectric element purchased from Active Control eXperts (ACX) (as shown in Figure 2-11) as the power generator. This piezoelectric element is a bimorph actuator with piezo wafers embedding in a Kapton and epoxy matrix. The output behavior of this piezoelectric element with a cantilever boundary condition under a transverse vibration was study.



Figure 2- 9 QuickPack[®] Actuator [44].

Sodana in 2003 and 2004 developed a model of the piezoelectric power harvesting device and estimated the electric charge output for piezoelectric energy harvesting [45, 46]. During the experimental verification, he also used the Quickpack[®] QP40N piezoelectric element as the power generator. In 2003 and 2004, he reported his study on macro-fiber composite (MFC) for sensing, actuation, and power generator [47, 48]. MFC consists of rectangular piezoelectric ceramic rods sandwiched between layers

of adhesive and electroded polyimide film [49]. The interdigitated electrodes can transfer charge when the MFC bender deflects. Comparing with traditional piezoelectric ceramic (PZT) actuators, the major advantages of MFC actuators are their flexibility, durability, and larger ability to couple the electrical and mechanical fields. In 2004 they reviewed piezoelectric power harvesting from vibration and discussed the future goals that must be achieved such as improving power output and energy conversion efficiency [50]. In 2005 and 2006, they compared different cantilever piezoelectric energy harvesting devices, including Mide Quick Pack, Mid Quick Pack IDE, PZT, and MFC [51, 52]. The power output of Quick Pack IDE actuator is similar to that of MFC and lower than that of Quick Pack. PZT shows more effective capability to recharging a capacitor. The low power outputs of Quick Pack IDE and MFC result from the low capacitance characteristics caused by the IDE configuration of the MFC and the Quick Pack IDE. But, the fibrous nature of the piezoelectric ceramic PZT in the MFC is not found negative effects on the actuator's performance.

Priya et al. in 2005 demonstrate piezoelectric windmill made of bimorph piezoelectric cantilevers arranged along the circumference of the mill [53, 54]. Every bimorph cantilever has a dimension of $60 \times 20 \times 0.5 \text{ mm}^3$ and a preload of 23.5 gm. The power output measured across a resistive load of $4.6 \text{ k}\Omega$ is 10.2 mW at an oscillation frequency of 6 Hz.

2.3.2 Piezoelectric Micro Power Generator (PMPG)

Ramsay and Clark in 2001 investigated the feasibility of using piezoelectric materials to power an in vivo MEMS application [55]. They found the mechanical advantage of 31-mode (transverse loaded) generator over 33-mode generator in converting applied pressure to working stress for piezoelectric conversion. The requirement on continuous power for a typical bio MEMS chip is 10 mW and 2.8 μ W for an intermittent application (once per hour). The predicted power output from a $10000 \times 10000 \times 9 \mu\text{m}^3$ PZT-5A square plate will be in the μ W power range continuously and up to the mW range intermittently.

Most current research on piezoelectric energy harvesting devices is concentrated on bulk prototypes; however, a few groups have been started to study piezoelectric micro-generator and demonstrated MEMS devices capable of generating useful power.

As early as 1996, Williams and Yates analyzed a piezoelectric micro-electric generator for microsystem [56]. The proposed micro-generator has a dimension of $5 \times 5 \times 1 \text{ mm}^3$. The predicted power output is about 1 μ W at 70 Hz and 0.1 mW at 330 Hz assuming a displacement of 50 μm . They conclude from the analysis that the power output is proportional to the cube of frequency of the vibration source and the power output is maximized when the seismic mass is as large as possible.

White et al. in 2001 developed a novel thick-film piezoelectric micro-generator as shown in Figure 2-7 [57]. The length is about 23 mm, and the maximum width is about 20 mm. The cantilever power generator beam was tapered to obtain a constant strain along the length of the piezoelectric beam. The PZT-5H thick-film and the electrode

layers were deposited by multiple printing and firing. The small seismic mass attached at the free end tip of the beam has a mass of 0.8 g. The simulated and experimental power output of this device is about $2 \mu\text{W}$ at a frequency of 80 Hz. The low power output is due to the lower coupling coefficient of the thick-film than bulk PZT. There approaches were proposed by the authors to improve the power output: densification of the film, multi-beam configuration design to match different ambient vibration frequencies, and multilayer piezoelectric material.

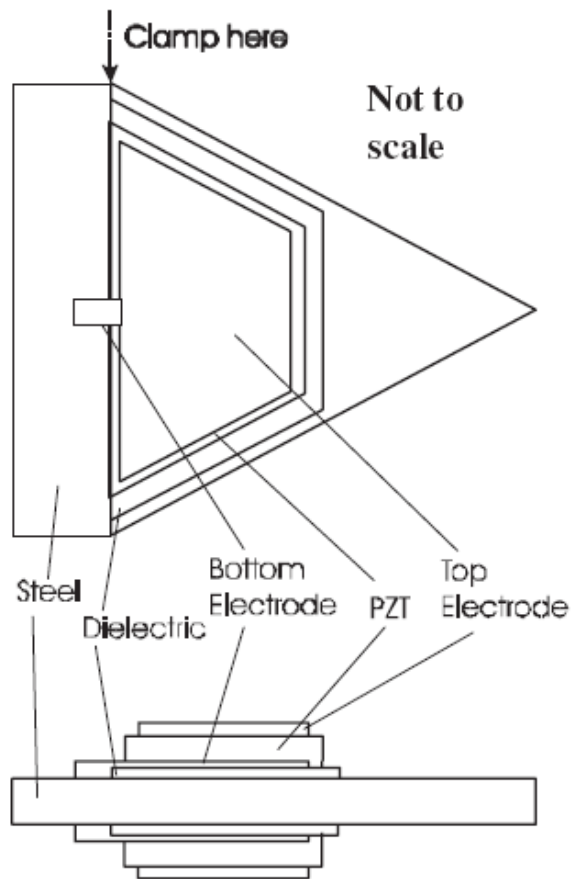


Figure 2- 10 Schematic diagram of a thick-film piezoelectric micro-generator [57].

Zurn et al. in 2001 reported the fabrication and structural characterization of a resonant frequency PZT cantilever without a proof mass used as both the micro-sensor and micro-actuator [58]. This cantilever has a Pt/PZT/Pt/Ti/Si₃N₄/SiO₂/Si multi-layer structure and a dimension of $1000 \times 300 \times 4.5 \mu\text{m}^3$.

Demir et al. in 2004 examined the behavior of thin-film piezoelectric membranes at high deflections and strains for power generation applications [59]. An Au/PZT/Pt/Ti/SiO₂/Si multi-layer membrane was fabricated. Experimental results show that increasing the thickness of PZT layer and Ti component in PZT chemistry will increase the power output for a given deflection. The tensile residual stress in PZT thin film can lead to a lower deflection for a given force and accordingly lower the power output, but increasing the Ti element in PZT can produce lower residual stress.

Lu et al. in 2004 developed a simple model to analyze the 31-mode piezoelectric micro-generator, and compared two types of laminated micro-generators respectively made of PZT and PZN-8% PT [60]. The dimensions of the piezoelectric material are $5 \times 1 \times 0.1 \text{ mm}^3$, and the power output at 2939 Hz for these two devices are respectively 0.64 and 0.31 mW at a deflection of 30 μm . PZN-8% PT is more sensitive to the operational frequency, but PZT is more sensitive to the resistive load.

Due to the difficulty in fabricating high quality PZT thin film during the whole processes of fabricating a MEMS piezoelectric power generator. Marzencki et al. in 2005 firstly fabricated a thin film AlN cantilever generator that can generate 0.038 μW from a 0.5g ($g = 9.81 \text{ m/s}^2$) vibration at its resonant frequency of 204 Hz [61, 62]. The output power of their device is limited to low power levels by the properties of AlN. Through FEM simulation, they estimated that higher power could be obtained from a thin

film PZT generator due to much higher piezoelectric constant. Recently, Marzencki et al. in 2007 improved upon the power generation capabilities of their devices with a thin film AlN cantilever that can generate 1.97 μW from a 4.0g vibration at its resonant frequency of 1368 Hz [63].

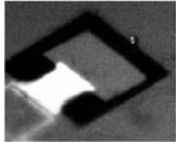
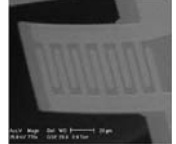
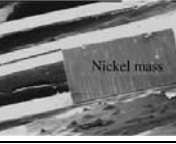
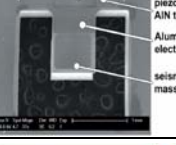
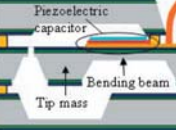
Jeon et al. in 2005 developed a d_{33} mode thin film PZT power generating device with interdigitated electrodes. The device has a dimension of $170 \times 260 \mu\text{m}^2$. The PZT layer was deposited by sol-gel process. The fabricated power generator can generate 1.0 μW power output across a 5.2 M Ω resistive load from a 10.8g vibration at its resonant frequency of 13.9 kHz [64]. The same group in 2006 reported the second generation Piezoelectric Micro Power Generator (PMPG) based on the first generation PMPG described above [65]. They analyzed and modeled the effect of proof mass, beam shape and damping on the power generating performance to provide a design guideline for maximum power harvesting from a given input vibration. Besides, a spiral cantilever is designed to achieve compactness, low resonant frequency and minimum damping coefficient for the application of monitoring the structural integrity of buried pipes.

Fang et al. in 2006 reported the fabrication and performance of a MEMS-based PZT cantilever power generator with a nonintegrated Ni proof mass. This micro power generator has a beam dimension of $2000 \times 600 \times 13.64 \mu\text{m}^3$ and a proof mass dimension of $600 \times 600 \times 500 \mu\text{m}^3$. It can generate 2.16 μW from a 1g vibration at its resonant frequency of 609 Hz [66, 67]. While their demonstrated power density is quite high, the proof mass was not integrated with the cantilever which will be an additional difficulty in production.

Because of the difficulty in fabricating high quality PZT thin film and the complex process procedures during the MEMS PZT-based cantilever with an integrated proof mass at the end tip. This PZT-based micro cantilever with an integrated proof mass did not present until 2007.

Renaud et al. in 2007 and 2008 reported that the fabrication, modeling, and characterization of MEMS piezoelectric cantilever power generator with an integrated proof mass [68, 69]. The PZT-based energy harvester has a Pt/PZT/Pt/Si multi-layer structure, and the PZT was deposited by sol-gel process. The fabricated PZT-based cantilever can generate maximum 40 μ W from a mechanical input driving the generator at its resonant frequency of 1.8 kHz and amplitude of 180 nm. The AlN-based energy harvester has a Al/AlN/Pt/Ta/Si₃N₄/SiO₂/Si multi-layer structure, and the AlN was deposited by reactive sputtering. The maximum power output from the AlN based device was 50 nW from an input vibration at 320 Hz with an amplitude of 45 nm.

Table 2. 3 Summary among current PMPG.

Author	Device	Effective volume (mm ³)	Power (μW)	Power density (μW/cm ³)	<i>A</i> (g)	<i>f</i> (Hz)	Picture or schematic diagram
Marzecki 2005 [62]	d ₃₁ AlN cantilever	3.8 ^a	0.038	10	0.5	204	
Jeon 2005 [64]	d ₃₃ PZT cantilever	0.027 ^a	1.01	37037 ^a	10.8	13.9k	
Fang 2006 [67]	d ₃₁ PZT cantilever	0.1992 ^a	2.16	10843 ^a	1.0	608	
Marzecki 2007 [63]	d ₃₁ AlN cantilever	>0.552 ^a	1.97	< 3569 ^a	4.0	1368	
Renaud 2007 [68]	d ₃₁ PZT cantilever	1.845 ^a	40	21680 ^a	1.9 ^a	1.8k	

^a Estimated from data in reference.

References

- [1] S. P. Beeby, M. J. Tudor, and N. M. White, "Energy harvesting vibration sources for microsystems applications," *Measurement Science and Technology*, vol. 17, pp. 175-195, 2006.
- [2] "IEEE standard on piezoelectricity," New York, 1987.
- [3] J. F. Antaki, G. E. Bertocci, E. C. Green, A. Nadeem, T. Rintoul, R. L. Kormos, and B. P. Griffith, "Gait-powered autologous battery charging system for artificial organs," *ASAIO Journal*, vol. 41, pp. 588-595, 1995.
- [4] M. W. Barsoum, *Fundamentals of Ceramics*. Bristol and Philadelphia: IOP Publishing Ltd, 2003.
- [5] <http://www.piezo.com>.
- [6] <http://www.meas-spec.com/myMeas/default/index.asp>.
- [7] W. Tljlhen, T. Tamagawa, C. P. Ye, C. C. Hsueh, P. Schiller, and D. L. Polla, "Properties of piezoelectric thin films for micromechanical devices and systems," Nara, Jpn, 1991, pp. 114-119.
- [8] K. Tsuchiya, T. Kitagawa, Y. Uetsuji, and E. Nakamachi, "Fabrication of smart material PZT thin films by RF magnetron sputtering, method in micro actuators," *Nihon Kikai Gakkai Ronbunshu, A Hen/Transactions of the Japan Society of Mechanical Engineers, Part A*, vol. 71, pp. 66-72, 2005.
- [9] <http://www.azom.com/Details.asp?ArticleID=610>.
- [10] E. Haeusler, H. Lang, and F. J. Schreiner, "Piezoelectric high power foils as physiological mechanic-electric energy converters," *IEEE/Engineering in Medicine and Biology Society Annual Conference*, pp. 333-334, 1980.
- [11] C. Keawboonchuay, "Maximum Power Generation in a Piezoelectric Pulse Generator," *IEEE Transactions on Plasma Science*, vol. V. 31, No. 1, 2003.
- [12] M. Umeda, K. Nakamura, and S. Ueha, "Analysis of the transformation of mechanical impact energy to electric energy using piezoelectric vibrator," *Japanese Journal of Applied Physics, Part 1: Regular Papers & Short Notes & Review Papers*, vol. 35, pp. 3267-3273, 1996.
- [13] M. Umeda, K. Nakamura, and S. Ueha, "Energy storage characteristics of a piezo-generator using impact induced vibration," *Japanese Journal of Applied Physics, Part 1: Regular Papers & Short Notes & Review Papers*, vol. 36, pp. 3146-3151, 1997.

- [14] T. Funasaka, M. Furuhashi, Y. Hashimoto, and K. Nakamura, "Piezoelectric generator using a LiNbO₃ plate with an inverted domain," *Proceedings of the IEEE Ultrasonics Symposium*, vol. 1, pp. 959-962, 1998.
- [15] P. C. Lysne and C. M. Percival, "Electric energy generation by shock compression of ferroelectric ceramics: normal-mode response of PZT 95/5," *Journal of Applied Physics*, vol. 46, pp. 1519-1525, 1975.
- [16] W. Mock, Jr. and W. H. Holt, "Pulse charging of nanofarad capacitors from the shock depoling of pzt 56/44 and PZT 95/5 ferroelectric ceramics," *Journal of Applied Physics*, vol. 49, pp. 5846-5854, 1978.
- [17] Y.-L. Wang, W.-Z. Yuan, G.-R. He, S.-W. Lin, Y.-H. Ling, C.-F. Qu, and B.-G. Wang, "Study on shock wave-explosive energy converter of PZT 95/5 ferroelectric ceramics," *Ferroelectrics*, vol. 49, pp. 169-176, 1983.
- [18] S. W. Freiman and G. S. White, "Intelligent ceramic materials: Issues of brittle fracture," *Journal of Intelligent Material Systems and Structures*, vol. 6, pp. 49-54, 1995.
- [19] C.-N. Xu, M. Akiyama, K. Nonaka, and T. Watanabe, "Electrical power generation characteristics of PZT piezoelectric ceramics," *IEEE Transactions on Ultrasonics, Ferroelectrics, and Frequency Control*, vol. 45, pp. 1065-1070, 1998.
- [20] C.-N. Xu, M. Akiyama, K. Nonaka, K. Shobu, and T. Watanabe, "Electrical output performance of PZT-based piezoelectric ceramics," East Brunswick, NJ, USA, 1996, pp. 967-970.
- [21] C. Keawboonclinay., "Electrical power generation characteristics of piezoelectric generator under quasi-static and dynamic stress conditions," *IEEE Transactions on Ultrasonics, Ferroelectrics, And Frequency Control*, vol. V. 50, No. 10, Oct. 2003.
- [22] E. S. G. Poulin., F. Costa, "Generation of electrical energy for portable devices: Comparative study of an electromagnetic and a piezoelectric system," *Sensors and Actuators*, vol. A 116, p. 461-471, Received 5 November 2003; received in revised form 28 March 2004; accepted 18 May 2004
- [23] T. Starner, "Human-powered wearable computing," *IBM Systems Journal*, vol. 35, pp. 618-629, 1996.
- [24] C. J. Kendall, "Parasitic power collection in shoe-mounted devices," in *Dept. of Physics and MIT Media Laboratory*. vol. BS: Massachusetts Institute of Technology, 1998.

- [25] J. Kymissis, C. Kendall, J. Paradiso, and N. Gershenfeld, "Parasitic power harvesting in shoes," in *Second International Symposium on Wearable Computers*, Pittsburgh, PA, USA, 1998, pp. 132-139.
- [26] N. Shenck, "A demonstration of useful electric energy generation from piezoceramics in a shoe," in *Dept. of Electrical Engineering and Computer Science*. vol. MS Cambridge, Massachusetts: Massachusetts Institute of Technology, 1999.
- [27] J. Drake, "The Greatest Shoe on Earth," *Wired*, vol. 9, pp. 90-100, 2001.
- [28] N. S. Shenck and J. A. Paradiso, "Energy scavenging with shoe-mounted piezoelectrics," *IEEE Micro*, vol. 21, pp. 30-42, 2001.
- [29] L. Mateu and F. Moll, "Optimum piezoelectric bending beam structures for energy harvesting using shoe inserts," *Journal of Intelligent Material Systems and Structures*, vol. 16, pp. 835-845, 2005.
- [30] M. Ichiki, K. Ashida, and T. Kitahara, "Characterization of piezoelectric lead zirconate titanate from the viewpoint of transducer and power generator properties," *Japanese Journal of Applied Physics, Part 1: Regular Papers and Short Notes and Review Papers*, vol. 41, pp. 7080-7083, 2002.
- [31] S. Kim, W. W. Clark, and Q.-M. Wang, "Piezoelectric energy harvesting with a clamped circular plate: Analysis," *Journal of Intelligent Material Systems and Structures*, vol. 16, pp. 847-854, 2005.
- [32] S. Kim, W. W. Clark, and Q.-M. Wang, "Piezoelectric energy harvesting with a clamped circular plate: Experimental study," *Journal of Intelligent Material Systems and Structures*, vol. 16, pp. 855-863, 2005.
- [33] H. W. Kim, A. Batra, S. Priya, K. Uchino, D. Markley, R. E. Newnham, and H. F. Hofmann, "Energy harvesting using a piezoelectric "cymbal" transducer in dynamic environment," *Japanese Journal of Applied Physics, Part 1: Regular Papers and Short Notes and Review Papers*, vol. 43, pp. 6178-6183, 2004.
- [34] H. W. Kim, S. Priya, K. Uchino, and R. E. Newnham, "Piezoelectric energy harvesting under high pre-stressed cyclic vibrations," *Journal of Electroceramics*, vol. 15, pp. 27-34, 2005.
- [35] H. Kim, S. Priya, and K. Uchino, "Modeling of piezoelectric energy harvesting using cymbal transducers," *Japanese Journal of Applied Physics, Part 1: Regular Papers and Short Notes and Review Papers*, vol. 45, pp. 5836-5840, 2006.
- [36] S. Roundy, P. K. Wright, and J. Rabaey, "A study of low level vibrations as a power source for wireless sensor nodes," *Computer Communications*, vol. 26, pp. 1131-1144, 2003.

- [37] S. Roundy and P. K. Wright, "A piezoelectric vibration based generator for wireless electronics," *Smart Materials and Structures*, vol. 13, pp. 1131-1142, 2004.
- [38] Shad Roundy, Brian P. Otis, Yuen-Hui Chee, Jan M. Rabaey, and P. Wright, "A 1.9ghz rf transmit beacon using environmentally scavenged energy," in *ISPLED*, Seoul, Korea, 2003.
- [39] S. Roundy, E. S. Leland, J. Baker, E. Carleton, E. Reilly, E. Lai, B. Otis, J. M. Rabaey, P. K. Wright, and V. Sundararajan, "Improving power output for vibration-based energy scavengers," *IEEE Pervasive Computing*, vol. 4, pp. 28-36, 2005.
- [40] S. Roundy, "On the effectiveness of vibration-based energy harvesting," *Journal of Intelligent Material Systems and Structures*, vol. 16, pp. 809-823, 2005.
- [41] S. Roundy and Y. Zhang, "Toward self-tuning adaptive vibration based micro-generators," Sydney, Australia, 2005, pp. 373-384.
- [42] G. K. Ottman, H. F. Hofmann, A. C. Bhatt, and G. A. Lesieutre, "Adaptive piezoelectric energy harvesting circuit for wireless remote power supply," *IEEE Transactions on Power Electronics*, vol. 17, pp. 669-676, 2002.
- [43] G. K. Ottman, H. F. Hofmann, and G. A. Lesieutre, "Optimized piezoelectric energy harvesting circuit using step-down converter in discontinuous conduction mode," *IEEE Transactions on Power Electronics*, vol. 18, 2003.
- [44] http://www.efunda.com/storefront/product_detail.cfm?prod=328.
- [45] H. A. Sodano, G. Park, D. J. Leo, and D. J. Inman, "Model of piezoelectric power harvesting beam," Washington, DC., United States, 2003, pp. 345-354.
- [46] H. A. Sodano, G. Park, and D. J. Inman, "Estimation of electric charge output for piezoelectric energy harvesting," *Strain*, vol. 40, pp. 49-58, 2004.
- [47] H. A. Sodano, "Macro-fiber composites for sensing, actuation and power generation," in *Thesis Virginia Polytechnic Institute and State University*, 2003.
- [48] H. A. Sodano, G. Park, and D. J. Inman, "An investigation into the performance of macro-fiber composites for sensing and structural vibration applications," *Mechanical Systems and Signal Processing*, vol. 18, pp. 683-697, 2004.
- [49] <http://www.smart-material.com/index.php>.
- [50] H. A. Sodano, "A review of power harvesting from vibration using piezoelectric materials," *The Shock and Vibration Digest*, vol. V. 36, No. 3,, pp. 197-205, May 2004.

- [51] H. A. Sodano, D. J. Inman, and G. Park, "Comparison of piezoelectric energy harvesting devices for recharging batteries," *Journal of Intelligent Material Systems and Structures*, vol. 16, pp. 799-807, 2005.
- [52] H. A. Sodano, J. Lloyd, and D. J. Inman, "An experimental comparison between several active composite actuators for power generation," *Smart Materials and Structures*, vol. 15, pp. 1211-1216, 2006.
- [53] S. Priya, "Modeling of electric energy harvesting using piezoelectric windmill," *Applied Physics Letters*, vol. 87, pp. 184101-3, 2005.
- [54] S. Priya, C.-T. Chen, D. Fye, and J. Zahnd, "Piezoelectric windmill: a novel solution to remote sensing," *Japanese Journal of Applied Physics, Part 2: Letters*, vol. 44, pp. 104-107, 2005.
- [55] M. J. Ramsay and W. W. Clark, "Piezoelectric energy harvesting for bio MEMS applications," Newport Beach, CA, 2001, pp. 429-438.
- [56] C. B. Williams and R. B. Yates, "Analysis of a micro-electric generator for microsystems," *Sensors and Actuators A: Physical*, vol. 52, pp. 8-11, 1996.
- [57] N. M. White, P. Glynne-Jones, and S. P. Beeby, "A novel thick-film piezoelectric micro-generator," *Smart Materials and Structures*, vol. 10, pp. 850-852, 2001.
- [58] S. Zurn, M. Hsieh, G. Smith, D. Markus, M. Zang, G. Hughes, Y. Nam, M. Arik, and D. Polla, "Fabrication and structural characterization of a resonant frequency PZT microcantilever," *Smart Materials and Structures*, vol. 10, pp. 252-263, 2001.
- [59] I. Demir, A. L. Olson, J. L. Skinner, C. D. Richards, R. F. Richards, and D. F. Bahr, "High strain behavior of composite thin film piezoelectric membranes," Phoenix, AZ, United States, 2004, pp. 12-23.
- [60] H. L. a. S. P. L. F Lu, "Modeling and analysis of micro piezoelectric power generators for micro-electromechanical-systems applications," *Smart Mater. Struct.*, vol. 13, pp. 57-63, Received 12 August 2002, in final form 16 September 2003
- [61] M. Marzencki, S. Basrour, and B. Charlot, "Design, modelling and optimisation of integrated piezoelectric micro power generators," Anaheim, CA, United States, 2005, pp. 545-548.
- [62] M. Marzencki, B. Charlot, S. Basrour, M. Colin, and L. Valbin, "Design and Fabrication of Piezoelectric Micro Power Generators for Autonomous Microsystems," in *DTIP '05 - Symposium on Design Testing Integration and Packaging of MEMS/MOEMS* Montreux, Switzerland, 2005, pp. 299-302.

- [63] M. Marzencki, Y. Ammar, and S. Basrour, "Integrated Power Harvesting System Including a MEMS Generator and a Power Management Circuit," in *Solid-State Sensors, Actuators and Microsystems Conference, Transducers International*, 2007, pp. 887-890.
- [64] Y. B. Jeon, R. Sood, J. h. Jeong, and S. G. Kim, "MEMS power generator with transverse mode thin film PZT," *Sensors and Actuators A: Physical*, vol. 122, pp. 16-22, 2005.
- [65] W. J. Choi, Y. Jeon, J. H. Jeong, R. Sood, and S. G. Kim, "Energy harvesting MEMS device based on thin film piezoelectric cantilevers," *Journal of Electroceramics*, vol. 17, pp. 543-548, 2006.
- [66] H. Fang, J. Liu, Z. Zheng, L. Dong, D. Chen, B. Cai, and Y. Liu, "A MEMS-Based Piezoelectric Power Generator for Low Frequency Vibration Energy Harvesting," *Chin. Phys. Lett.*, vol. 23, pp. 732-734, 2006.
- [67] H.-B. Fang, J.-Q. Liu, Z.-Y. Xu, L. Dong, L. Wang, D. Chen, B.-C. Cai, and Y. Liu, "Fabrication and performance of MEMS-based piezoelectric power generator for vibration energy harvesting," *Microelectronics Journal*, vol. 37, pp. 1280-1284, 2006.
- [68] M. Renaud, T. Sterken, A. Schmitz, P. A. F. P. Fiorini, C. A. V. H. C. Van Hoof, and R. A. P. R. Puers, "Piezoelectric Harvesters and MEMS Technology: Fabrication, Modeling and Measurements," in *Solid-State Sensors, Actuators and Microsystems Conference, Transducers International*, 2007, pp. 891-894.
- [69] M. Renaud, K. Karakaya, T. Sterken, P. Fiorini, C. Van Hoof, and R. Puers, "Fabrication, modeling and characterization of MEMS piezoelectric vibration harvesters," *Sensors and Actuators, A: Physical*, vol. 145-146, pp. 380-386, 2008.

CHAPTER 3

DESIGN, OPTIMIZATION AND DEMONSTRATION OF BULK PROTOTYPES

3.1 Material selection, configuration design, analytical modeling, and dimension optimization

3.1.1 Material selection and configuration design

Three configurations were usually utilized for piezoelectric power harvesting device. They are diaphragm, bridge, and cantilever as shown in Figure 3-1. The fixed-free cantilever configuration with a proof mass at the free end was selected for two reasons. First, this one-edge clamped configuration can generate larger strain and thereby higher power compared to two-edge clamped bridge and all-edge clamped diaphragm at the same input force. Second, it can easily realize low resonant frequency corresponding to most vibration sources in our living environment as well as the vibration frequency, 100 Hz at which this research aimed.

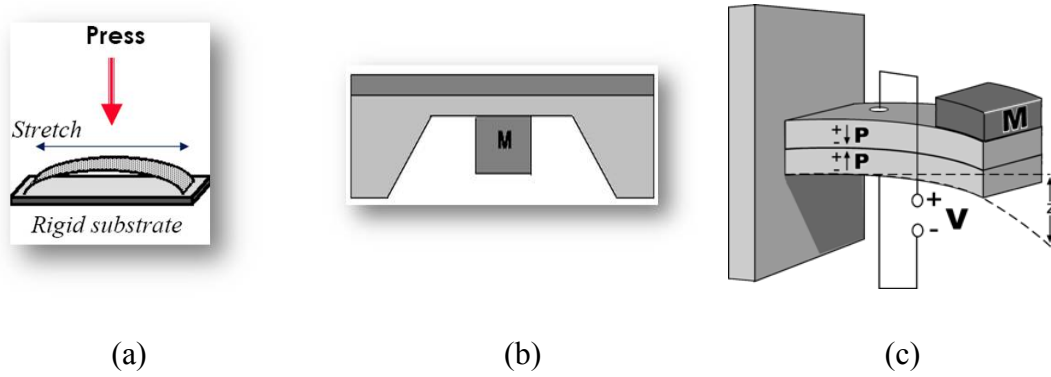
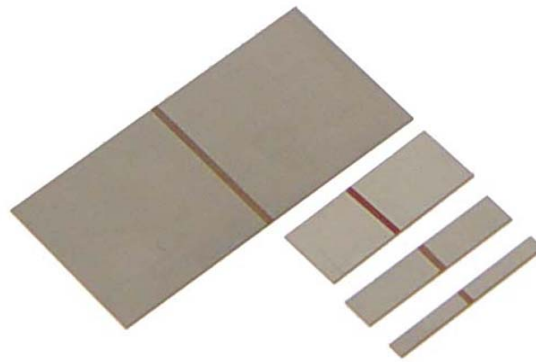
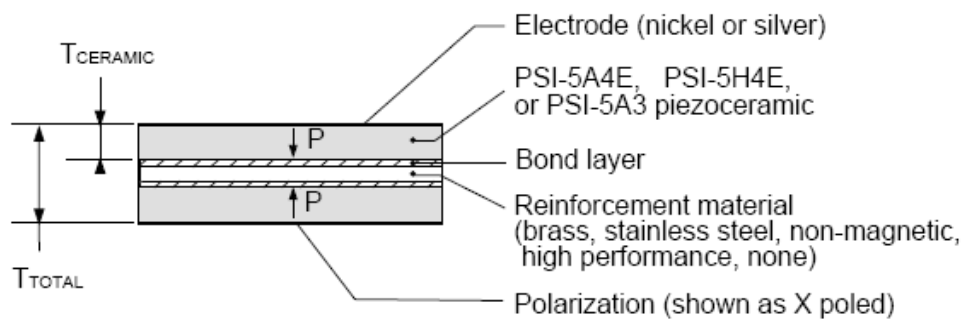


Figure 3- 1 Schematic diagrams of three common configurations (a) diaphragm (b) bridge (c) cantilever of piezoelectric power harvester.

One of commercial PZT-5H bimorph bender (T-215-H4-103Y) was selected from Piezo Systems Inc. as the piezoelectric transducer by miniaturizing the prototype based on the available commercial products. The bimorph bender consists of a metal shim (brass) sandwiched by two thin layers of PZT material, as shown in Figure 3-2. Tungsten was used as the material of the proof mass due to high density.



(a)



(b)

Figure 3- 2 (a) Picture of bimorph cantilever bender; (b) schematic diagram of the layer structure of bimorph cantilever bender [1].

Figure 3-3 shows the schematic diagram of the configuration of designed cantilever and the notations used for calculation, where the two bonding layers were neglected because they are very thin.

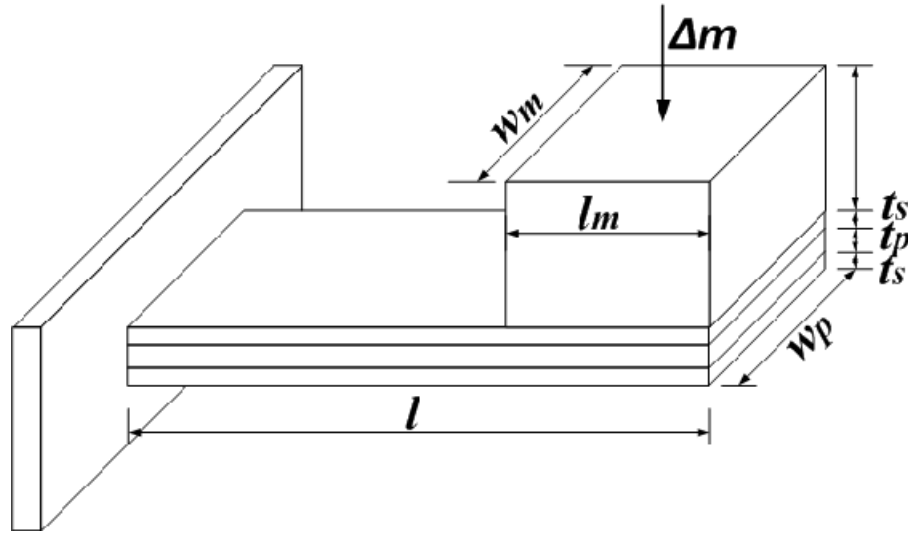


Figure 3- 3 Schematic diagram of bimorph cantilever configuration and notations.

3.1.2 Analytical modeling and optimization on the dimension of bulk PZT prototype

There are three key factors that we need to consider during the optimization design of the PZT energy harvester. They are the resonant frequency, the output power density, and the safety factor, which will be elaborated in this section.

The resonant frequency of the generator was primarily analyzed to design the piezoelectric power generator prototype with the wanted resonant frequency since the maximum power (generated or converted) can only be achieved when the resonant frequency of the generator is matching the frequency of the vibration source. The safety of generator has to be considered due to the high fragility of piezoelectric ceramic. By compromise between the maximum power and safety issue, the optimal designs of cantilever generator were finally achieved.

3.1.2.1 Analysis on the resonant frequency of the piezoelectric cantilever

The resonant frequency of the piezoelectric energy converter is one of the most important factors influencing the converting efficiency of a device from mechanical energy to electrical energy. It must be designed to match the environmental vibration frequency, which is the prerequisite to maximize the output power. It was reported orders of reduction in power output even for a small deviation of vibration frequency from the resonant frequency [2].

Generally, the resonant frequency can be calculated by [3]:

$$f_r = \frac{\omega}{2\pi} = \frac{1}{2\pi} \sqrt{\frac{K}{m_e}} \quad (3-1)$$

where f_r is the resonant frequency; ω is the angular frequency; K is the spring constant at the tip of the cantilever, m_e is the effective mass of the cantilever.

To calculate the resonant frequency of a cantilever without a proof mass, high accuracy can be expected using most published Equations [3-5]. For cantilevers with proof mass, the proof mass was considered as a point mass in most published equations. This simplification was effective to some degree, especially when the proof mass was rather smaller than the length of the whole cantilever. There are two methods were selected as candidates to calculate the resonant frequency of cantilevers without proof mass.

The resonant frequency of a cantilever (clamped-free structure) without a proof mass can be expressed in terms of the flexural rigidity EI [6] by:

$$f_n = \frac{v_n^2}{2\pi} \frac{1}{l^2} \sqrt{\frac{EI}{m'}} \quad (3-2)$$

or in terms of the bending modulus per unit width E_0 ($E_0 = EI/w$) [5, 7] by:

$$f_n = \frac{v_n^2}{2\pi} \frac{1}{l^2} \sqrt{\frac{E_0}{m}} \quad (3-3)$$

where f_n is the n^{th} mode resonant frequency, v_n the n^{th} mode eigenvalue, l the length of the cantilever, E the modulus of elasticity, I the area moment of inertia about the neutral axis, m' the mass per unit length of the cantilever beam, w the width of the cantilever. For a bimorph laminated composite cantilever, E_0 is a function of the Young's moduli of the two materials, E_p (PZT) and E_s (brass), and their thicknesses, t_p and t_s where:

$$E_0 = \frac{2E_p t_p^3}{3} + E_p t_s t_p^2 + \frac{E_p t_s^2 t_p}{2} + \frac{t_s^3 E_s}{12} \quad (3-4)$$

and the mass per unit area m is calculated from the thicknesses and densities, ρ_p and ρ_s , of the two materials by:

$$m = 2\rho_p t_p + \rho_s t_s \quad (3-5)$$

The resonant frequency of a cantilever with a point proof mass positioned at the free end tip can be approximated by [5]:

$$f'_n = \frac{v_n'^2}{2\pi} \sqrt{\frac{K}{m_e + \Delta m}} \quad (3-6)$$

where $v_n'^2 = v_n^2 \sqrt{0.236/3}$, the effective mass of the cantilever at the tip $m_e = 0.236mwl$, Δm the mass of the point proof mass added at the free end tip, and K is the effective spring constant at the tip of the cantilever given by:

$$K = \frac{3D_p w_p}{l^3} \quad (3-7)$$

However, when the proof mass is distributed across an area rather than through a point at the end tip it can be treated as a concentrated point load directed through its center of mass. For a distributed proof mass with uniform density and rectangular symmetry located at the free end tip, the center of mass is at a distance of $l_m/2$ from the end tip. The effective spring constant of the cantilever at this location K' is related to the end tip effective spring constant K by [8]:

$$K' = K \left(\frac{l}{l - l_m / 2} \right)^3 \quad (3-8)$$

Substituting K' for K in Equation (3-7), the resonant frequency of a bimorph composite cantilever with a large proof mass located at the free end tip is thus:

$$f'_n = \frac{v_n^2}{2\pi} \sqrt{\frac{0.236E_0w_p}{0.236mw_p(l - l_m / 2)^4 + \Delta m(l - l_m / 2)^3}} \quad (3-9)$$

$$\Delta m = \rho_m l_m w_m h_m \quad (3-10)$$

where ρ_m , l_m , w_m , and h_m are the density, length, width, and height of the proof mass.

Parameter designs of cantilever beams were considered to calculate the resonant frequencies using the above equations. The targeted resonant frequency was attained by changing the lengths and widths of the cantilever beam and the dimensions of the proof mass.

For experimental verification of output power density, the total volume of cantilever was kept within 0.1 cm^3 . Three 3D plots about calculated resonant frequencies are shown in Figures 3-4, 3-5, and 3-6.

For the first plot, Figure 3-4, it shows the relationship between the resonant frequency and the length of PZT and the length of the proof mass, where $l_p = l - l_m$, was

changing from 1 mm to 20 mm; l_m was changing from 1mm to 10mm; the length of the electrode: $l_e = l_p + l_m$; $t_p = 0.134$ mm, $t_s = 0.123$ mm, and $w_p = 3.2$ mm, which are the typical values measured from commercial PZT bender (Piezo System Co.); the height of proof mass: $h_m = 6.77$ mm, which is the height of the commercial tungsten bulk; the width of the proof mass: $w_m = \frac{0.1\text{cm}^3 - (l_p + l_m)w_p(t_s + 2t_p)}{h_m l_m}$ to limit the total volume of the cantilever power generator smaller than 0.1 cm^3 . All parameter values were selected according to the wanted resonant frequency, 100 Hz. And, the tungsten was selected as the proof mass because of its high density, which is $\rho_m = 19300 \text{ kg/m}^3$.

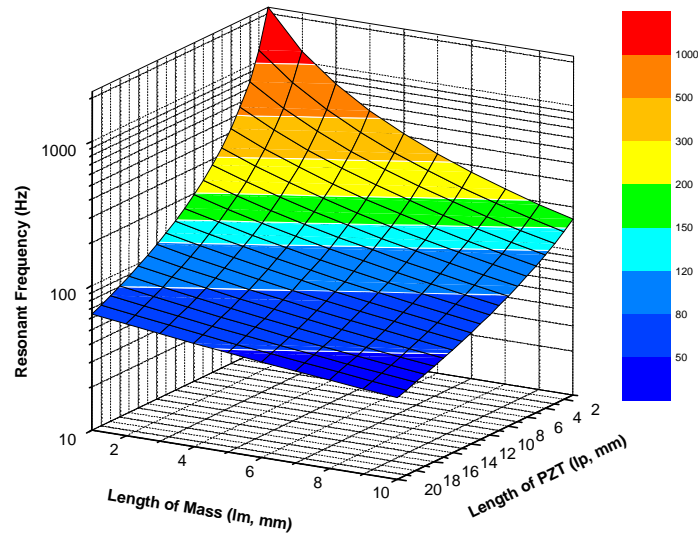


Figure 3- 4 Resonant frequency as a function of lengths of PZT and proof mass in the dimensions of cantilever beam.

For the second plot, Figure 3-5, it shows the relationship between the resonant frequency and the thickness of PZT and the thickness of the shim, where $l_p = 12$ mm; $l_m = 3$ mm; t_p was changing from 0.05 mm to 0.15 mm, t_s was changing from 0.05 mm to 0.25 mm; $l_e = l_p + l_m$; $w_p = 3.2$ mm; $h_m = 6.77$ mm; $w_m = \frac{0.1cm^3 - (l_p + l_m)w_p(t_s + 2t_p)}{h_m l_m}$. All parameter values were also selected according to the wanted resonant frequency, 100Hz.

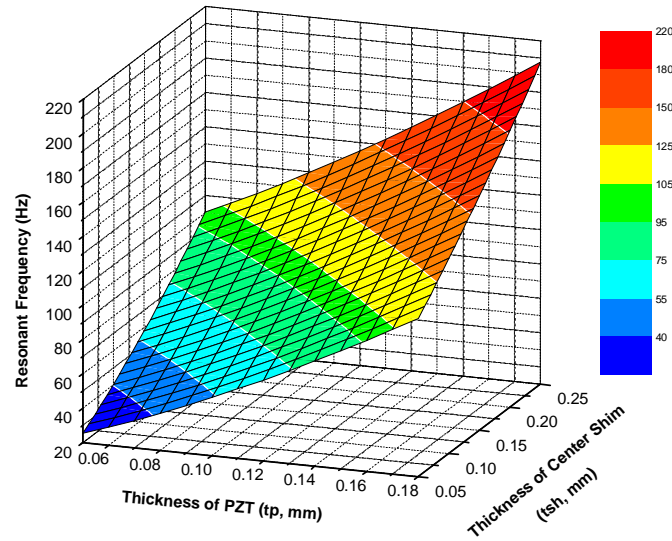


Figure 3- 5 Resonant frequency as a function of thicknesses of PZT and shim in the dimensions of cantilever beam.

For the third plot, Figure 3-6, it shows the relationship between the resonant frequency and the width of PZT and the height of the proof mass, where $l_p = 12$ mm; $l_m = 3$ mm; $l_e = l_p + l_m$; $t_p = 0.134$ mm, $t_{sh} = 0.123$ mm; w_p was changing from 2.5 mm to 4.5

mm, h_m was changing from 4 mm to 9 mm; $w_m = \frac{0.1cm^3 - (l_p + l_m)w_p(t_{sh} + 2t_p)}{h_m l_m}$. All

parameter values were again selected according to the wanted resonant frequency, 100Hz.

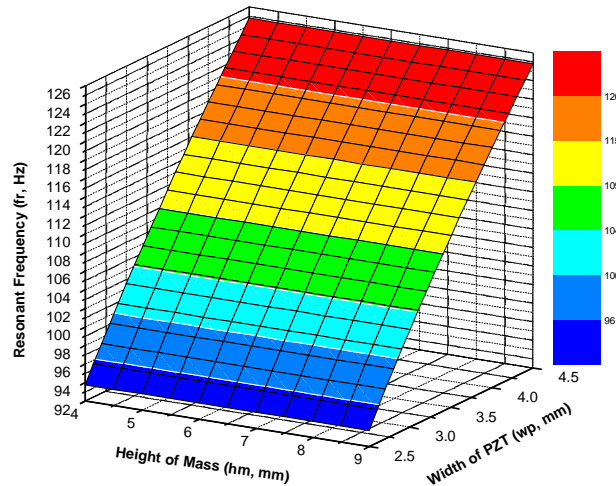


Figure 3- 6 Resonant frequency as a function of PZT width and height of proof mass in the dimensions of cantilever beam.

From these three 3D plots, it is verified that the resonant frequency decreases with increasing both the lengths of PZT and the mass, decreases with decreasing both thicknesses of PZT and the shim metal, and increases with increasing the width of the beam, but retain constant with changing the height of the proof mass.

Comparing with experimental values, calculations match reasonable within 10%. The observed errors between calculation and experiment are considered resulting from

the negligence of bonding materials and non-precise attachment of the proof mass on cantilever beam.

These simulations helped us to design the optimal dimensions of cantilever power generator with wanted resonant frequency after considering together with the simulations of output power and safety issues.

3.1.2.2 Analysis on the output power of the piezoelectric cantilever

Piezoelectric transformers can be analyzed using lumped-constant equivalent circuit or distributed-constant equivalent circuit. Generally, the lumped-constant equivalent circuit is easily calculated, compared with the distributed-constant equivalent circuit. The element values, used in a lumped-constant equivalent circuit, are those approximated near the resonant frequency.

Figure 3-7 shows the lumped-constant equivalent circuit for the piezoelectric transformer, where L : equivalent inductance, C : equivalent capacitance, R : equivalent resistance, n : transformation ratio, R_L : resistive load.

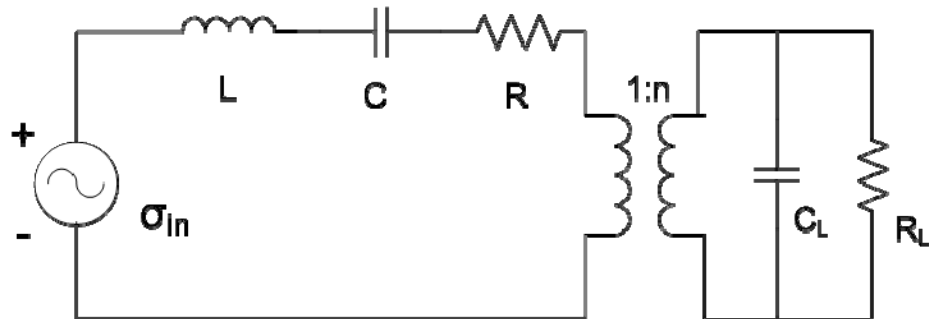


Figure 3- 7 Schematic diagram of the electronic equivalent circuit.

The output power analysis was performed based on the reported model [9], which is based on the electric equivalent circuit model for a PZT beam in Figure 3-7, where a voltage source connects in series to an inductor, a resistor and a capacitor that build in a resonant circuit.

Output power was calculated by Equation (3-11) which was derived by combining the standard beam equations with the constitutive piezoelectric equations and RC circuit equations. While the RC circuit was oversimplified, it was reported to give a reasonably good approximation of the amount of power generated.

$$P = \frac{|V|^2}{R_{Opt}} \quad (3-11)$$

$$V = \frac{-j\omega \frac{E_p d t_p b^*}{\epsilon}}{\left[\frac{1}{RC} \omega_r^2 - \left(\frac{1}{RC} + 2\zeta \omega_r \right) \omega^2 \right] + j\omega \left[\omega_r^2 (1 + k^2) + \frac{2\zeta \omega_r}{RC} - \omega^2 \right]} A_{in} \quad (3-12)$$

$$R_{Opt} = \frac{2\zeta}{\omega C \sqrt{4\zeta^2 + k^2}} \quad (3-13)$$

$$b^* = \frac{3b (2l_p + l_m - l_e)}{l_b^2 (2l_p + 1.5l_m)} \quad (3-14)$$

where P and V are respectively the power and voltage generated by the cantilever device, R_{Opt} the optimal resistance of resistor load, ω the angular frequency of the input signal and equal to the resonant frequency of the cantilever ω_r , C the capacitance of the bimorph cantilever beam, d the piezoelectric coefficient of PZT (3.2×10^{-10} m/V), l_p , and l_e the lengths of PZT and the electrode respectively (they are equal here), b the distance from the center of PZT layer to the center of the metal layer, ϵ the dielectric constant of PZT

$(3.36 \times 10^{-8} \text{ F/m})$, A_{in} the input acceleration (1 g, the acceleration of gravity), ζ the damping ratio of cantilever (0.02), k the coupling coefficient of PZT (0.44).

From these calculations, the values of the power density show the trend that the output power increases with increasing the lengths of the mass, but decreases first and then increases with increasing the length of PZT. It also increases with decreasing both thicknesses of PZT and metal, and increases with decreasing the width of PZT but retains constant with increasing the height of the mass. Relationships are shown as 3D plots in Figures 3-8, 3-9, and 3-10.

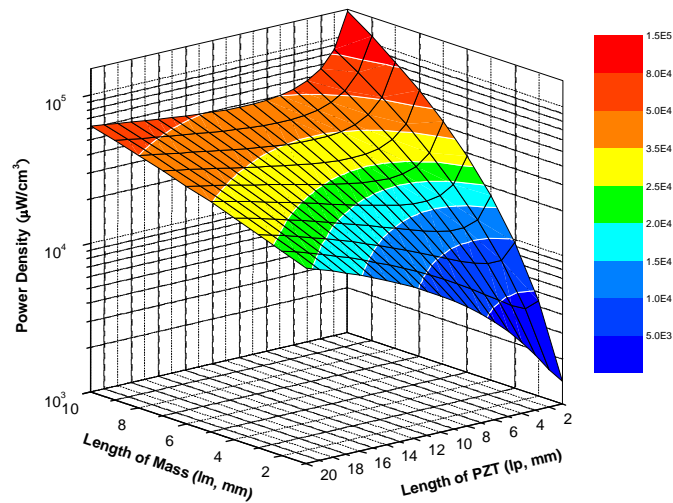


Figure 3- 8 Power density as a function of lengths of PZT and proof mass in the dimensions of cantilever beam.

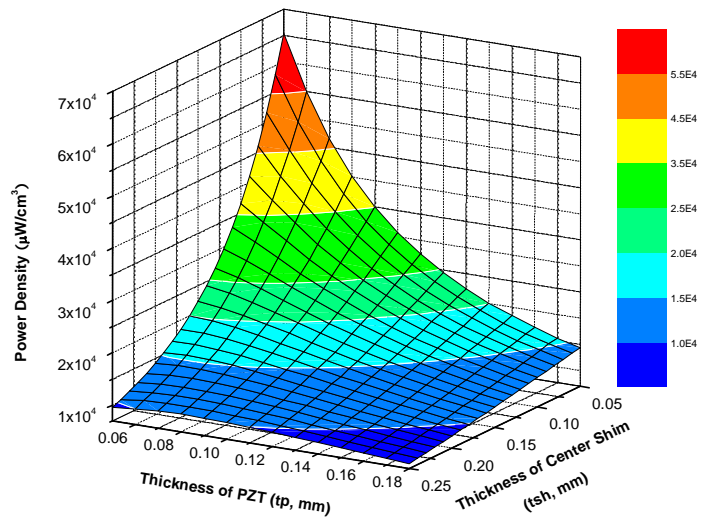


Figure 3- 9 Power density as a function of thicknesses of PZT and shim in the dimensions of cantilever beam.

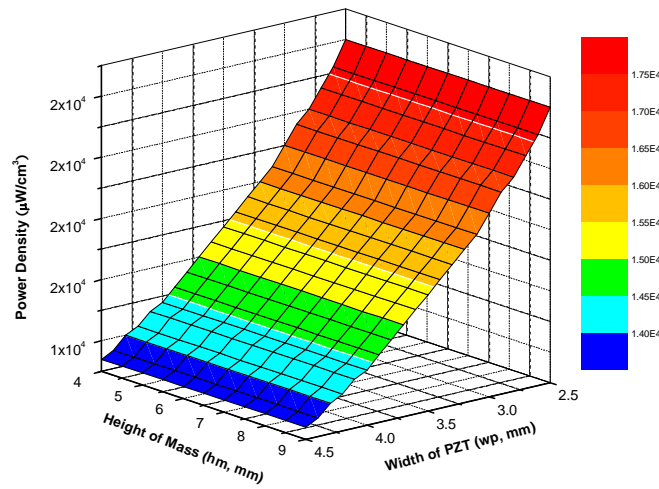


Figure 3- 10 Power density as a function of PZT width and height of proof mass in the dimensions of cantilever beam.

3.1.2.3 Analysis on the safety factor and the dimension optimization of the piezoelectric cantilever

The power density reaches highest value when the resonant frequency of cantilever beams is equal to the driving vibration frequency. Power conversion is maximized when larger strain was generated in the PZT beam, i.e. higher deflection of PZT beam. However, such structure is very vulnerable for fracture of ceramic PZT materials under high-g conditions, which may limit the applications requiring severe vibration conditions such as vehicle. To evaluate the robustness of cantilever structure, safety factor was introduced and calculated by:

$$S = \frac{\sigma_{ys}}{\sigma_{max}} \quad (3-15)$$

where σ_{ys} is the yield strength of PZT-5H ceramic ($\sim 20 \text{ MPa}$), and σ_{max} the maximum stress generated at the surface of PZT bender around the clamping area, which was calculated at 1 g acceleration by:

$$\sigma_{max} = \frac{M(\frac{t_{sh}}{2} + t_p)}{I} \quad (3-16)$$

$$M = \Delta m(\dot{y} + \ddot{z})(l_p + \frac{l_m}{2}) \quad (3-17)$$

$$\Delta m(\dot{y} + \ddot{z}) = \frac{2E_p I}{b(2l_p + l_m - l_e)} \delta = \frac{2E_p I}{bl_p} \delta \quad (3-18)$$

$$\delta = |V| \frac{\varepsilon}{dE_p t_p} \quad (3-19)$$

$$V = \frac{-j\omega \frac{E_p dt_p b^*}{\varepsilon}}{\left[\frac{1}{RC} \omega_r^2 - \left(\frac{1}{RC} + 2\zeta\omega_r \right) \omega^2 \right] + j\omega \left[\omega_r^2 (1+k^2) + \frac{2\zeta\omega_r}{RC} - \omega^2 \right]} A_{in} \quad (3-20)$$

$$b^* = \frac{3b (2l_p + l_m - l_e)}{l_b^2 (2l_p + 1.5l_m)} \quad (3-21)$$

$$C = \frac{2\varepsilon w l_e}{t_p} \quad (3-22)$$

where M is the moment of the cantilever with proof mass, t_s and t_p respectively the thicknesses of the shim metal and the PZT, I the moment of inertia of the cantilever, Δm the proof mass, \ddot{y} the input driving acceleration, z the vertical displacement of the cantilever tip with proof mass, here the tip was simplified at the middle of the proof mass, l_p , l_m , and l_e respectively the lengths of the PZT bender, the proof mass, and the electrode on the PZT, and here the total length of the cantilever is the sum of l_p and l_m , and $l_e = l_p + l_m$, E_p the Young's modulus of PZT, b the distance from the thickness center of the PZT to the thickness center of the shim metal, δ the strain generated in the PZT, V the potential generated in PZT, ε the dielectric constant of PZT, d the piezoelectric constant of PZT (3.2×10^{-10} m/V here), R the resistance of load, C the capacitance of the cantilever device, ω the frequency of the input driving vibration, ω_r the resonant frequency of the cantilever with proof mass, ζ the damping ration of the device (0.02 here), k the coupling coefficient of PZT (0.44 here), w the width of the PZT bender.

The calculated results regarding safety factor were plotted in Figure 3-11 to Figure 3-13. For the first plot, Figure 3-11, it shows the relationship between the safety

factor and the length of PZT and the length of the proof mass. All parameters have the same values or limitations as the calculation of the resonant frequency in Figure 3-5.

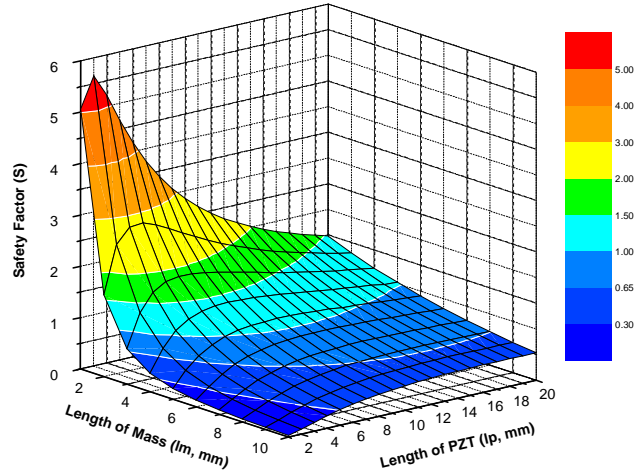


Figure 3- 11 Safety factor as a function of lengths of PZT and proof mass in the dimensions of cantilever beam.

For the second plot, Figure 3-12, it shows the relationship between the safety factor and the thickness of PZT and the thickness of the shim. All parameters have also the same values or limitations as the calculation of the resonant frequency in Figure 3-6.

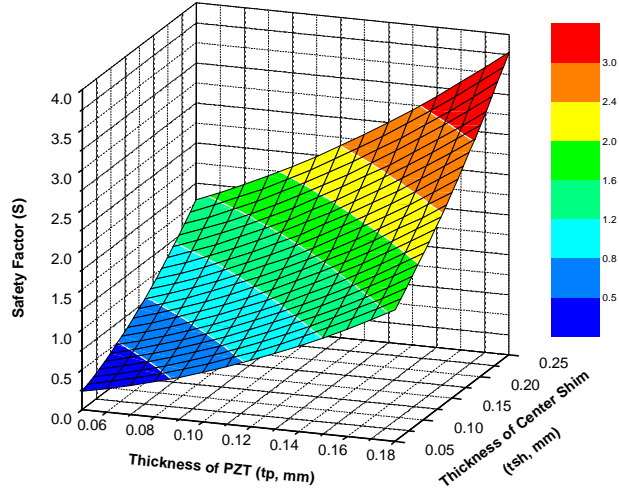


Figure 3- 12 Safety factor as a function of thicknesses of PZT and shim in the dimensions of cantilever beam.

For the third plot, Figure 3-13, it shows the relationship between the resonant frequency and the width of PZT and the height of the proof mass. All parameters have again the same values or limitations as the calculation of the resonant frequency in Figure 3-7.

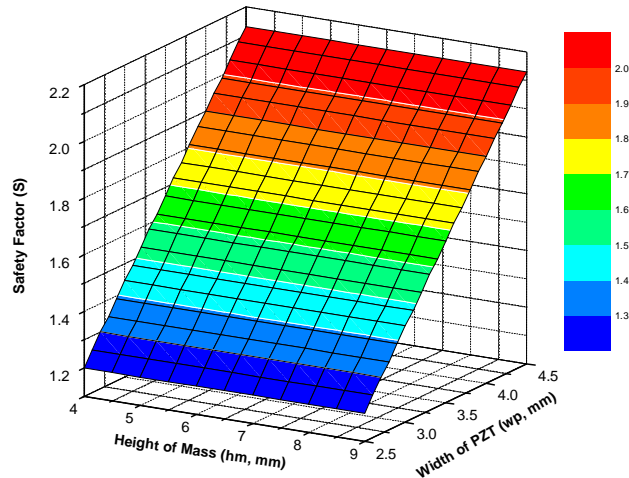


Figure 3- 13 Safety factor as a function of PZT width and height of proof mass in the dimensions of cantilever beam.

It is clear that the safety factor exhibits opposite trends to power. The safety factor decreases with increasing the lengths of the proof mass and decreasing the length of PZT, decreases with decreasing both thicknesses of PZT and the shim metal, and decreases with decreasing the width of PZT and increasing the height of mass. Therefore, the power conversion devices should be designed to achieve the robustness and longevity. Experimental verification under continuous load cycle is currently being investigated.

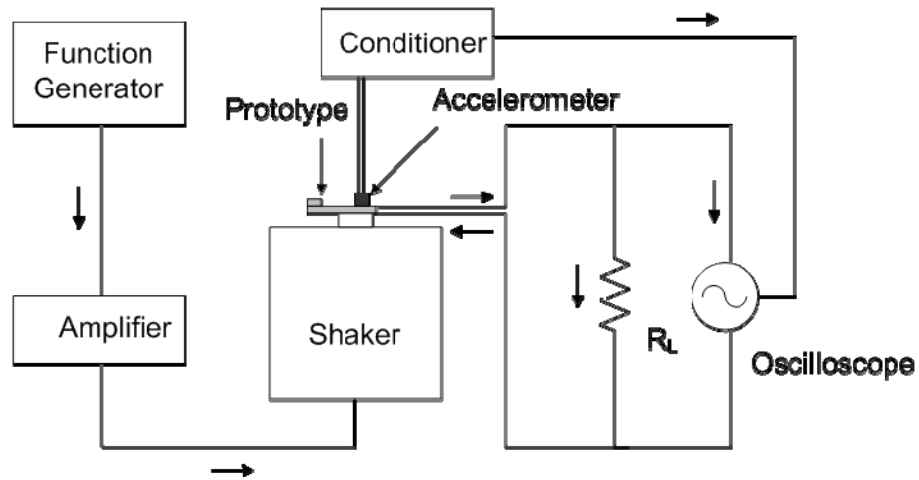
3.2 Experimental setup and measurement

The resonant frequency of the fabricated prototype was measured first using impedance analyzer (Agilent Technologies, 4294A) as shown in Figure 3-14.

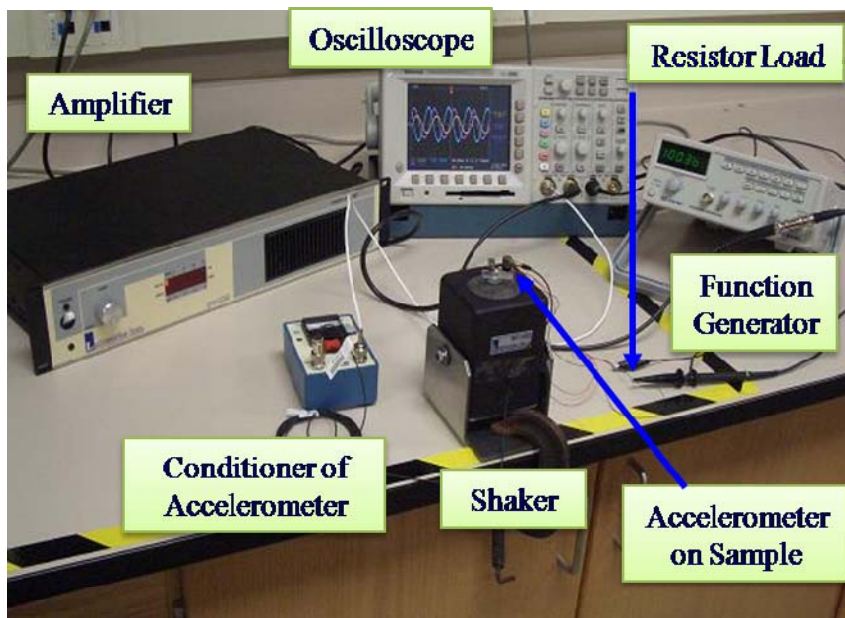


Figure 3- 14 Picture of Impedance analyzer 4294A (Agilent Technologies).

The fabricated cantilever generator was then evaluated using the simple resistance load. Vibration frequency was set at the value of the resonant frequency of the cantilever prototype, and optimal resistance, where maximum power reached, was found. When fixed the resistance value of the load, the trend of power versus vibration frequency was attained. Figure 3-15 (a) shows the schematic of experimental setup; while, Figure 3-15 (b) is the picture of the real setup.



(a)



(b)

Figure 3- 15 (a) Schematic diagram and (b) picture of experimental setup with a simple resistive load.

First, fixed the clamp of the generator onto the magnetic shaker with double-sided type, and then connected the positive and negative wires of the generator with a resistor. Second, the accelerometer (PCB Piezoelectronics Inc., 352C65) was attached onto the clamp to monitor the acceleration generated by the shaker, and a conditioner (PCB Piezoelectronics Inc., 480C02) was used to supply power to the accelerometer. Third, input sine wave signal was produced by the functional generator (Instek GFG-8216A), which was also used to control the vibration frequency. And, then the signal was amplified by an amplifier (Labworks Inc. PA-119), which was also used to control the magnitude or acceleration of the vibration. After the amplifier, the signal went into the shaker (Labworks Inc., ET-132-203), which was used to generate the vibration. Finally, the output signal in voltage from the generator was read out by an oscilloscope (Tektronix TDS 3014B). At the same time, the acceleration information output from the accelerometer and the output sine wave signal from the function generator were also monitored through the oscilloscope.

3.3 Results and discussion

The optimized cantilever device, with a safety factor higher than 10, was fabricated with a PZT-5H bender and tungsten mass to characterize power conversion from vibration, as shown in Figure 3-16.

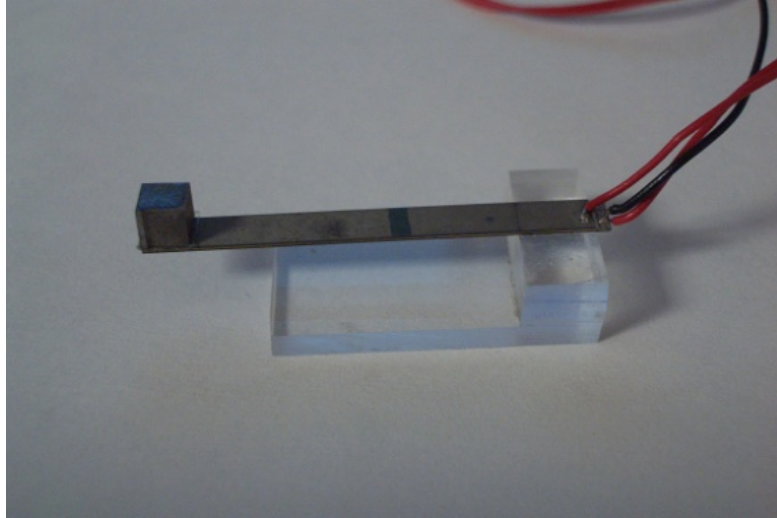


Figure 3- 16 Picture of the optimized PZT cantilever prototype.

The detailed dimensions and resonant frequencies of this power generation device are presented in Table 3-1.

Table 3. 1 Dimensions and frequency of the optimized PZT bulk power generator prototype with a safety factor over 10.

l (mm)	w_p (mm)	t_p (mm)	t_s (mm)	l_m (mm)	w_m (mm)	h_m (mm)	E_p (GPa)	E_s (GPa)	Δm (g)	Cal. f_r (Hz)	Mea. f_r (Hz)	%
25.2*	3.2*	0.134*	0.123*	3.2	3.0	3.0	62*	110*	5.56	95.8	97.6	1.9

* Predetermined value by the commercially available PZT-5H bender

The resonant frequency, the peak frequency of phase angle versus frequency, of this device was measured of 97.6 Hz, as shown in Figure 3-17. The calculated resonant frequency by equation (3-9) is 95.8 Hz. The difference between the measured and calculated resonant frequency is about 1.85%, which demonstrate that the calculation method is accurate to predict the resonant frequency of a bimorph cantilever with a non-point proof mass.

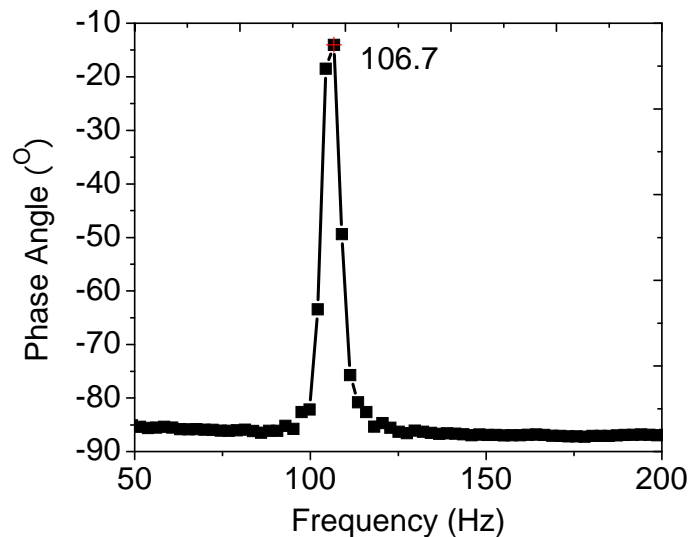


Figure 3- 17 Measured resonant frequency of the optimized bulk PZT prototype.

The output behavior of the optimized power generator was then evaluated at different resistive loads, different vibration frequencies, and different acceleration amplitudes. First, the optimal resistive load at 1g acceleration was obtained by changing the resistance of the resistive load. The peak voltage of AC output and the calculated

power versus the resistive load are presented in Figure 3-18. With increasing resistance of load, the output voltage increases abruptly at the beginning and then slowly. The maximum power output appears at 75 Ω resistive load.

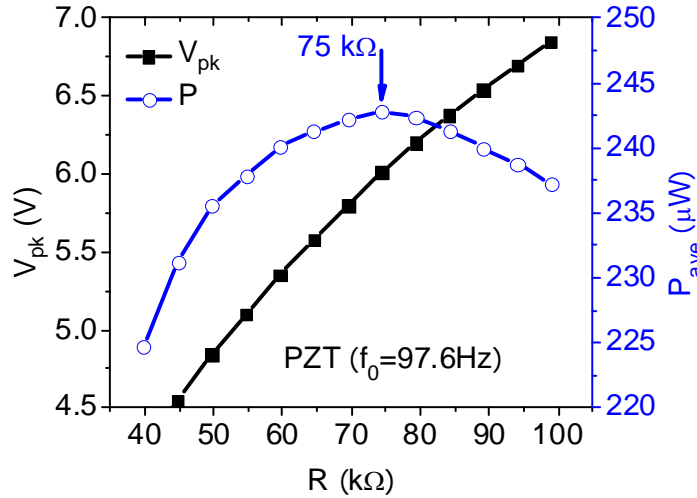
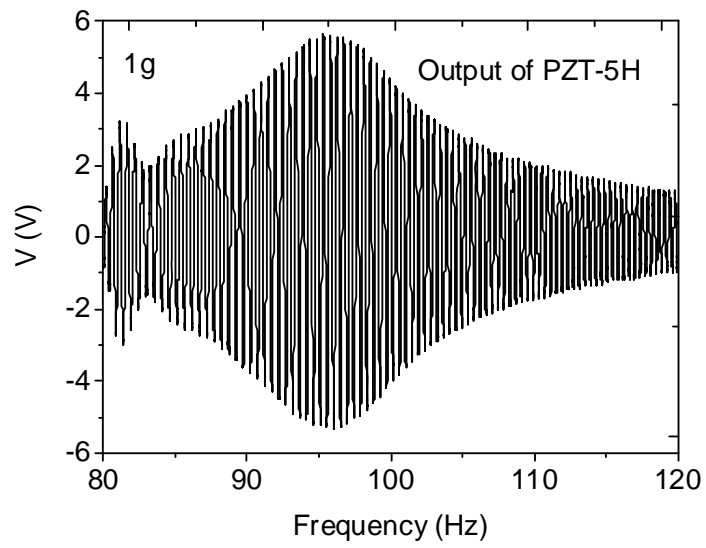
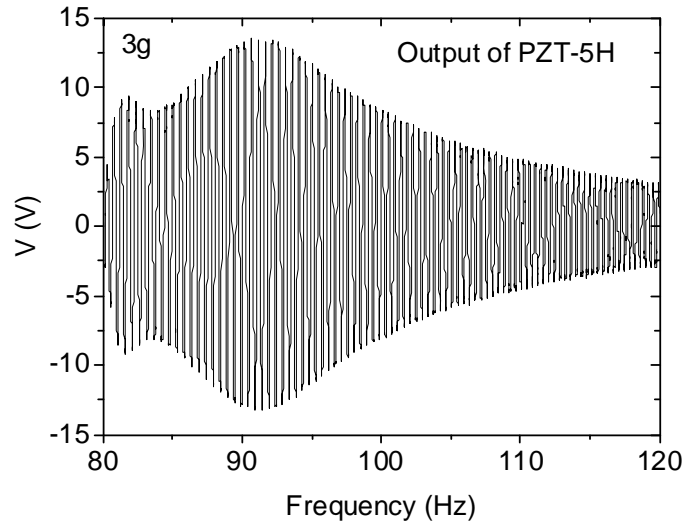


Figure 3- 18 Output peak voltage and power vs. the resistive load.

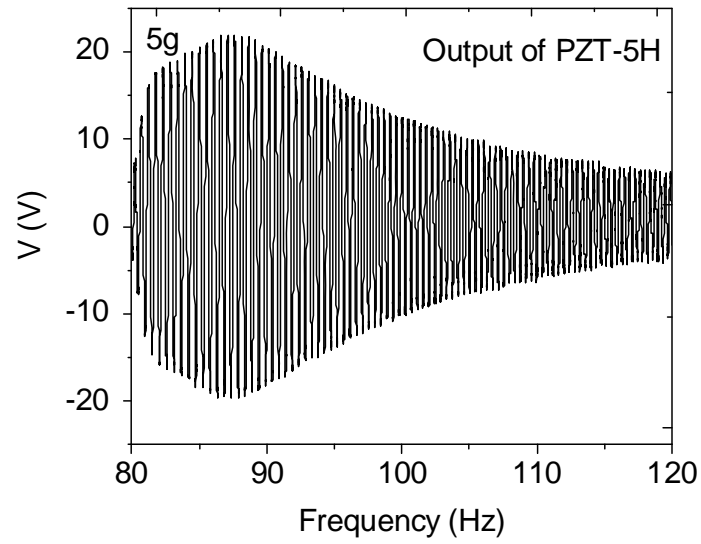
The AC outputs voltage at different acceleration amplitudes, 1g, 3g, and 5g and 75 Ω of resistive load are obtained by sweeping the vibration frequency from 80 to 120 Hz. The results are presented in Figure 3-19 (a), (b), and (c).



(a)



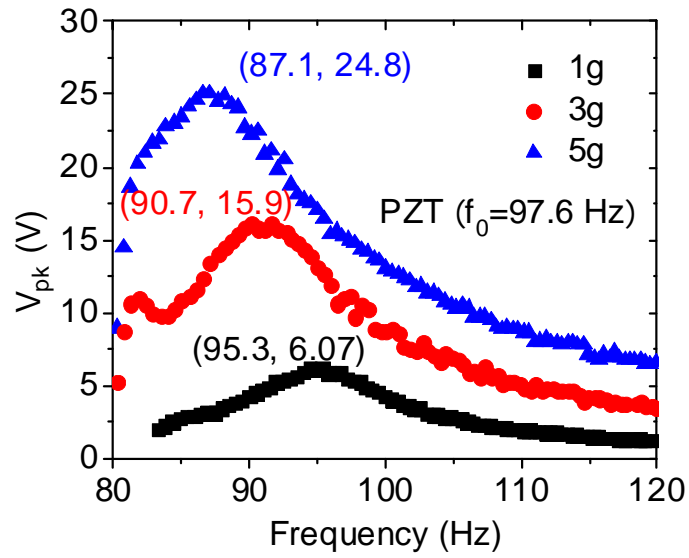
(b)



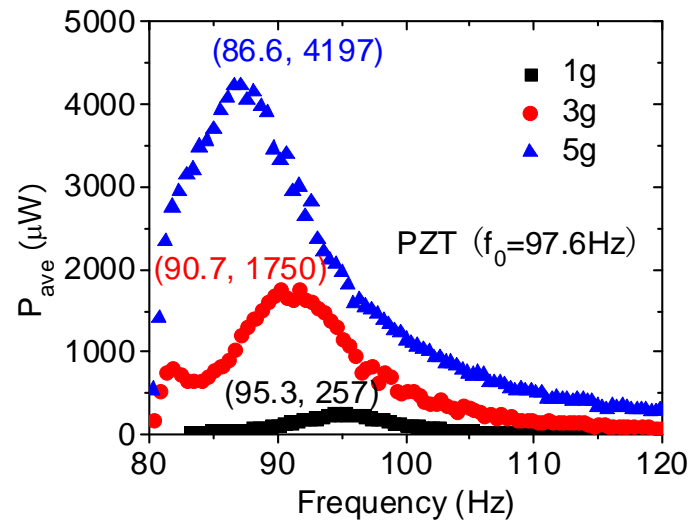
(c)

Figure 3- 19 AC voltage output at (a) 1g (b) 3g and (c) 5g acceleration amplitudes vs. vibration frequency.

The peak voltages obtained from the AC voltage output and the calculated peak power at different acceleration amplitudes versus frequency are summarized in Figure 3-20 (a) and (b).



(a)



(b)

Figure 3- 20 Peak voltages obtained from the AC voltage output and the average power vs. vibration frequency at different acceleration amplitudes.

The measured output voltages (V_{pk}) and the calculated power densities *via* $P=V^2/R$ divided by the effective volume of the device at 1g, 3g, and 5g accelerations are shown in Figure 3-21, and the power as a function of the vibration frequency reaches around 496 μW with 75 k Ω load at 1g vibration condition. Considering the volume of the cantilever, 0.06 cm^3 , the power density is about 8444 $\mu\text{W}/\text{cm}^3$, which is high enough to operate a microsensor system.

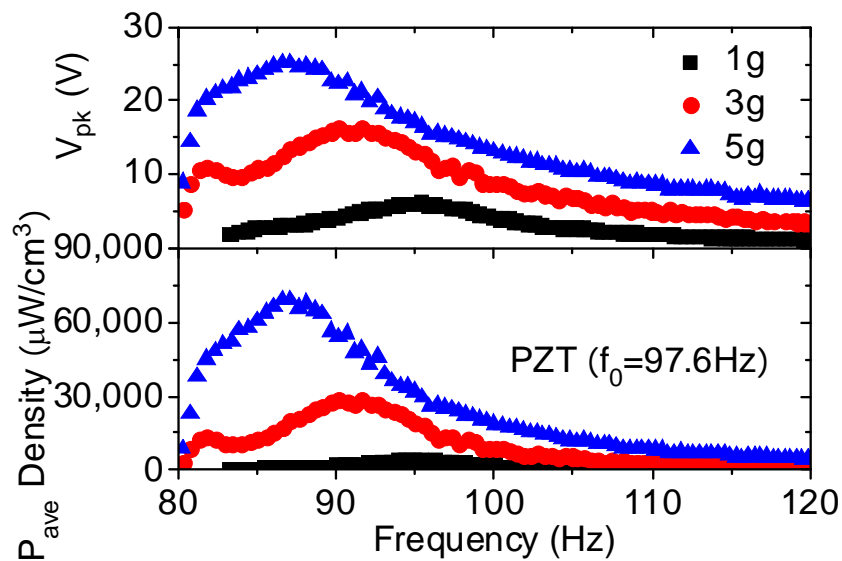


Figure 3- 21 Power density and voltage vs. vibration frequency of the PZT prototype.

The other phenomenon we can observe from Figure 3-21 is that peak frequency, where the maximum output power could be reached, shifted to lower frequency with the increasing vibration acceleration. This phenomenon is mainly attributed to the increasing

elastic compliance of PZT due to nonlinear effects under large stress [4, 10, 11]. This phenomenon can be clearly presented in Figure 3-22.

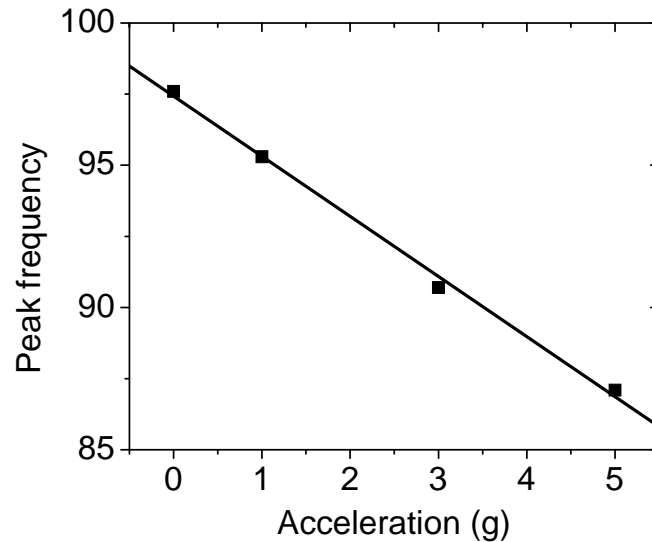
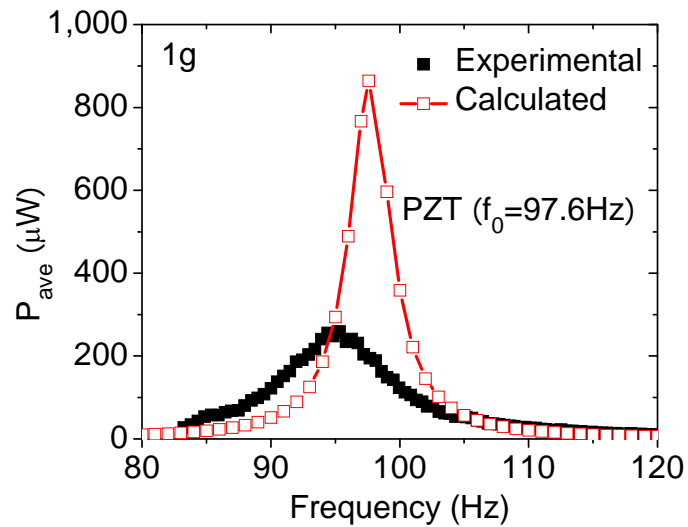


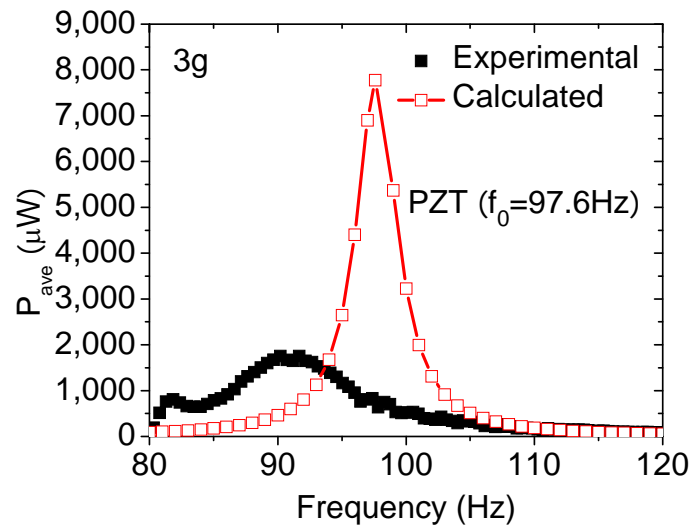
Figure 3- 22 Peak frequency of the bulk PZT power generator prototype vs. acceleration amplitude.

The experimental results were then compared with the simulation results got from the method discussed in 3.1.2.2, as shown in Figure 3-23. The simulation results are not so consistent with the experimental results in the optimal resistance, the peak vibration frequency, and the maximum output power. At 1g condition, the calculated optimal resistance is 4.12 k Ω , while the one attained by trial and error is 75 k Ω . This may also cause the difference of output power. Second, the theoretical peak vibration frequency should be 97.6 Hz, which is also the nature frequency of the cantilever, while the peak

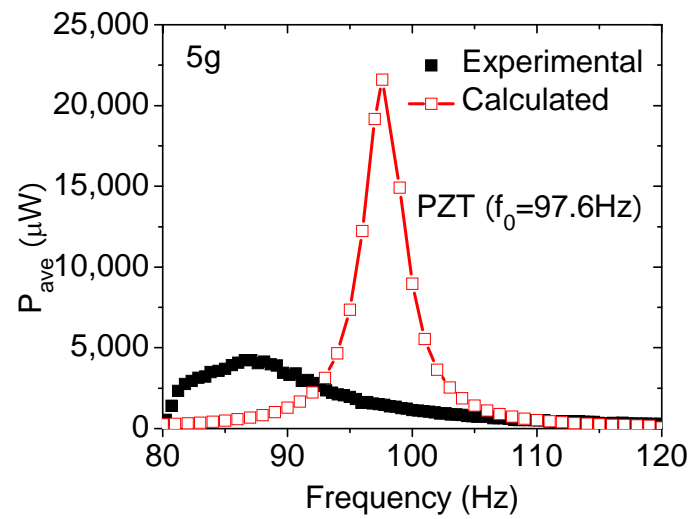
vibration frequency attained from the experimental data is 95.3 Hz. Third, the simulated maximum output power is 864 μW , while the measured one is 496 μW . With increasing of vibration, the difference between the experimental value and the simulated value begins to become larger and larger due to the nonlinear property of PZT. So the slope of experimental in Figure 3-24, which shows the relationship of output power versus the square of acceleration, is smaller than that of the calculated.



(a)



(b)



(c)

Figure 3- 23 Comparison of power output between experiment and calculation at different acceleration amplitudes.

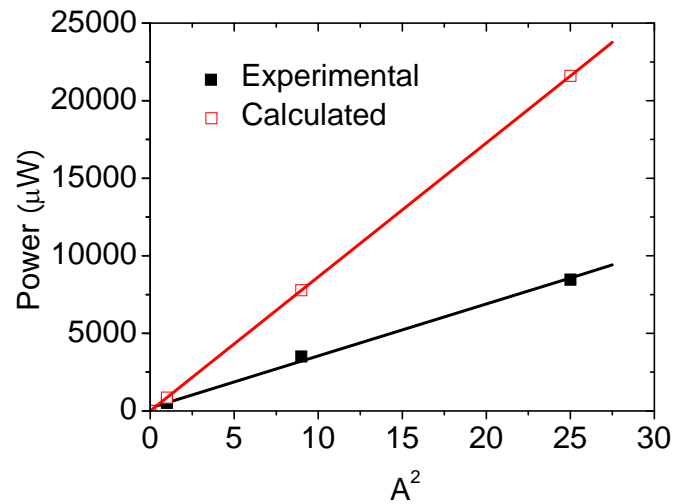


Figure 3- 24 Measured and calculated power vs. the square of acceleration amplitude.

3.4 Chapter summary

1. The new concept of converting environmental vibration energy into electricity by piezoelectric transducer was successful demonstrated.
2. The dimension of cantilever piezoelectric power generator prototype was optimized through balancing the power and fracture strength.
3. The optimized prototypes of piezoelectric cantilever generator ($f_r \sim 100$ Hz) were successfully fabricated using commercial a PZT-5H bender and evaluated.
4. The output power density of this power generator prototype even at 1g acceleration amplitude is high enough to supply energy to wireless sensor system.
5. The great potential of piezoelectric power generator was demonstrated.

References

- [1] www.piezo.com
- [2] S. Roundy, E. S. Leland, J. Baker, E. Carleton, E. Reilly, E. Lai, B. Otis, J. M. Rabaey, P. K. Wright, and V. Sundararajan, "Improving power output for vibration-based energy scavengers," *IEEE Pervasive Computing*, vol. 4, pp. 28-36, 2005.
- [3] R. K. Vierck, *Vibration Analysis*, 2nd edition ed. New York: Crowell Company, 1978.
- [4] Qing-Ming Wang, Qiming Zhang, Baomin Xu, Ruibin Liu, and L. Eric Cross, "Nonlinear piezoelectric behavior of ceramic bending mode actuators under strong electric fields," *Journal of Applied Physics*, vol. 86, pp. 3352-3360, 1999.
- [5] J. W. Yi, W. Y. Shih, and W.-H. Shih, "Effect of length, width, and mode on the mass detection sensitivity of piezoelectric unimorph cantilevers," *Journal of Applied Physics*, vol. 91, p. 1680, 2002.
- [6] R. D. Blevins, *Formulas for natural frequency and mode shape*. Malabar, Florida: Krieger Publishing Company, 2001.
- [7] X. Li, W. Y. Shih, I. A. Aksay, and W.-H. Shih, "Electromechanical behavior of PZT-brass unimorphs," *Journal of the American Ceramic Society*, vol. 82, pp. 1733-1740, 1999.
- [8] J. E. Sader, I. Larson, P. Mulvaney, and L. R. White, "Method for the calibration of atomic force microscope cantilevers," *Review of Scientific Instruments*, vol. 66, pp. 3789-3798, 1995.
- [9] S. Roundy, P. K. Wright, and J. Rabaey, "A study of low level vibrations as a power source for wireless sensor nodes," *Computer Communications*, vol. 26, pp. 1131-1144, 2003.
- [10] "IEEE standard on piezoelectricity," New York, 1987.
- [11] L. Q. Yao, J. G. Zhang, L. Lu, and M. O. Lai, "Nonlinear dynamic characteristics of piezoelectric bending actuators under strong applied electric field," *Journal of Microelectromechanical Systems*, vol. 13, pp. 645-652, 2004.

CHAPTER 4
DESIGN, INVESTIGATION AND COMPARISON OF BULK PROTOTYPES MADE
OF OTHER MATEIRALS

4.1 Introduction

In order to achieve higher vibration-to-electricity conversion, the cantilever structure with a proof mass was mainly focused since this structure can generate a larger strain and can be easily designed to oscillate at low frequencies whose ranges are typically between 60 and 200 Hz [1]. Although many sensor devices may be located under common environmental vibrations such as a building showing moderate values of vibration amplitudes ($< 9.8 \text{ m/s}^2$; 1 gravitational acceleration), they can be installed at the conditions of higher vibration amplitudes such as vehicles. Therefore, such devices will require both higher conversion efficiency and the vibration durability.

PZT ceramic is rather fragile, and it is safe to operate PZT power generator at lower acceleration condition, but not so secure to operate long-term at harsh conditions ($>10g$) due to the potential fatigue or high-g shock issues because PZT is readily fracture at high stress generated from large vibration amplitudes. This is also the general drawback of ceramic materials. The damage effect of PZT prototype on power output was therefore studied. The AC output voltages of a PZT power generator prototype before and after damage are shown in Figure 4-1. After damage, the output peak voltage

decreased to 25% of the value before damage. When the damage was so severe, the output was highly distorted.

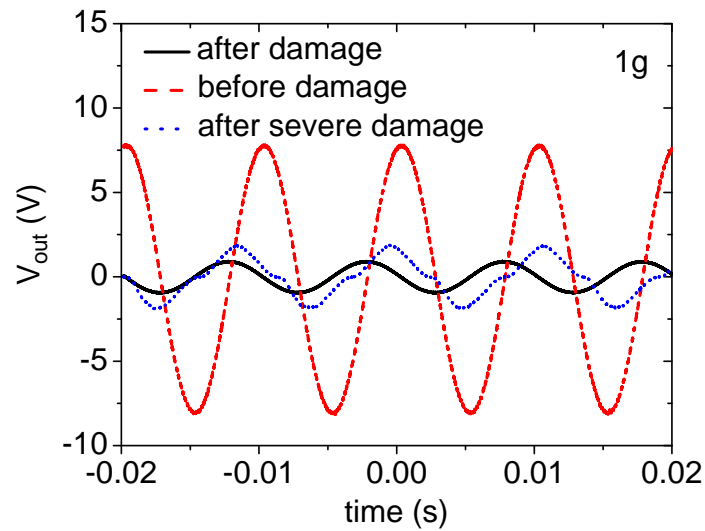


Figure 4- 1 Comparison of AC output before and after damage of PZT prototype.

One approach to avoid damaging is to increase the safety factor at the cost of losing the converting efficiency of energy, while, adopting other flexible material is another approach to improve the robustness of device at harsh vibration conditions.

4.2 Material selection and experimental procedure

4.2.1 Material selection

Since the fragility of the PZT ceramic, two more piezoelectric more flexible materials were investigated to improve the robustness of the cantilever power generator. They are PVDF (Polyvinylidene fluoride) and MFC (Macro Fiber Composite). Commercial benders are available for both materials, PVDF (Measurement Specialties, Inc., LDT0-028K/L) and MFC (Smart Material Corp., M8507 P2). The pictures of these three types of piezoelectric materials are presented in Figure 4-2.

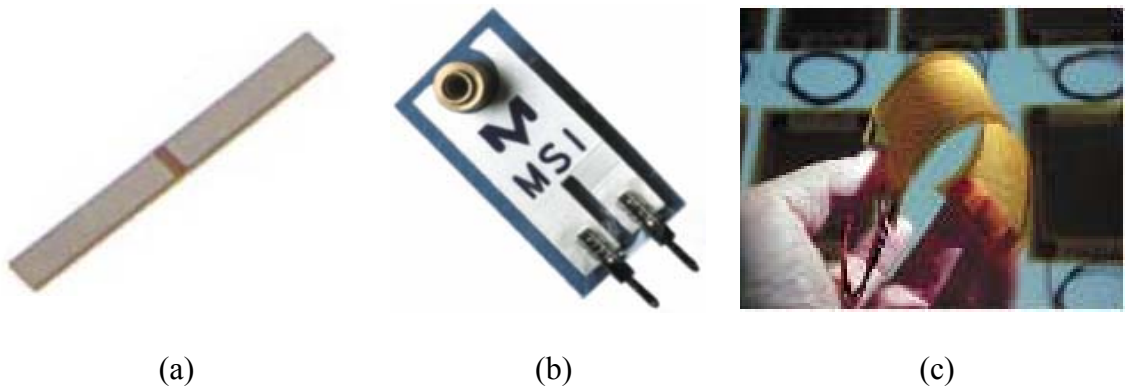


Figure 4- 2 Three types of piezoelectric transducers [2-4].

One main dimension was selected for each type of material. The qualitative characteristics of these three materials are summarized and compared in Table 4.1 for comparison. From the values in Table 4.1, PZT has the highest converting efficiency (coupling coefficient $k_{31} = 0.44$), the highest application temperature (230 °C), but the

lowest mechanical yield strength (~ 20 MPa); PVDF shows the highest flexibility (Young's modulus = 2~4), but the lowest converting efficiency ($k_{31} = 0.12$) and the application temperature (80 °C); MFC has the medium application temperature (180 °C) and the converting efficiency.

Table 4. 1 Characteristic comparison among three types of piezoelectric materials.

Properties	PZT	PVDF	MFC
Maximum temperature (°C)	230	80	180
Young's modulus (GPa)	62	2-4	16
Yield strength (MPa)	20	30	>30
d_{31} ($E^{-1}m/V$)	320	23	170
k_{31}	0.44	0.12	-
Dielectric constant	3800	12-13	-

The three types of piezoelectric materials such as PZT ceramic, PVDF polymer, and MFC composite were investigated and analyzed to determine the capability of harvesting energy under higher vibration amplitudes (≥ 1 g) without device failure. Dimensions of the PZT prototype were designed and fabricated by considering the resonant frequency, the output power density, and the maximum operating acceleration or

safety factor. To analyze and evaluate the performance of energy harvesting devices depending on types of piezoelectric materials, three criteria were applied: first, the same bimorph configuration with a 0.1mm thick of flexible brass center shim (as shown in Figure 3-3); second, the same volume of the piezoelectric materials (PZT or PVDF) as the PZT prototype, $\sim 0.02 \text{ cm}^3$; third, the similar resonant frequency ($\sim 100 \text{ Hz}$).

4.2.2 Prototype fabrication and evaluation

The dimensions of the piezoelectric benders and the final designs are listed in Table 4.2.

Table 4. 2 Finally designed dimensions of three types of power generators.

Dimensions	PZT	PVDF	MFC
Bender: length \times width \times height (mm^3)	25.00 \times 3.20 \times 0.38	10.94 \times 22.00 \times 0.354	15.80 \times 7.00 \times 0.50
Weight of proof mass (g)	0.501	3.512	2.740
Total prototype volume (cm^3)	0.0564	0.267	0.197

Figure 4-3 shows the picture of the finally fabricated prototypes.

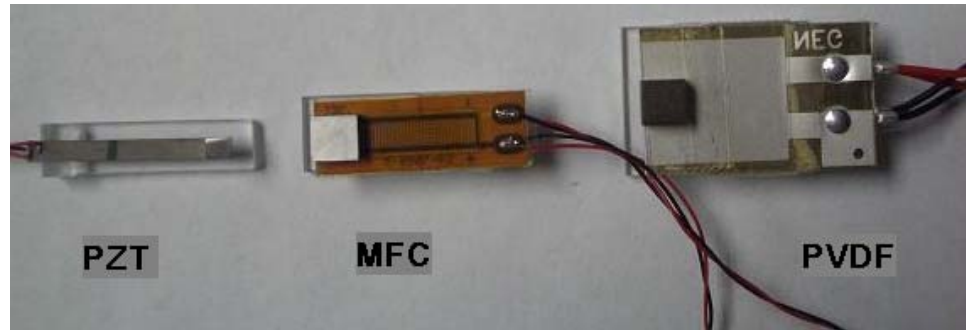


Figure 4- 3 Picture of fabricated prototypes using three types of piezoelectric materials.

The resonant frequency of a prototype was measured using an impedance analyzer (Agilent Technologies 4294A), and then the output signal was evaluated using the experimental setup as shown in Figure 3-15.

4.3 Results and discussion

Figure 4-4 shows the measured resonant frequencies of the three prototypes. The difference between the calculation and the measurement is within 5% for the PZT device, but larger than 5% for the MFC and the PVDF cantilevers due to the inaccurate Young's modulus and the complexity of the benders. For the PZT-based prototype, the phase angle changes sharply at the resonant frequency, while the changes for the PVDF- and the MFC-based prototypes are not so sharp and show more noise, especially for the PVDF prototype. These may be resulted from the different dielectric properties of the three materials. Lower charge can only be generated from PVDF and MFC. In addition, the different bending behaviors due to the rigidity of materials and the fixture situations

might be other reasons for the noise. These could also be factors influencing the output voltage and power by influencing the damping ratio.

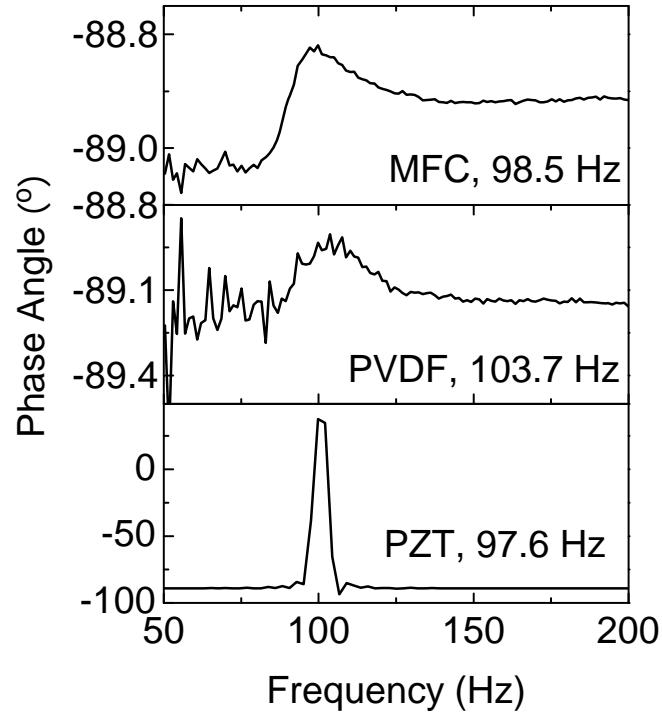
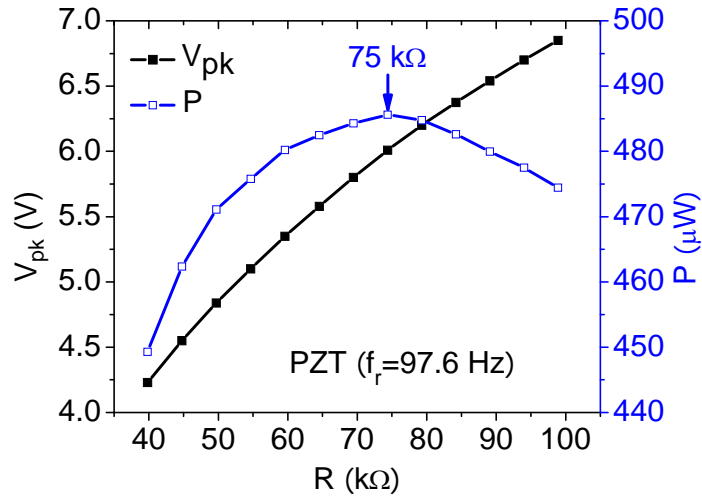


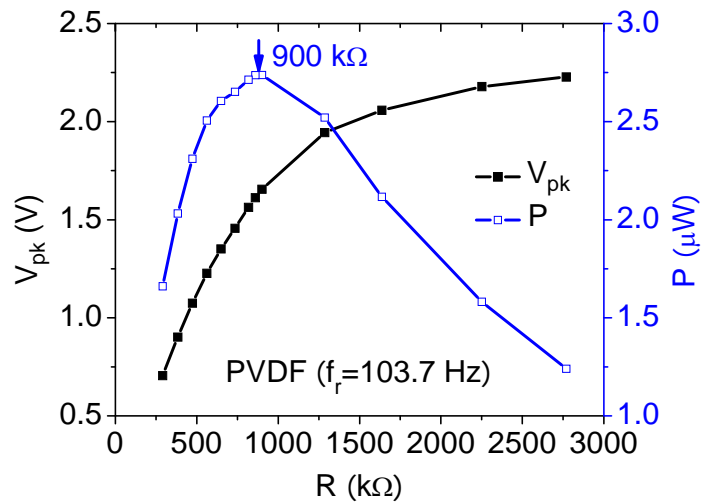
Figure 4- 4 Measured resonant frequencies of devices from three types of piezoelectric materials.

The output-peak voltages were first measured with varying load resistors at given vibration acceleration. And, the output peak powers were calculated using the measured peak voltages and the resistance loads. The relationships of the peak power and the peak voltage versus the resistive load of the three prototypes are shown in Figure 4-5 at 1 g acceleration condition. The optimal resistive loads where maximum power reached, of

these three prototypes at 1g acceleration amplitude were found to be 75 k Ω (PZT), 900 k Ω (PVDF), and 55 k Ω (MFC) as shown in Figure 4-5.



(a)



(b)

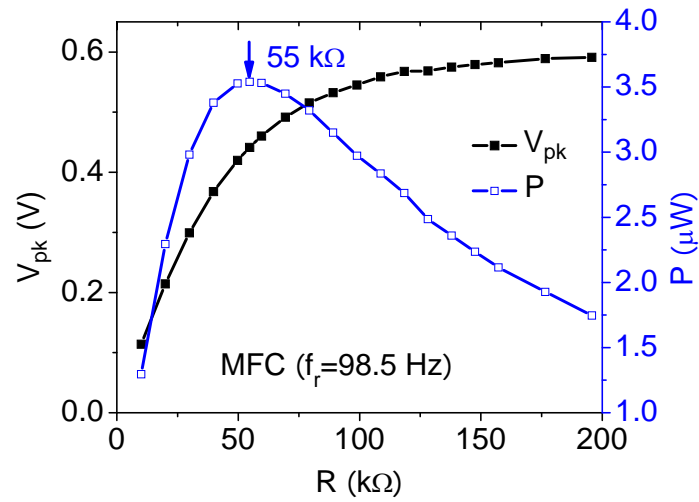
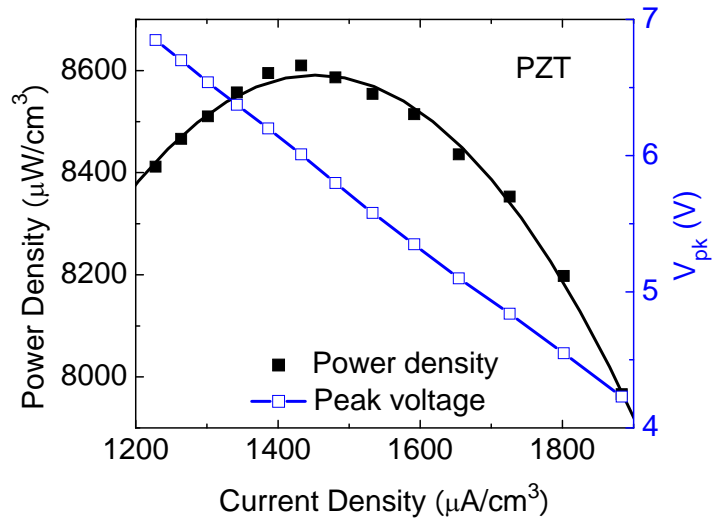
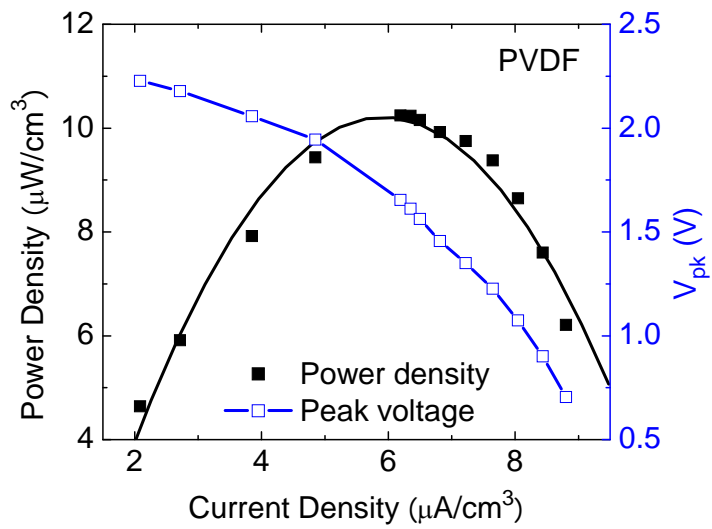


Figure 4- 5 Optimal resistive loads of three prototypes: (a) PZT, (b) PVDF, and (c) MFC.

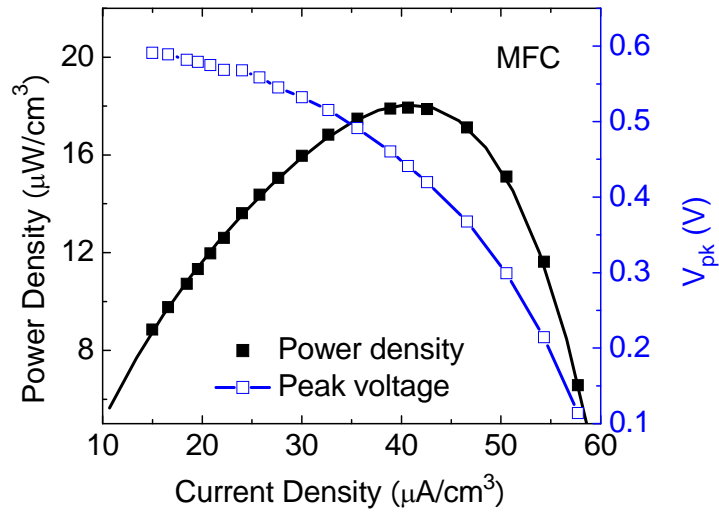
The power density was then calculated after considering the volume of devices. The generated current from the devices is also calculated by Ohm's Law to provide the guide of choosing power management electronics such as rectifier and dc-dc converter. The relationships of the peak power density and the voltage versus the current density of three prototypes are shown in Figure 4-6 at 1 g acceleration condition. As seen in Figure 4-6, the current generated at 1 g condition and with about 0.02 cm³ volume of piezoelectric materials were about 81, 1.8, and 8.1 μA for PZT-, PVDF-, and MFC-based devices, respectively. Low current values in PVDF and MFC-based devices can have the limit of scaling to realize miniaturization.



(a)



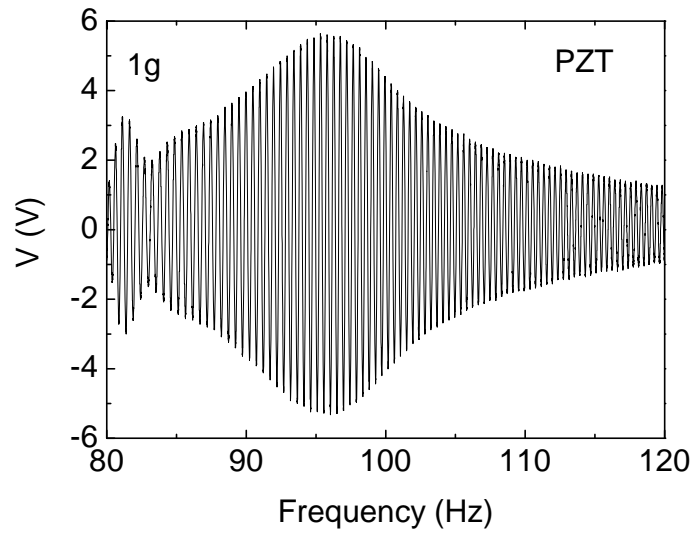
(b)



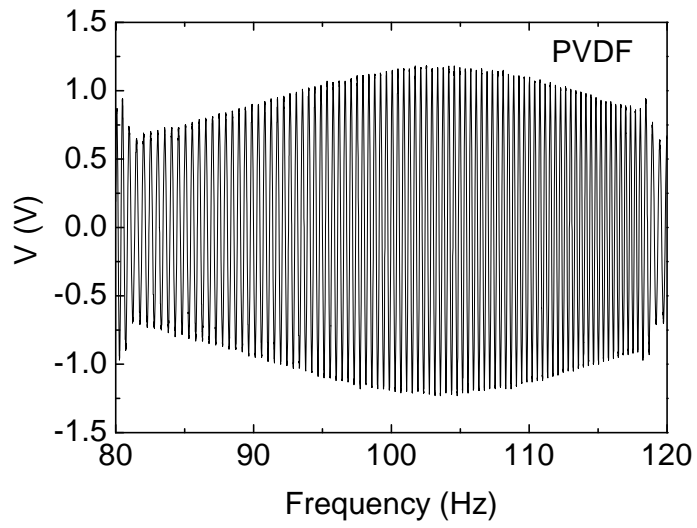
(c)

Figure 4- 6 Power density and voltage of (a) PZT, (b) PVDF, and (c) MFC vs. current density obtained using various external resistors.

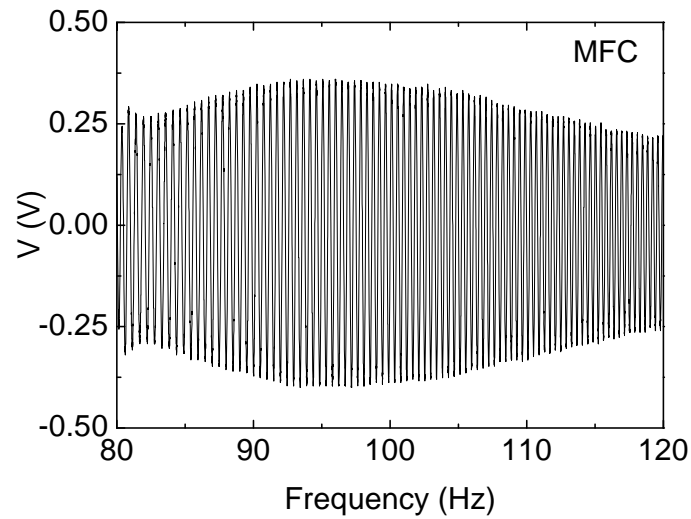
The AC outputs voltage of these three prototypes at different acceleration amplitudes, 1g, 3g, and 5g and individual optimal resistive load are obtained by sweeping the vibration frequency from 80 to 120 Hz. The results are presented in Figure 4-7.



(a)



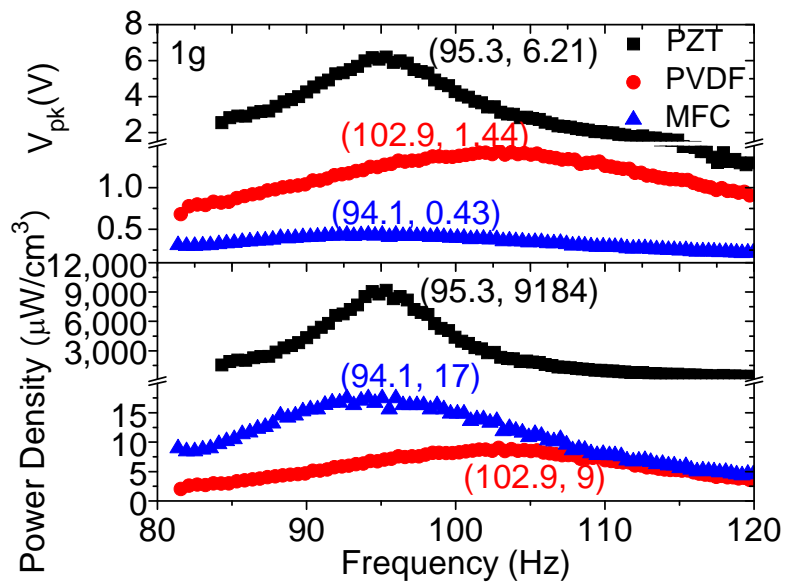
(b)



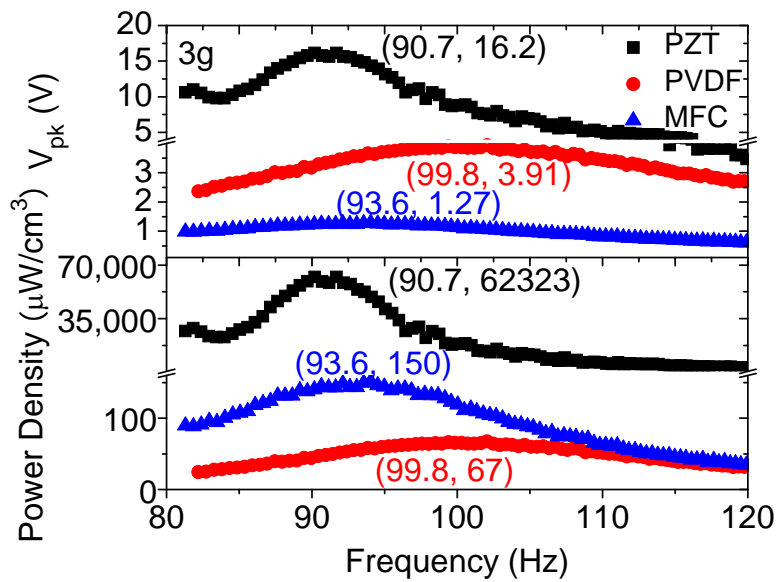
(c)

Figure 4- 7 Output voltage waveforms of three piezoelectric devices as a function of vibration frequency.

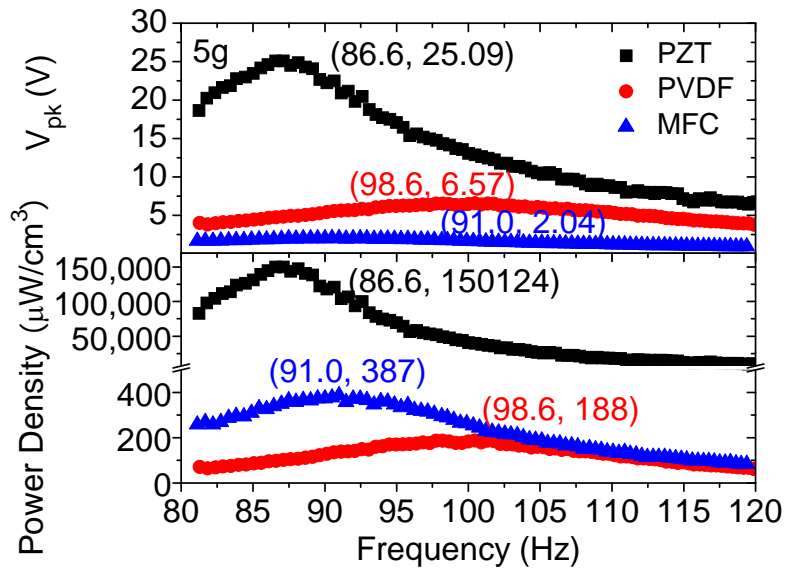
The output peak powers were calculated using the measured peak voltages and the resistive loads. The power densities were then calculated by considering the total volumes of prototypes. The peak voltages obtained from the AC voltage outputs and the calculated peak power density at different acceleration amplitudes, 1g, 3g, and 5g versus frequency are summarized in Figure 4-8.



(a)



(b)



(c)

Figure 4- 8 Power density and voltage of prototypes at (a) 1g, (b) 3g, and (c) 5g vs. vibration frequency.

The power densities of the MFC and the PVDF prototypes at 1g acceleration amplitude are 17 and 9 $\mu\text{W}/\text{cm}^3$ respectively, while the power density obtained from the PZT prototype is 9,184 $\mu\text{W}/\text{cm}^3$, which is approximately 540 and 1000 times larger than the output of the MFC and the PVDF prototypes. With increasing acceleration, the generated voltage increases exponentially. Therefore, higher vibration condition will allow the miniaturized devices from MFC and PVDF to achieve the minimum power density required supplying power to a microscale device based on reported values, that is,

above $300 \mu\text{W}/\text{cm}^3$ [5, 6]. These output data indicate that PZT could be the best candidate as a piezoelectric material for vibration energy harvesting in comparison with MFC and PVDF. Another factor for consideration is current through the piezoelectric devices. In general, the power in these devices is mainly due to higher voltage than current. Electronic components used in the energy harvesting devices such as DC voltage regulators or microsensors, however, operate with minimal current on the order of a few microamperes. As seen in Figure 4-6, the current generated at 1 g condition and with about 0.02 cm^3 volume of piezoelectric materials were about 81, 1.8, and $8.1 \mu\text{A}$ for PZT-, PVDF-, and MFC-based devices, respectively. Low current values in PVDF and MFC-based devices can have the limit of scaling to realize miniaturization.

Another observation from Figure 4-8 is that the maximum values of the power or the power density is reached when the ambient vibration frequency is matching with the measured resonant frequency of a prototype at 1g acceleration. Similarly to PZT prototype, when a prototype is under a high-g vibration condition, the resonant frequency where maximum output attained apparently shifts to lower values. For the high flexible PVDF prototype, the shift of the peak frequency is only 5.1 Hz. The shifts for the PZT- and the MFC-based prototypes are 11.0 Hz and 7.5 Hz, respectively. It has been observed that the resonant frequency shift decreases at a low-g vibration condition, *i.e.* the lower input magnitude of the vibration is applied to the same prototype. This phenomenon could be the combination results from the increasing effective mass and the elastic nonlinearity with high deflections. From Equation (3-9), we can see that the resonant frequency of a cantilever structure depends upon the Young's modulus of the material, the effective mass of the bender, the proof mass, and the dimensions of the cantilever

structure. This shifting should be considered during designing cantilever based power conversion devices for high-g vibration applications.

The potential fracture or damage of the piezoelectric materials under high-vibration conditions can limit the applications requiring severe vibrations such as vehicle conditions. To evaluate the robustness of a cantilever structure, the safety factor (S) was introduced and calculated by Equation (3-14). The maximum power density and correlated safety factor at 1g, 3g and 5g acceleration amplitudes of the three prototypes are summarized and compared in Table 4.3. The PVDF prototype shows the highest fracture strength, and the fracture strength of the MFC prototype is twice lower than that of the PVDF prototype, but the fracture strength of the PZT prototype is about one order of magnitude lower than that of the PVDF prototype, *i.e.* 12 vs. 266. These results mean that it is likely safe when operating the PVDF and the MFC prototypes above 100g, but the damage of the PZT prototype is highly probable when operating over 10g. Therefore, PVDF and MFC show the potentials at harsh vibration environments. The low output power of the PVDF- or the MFC-based prototype may be diminished at high-g conditions.

Table 4. 3 Characteristic comparison of three prototypes.

Characteristics		PZT	PVDF	MFC
Optimal resistance (k Ω)		75	900	55
Effective volume (cm ³)		0.0564	0.2672	0.1973
Resonant frequency (Hz)	0g	97.6	103.7	98.5
	1 g	95.3	102.9	94.1
	3 g	90.7	99.8	93.6
	5 g	86.6	98.6	91.0
Peak Voltage V_{pk} (V)	1 g	6.21	1.44	0.43
	3 g	16.20	3.91	1.27
	5 g	25.09	6.57	2.04
Peak current density with R_{Opt} (μ A/cm ³)	1 g	1468	6	40
	3 g	3830	16	117
	5 g	5931	27	188
Average power density at different acceleration (μ W/cm ³)	1 g	4558	4	9
	3 g	31,021	32	74
	5 g	74,410	90	192
Safety factor at different acceleration	1 g	12.0	266	113
	3 g	4.0	89	38
	5 g	2.4	53	23

Figure 4-9 shows the estimation of output voltage and power density at high-g condition for PVDF and MFC devices. This estimation was based on the data measured at 1g, 3g, 5g, 7g, and 10g. These data indicate that mechanical strength and harvester efficiency of PVDF and MFC devices are good enough to be used as power scavenger at harsh vibration environment. When compared with PVDF, MFC shows lower optimal resistance load of 55 k Ω versus 900 k Ω (PVDF). Thus the current generated by a MFC device is much higher than that by a PVDF device. In addition, the maximum working temperature of MFC is higher than that of PVDF.

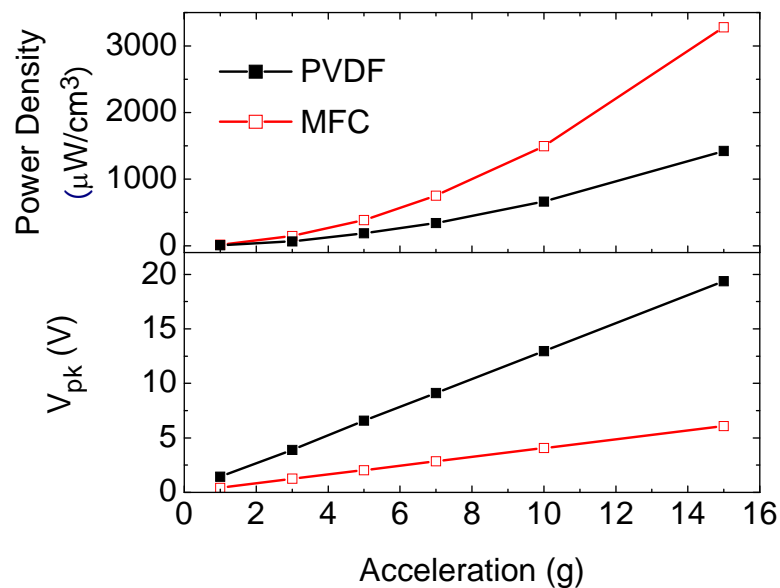


Figure 4- 9 Estimation on the output voltage and power density of PVDF and MFC prototypes at high-g vibration conditions.

4.4 Chapter summary

Cantilever power harvesting prototypes made of three types of piezoelectric materials such as PZT ceramic, MFC composite and PVDF polymer were designed and fabricated. Devices with the same volume of piezoelectric materials were evaluated by varying the load resistance, the ambient vibration frequency and amplitude, and the maximum fracture strength of each prototype was estimated from the proposed equations and verified. PZT-based device shows the highest power and current densities among three devices. The damage of a piezoelectric material determined by calculating fracture strength, however, can limit its applications into low-g vibration conditions unless further modification of design. For such harsh vibration conditions, MFC and PVDF show the potentials. However, the current generation in these devices is limited by the size of piezoelectric materials.

References

- [1] S. Roundy, P. K. Wright, and J. Rabaey, "A study of low level vibrations as a power source for wireless sensor nodes," *Computer Communications*, vol. 26, pp. 1131-1144, 2003.
- [2] <http://meas-spec.com>.
- [3] <http://www.smart-material.com/>.
- [4] <http://www.piezo.com>.
- [5] M. J. Ramsay and W. W. Clark, "Piezoelectric energy harvesting for bio MEMS applications," Newport Beach, CA, 2001, pp. 429-438.
- [6] H. W. Kim, A. Batra, S. Priya, K. Uchino, D. Markley, R. E. Newnham, and H. F. Hofmann, "Energy harvesting using a piezoelectric "cymbal" transducer in dynamic environment," *Japanese Journal of Applied Physics, Part 1: Regular Papers and Short Notes and Review Papers*, vol. 43, pp. 6178-6183, 2004.

CHAPTER 5
SAFETY FACTOR IMPROVEMENT FOR HIGH AMPLITUDE VIBRATION
APPLICATION

The attachment of a large proof mass to the free end tip of the cantilever has been used not only to lower the resonant frequency of a cantilever to match the exciting frequency (60~200 Hz) of many low amplitude vibration sources [1], but also to generate a large strain or power output. However, the extremely large stresses at the clamping area that result from sudden impacts or higher vibration amplitudes such as in mobile vehicles, aircraft, and machining tools make the structures vulnerable. This is one of the reasons why few people study ceramic piezoelectric cantilevers for both low frequency and high amplitude vibration applications. Although high mechanical strength or flexible piezoelectric materials can compensate this fragile disadvantage of piezoelectric ceramics, there is another potential solution proposed in this chapter. A dense medium can protect the fragile structure from fracture by adding damping, although the dynamic behaviors of the cantilever will be strongly influenced by the fluid physical properties.

In this chapter, the behavior of vibrating a fragile power generator in a viscous fluid will be investigated. The changes in resonant frequency, Q-factor, damping ratio, and power output of a bimorph piezoelectric cantilever prototype, as well as the relationship of power output versus the vibration acceleration were investigated. The

broadened application frequency spectrum and the increased maximum operational acceleration demonstrate the potential of the bimorph piezoelectric cantilever operating in a viscous fluid for high amplitude vibration applications.

5.1 Mechanical behavior of a cantilever in a fluid

The resonant frequency, one of the key parameters, of the cantilever with a nonpoint proof mass attached to the free end tip can be estimated by Equation (3-9).

When the cantilever is submerged in a viscous fluid, the fluid will resist its vibration due to inertial and damping forces distributed over the surface of the cantilever [2-4]. The inertial force is proportional to the acceleration of cantilever vibration with the proportionality constant, m_a , the added mass due to the fluid. The damping force is proportional to the vibration velocity. The added mass mainly serves to decrease the resonant frequency, while viscous damping contributes to the Q-factor drop. A low Q-factor indicates high energy dissipation. The Q-factor of a power generator can be calculated from its resonant response curve by $Q = f_0 / \Delta f$, where f_0 is the peak frequency, Δf is the band width at the half peak amplitude.

The resonant frequency of the cantilever is therefore decreased by the added mass, and can be calculated by rewriting Equation (3-9) as [5]:

$$f_n = \frac{v_n^2}{2\pi} \sqrt{\frac{0.236E_0 w}{(l - l_m / 2)^3 (m_e + m_{ae} + \Delta m)}} \quad (5-1)$$

where m_{ae} is the effective added mass by the viscous fluid at the middle of the proof mass, and can be calculated from the added mass, $m_{ae} = 0.236m_a(l - l_m / 2) / l + m_a l_m / (2l)$.

Based on strip theory, the added mass can be roughly estimated by the density of the fluid and the geometry of the cantilever, $m_a = (\pi/4)\rho w_p^2 l$ when a slender (large aspect ratio) cantilever is submerged into a theoretically infinite fluid bath [6].

5.2 Experimental setup and measurement

In this section, the vibration behaviors of a piezoelectric cantilever fabricated using a bimorph bender (T215-H4-103Y, Piezo Systems, Inc., Cambridge, MA) and a tungsten proof mass in both air and Si oil environments were investigated. The schematic and notations of the device can be found in Figure 3-3. Figure 5-1 presents the picture of the device and the schematic diagram of the device submerged in Si oil. The dimensions of the cantilever beam and the proof mass are respectively $l \times w_p \times (2t_p + t_s) = 25.2 \times 3.2 \times (2 \times 0.134 + 0.123) \text{ mm}^3$ where l and w_p are the total length and the width of the cantilever beam, t_p and t_s respectively the thicknesses of the piezoelectric material and the center shim brass, and $l_m \times w_m \times h_m = 2.73 \times 2.80 \times 2.70 \text{ mm}^3$ where l_m , w_m , and h_m the length, width, and height of the proof mass.

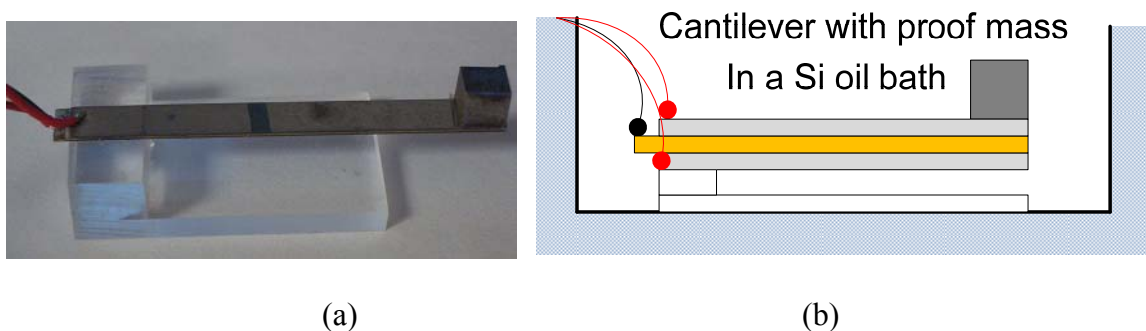


Figure 5- 1 (a) Picture of the device and (b) schematic diagram of the device submerged in Si oil (not to scale).

5.3 Results and discussion

The resonance spectra of the cantilever in air and in Si oil were measured by an impedance analyzer (Agilent 4294A), and are presented in Figure 4-2. The peak value of the phase angle decreased from 106.4 Hz in air to 86.4 Hz in Si oil. In air, the theoretical value calculated from Equation (3-9) is 108.5 Hz resulting in a difference of 1.9%. In Si oil however, a difference of 14.8% was observed with the resonant frequency calculated from Equation (5-1), $f_{fluid} = 101.4$ Hz. The large discrepancy in Si oil is mainly attributed to the heavy proof mass, which appears to have weakened the effect of the inertial loading caused by the added fluid mass upon the resonant frequency of the device since estimates given by Equation (5-1) work well for a cantilever without a proof mass submerged in a fluid.

An alternate approach to estimating the resonant frequency in liquid is based upon [6]:

$$f_{fluid} = \frac{1}{\left(1 + \frac{m_a}{m_b}\right)^{1/2}} f_{vacuum} \quad (5-2)$$

where m_b is the mass of a cantilever beam without a proof mass, f_{vacuum} the resonant frequency of the cantilever in vacuum, and here we substitute the resonant frequency in air, f_{air} , for f_{vacuum} because of negligible difference.

Initially neglecting the proof mass and only considering the loading effect of the fluid on the cantilever beam, we obtain from Equation (5-2) $f_{fluid} = 0.7538 \times f_{air} = 0.7538 \times 108.5 = 81.8$ Hz, and the error has been decreased to 5.6%. By considering the buoyancy effects on the whole cantilever structure, m_{ae} is reduced from 0.2559 to 0.2256

gram, Δm is reduced from 0.3983 to 0.3785 gram, and the f_{air} is increased to 111.94 Hz. We, therefore, obtained $f_{fluid} = 0.7538 \times 111.94 = 84.4$ Hz. The difference from experimental value has been reduced to 2.4%.

The Q-factor calculated from Figure 5-2 dropped from 20.30 to 8.65 when submerged in Si oil. The decreasing in the amplitude and the broadening in the full wave at half maximum (FWHM) are due to the added viscous damping by the fluid [4]. Broad bandwidth is favorable in energy harvesting application because a small deviation in the exciting frequency from the resonant frequency of the device will not cause such a large decrease in power output.

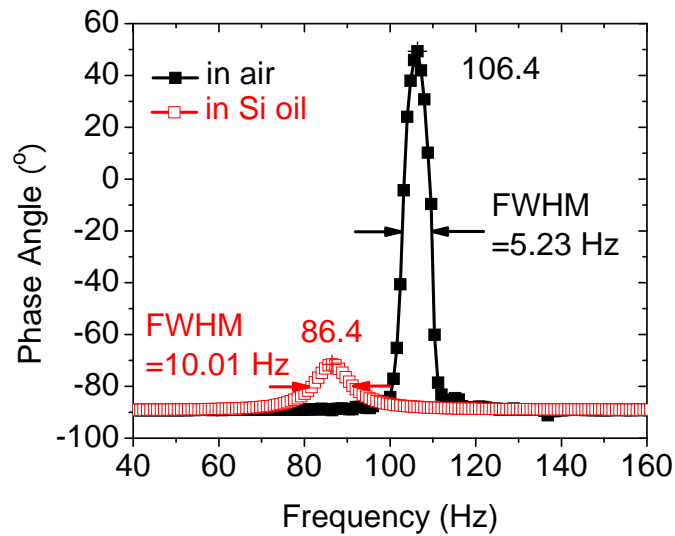


Figure 5- 2 Measured resonant frequency of cantilever in air and in Si oil.

Besides the resonant frequency of this device, the damping ratio (ζ) was also calculated at different accelerations. For a damped harmonic oscillator, the mass m , natural angular frequency ω_0 , viscous damping coefficient c , and the damping ratio ζ (defined as the ratio between the damping coefficient c and the critical damping coefficient c_c) are related by $c = 2m\zeta\omega_0$ [1]. A large damping ratio indicates low power conversion efficiency and increased energy loss. The AC outputs of the PZT cantilever were recorded separately immediately after stopping the exciting vibration. The damping ratio can be calculated by [1]:

$$\zeta = \frac{1}{2\pi n} \ln(x_1 / x_2) \quad (5-3)$$

where x_1 is the amplitude at one point in time and x_2 is a later amplitude measured after n periods of the sinusoidal response. For each acceleration evaluated, ten segments of the damped waveforms were randomly selected to obtain the amplitudes to be used in calculating the average damping ratios and the results shown in Figure 9. The ratio increases with the acceleration due to nonlinearity of PZT under large stress [7].

The results of the damping ratio for different accelerations and different mediums were measured and calculated are presented in Figure 5-3. The values in Si oil are much larger than those in air because of increased damping by the viscous medium. In both mediums, the damping ratio increases with acceleration due to the nonlinearity of PZT under large strain [7]. However, the slope in air is larger than that in Si oil because the displacement of the cantilever tip and the strain generated in the PZT beam are increasing faster with acceleration in air.

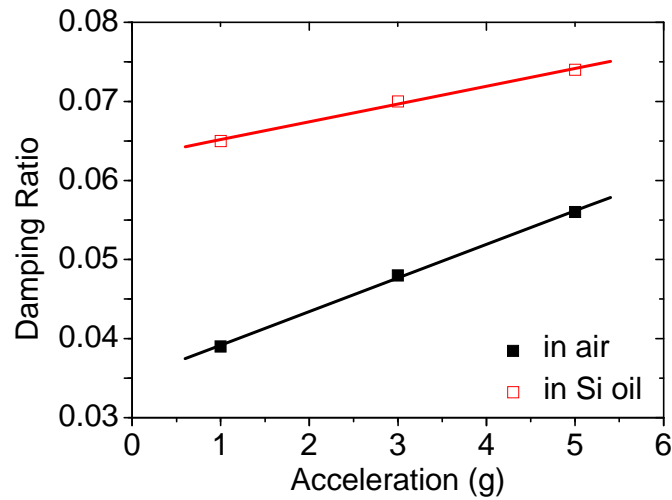


Figure 5- 3 Damping ratio in air and Si oil vs. the exciting vibration acceleration.

Figure 5-4 presents the optimal power output, the maximum power obtained by changing the resistive load, in air and in Si oil at different acceleration amplitudes versus vibration frequency. A summary of the comparison between a cantilever operating in air and Si oil is given in Table 5.1. Data in air at accelerations over 7g were not available because the device experiences a dramatic power decrease due to crack formations in the ceramic PZT in the device. By utilizing Si oil as a damping medium, the applicable acceleration in Si oil becomes about 10 times higher than that in air, and the applicable frequency bandwidth in Si oil is over twice as wide as that in air when the power output levels are similar.

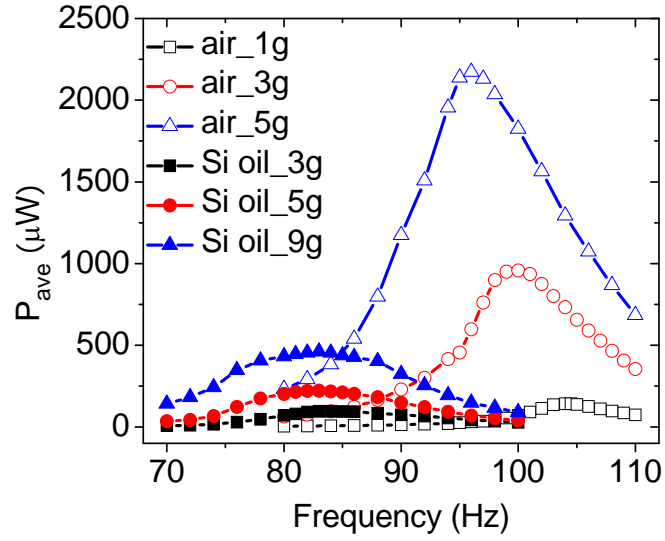


Figure 5- 4 Power output in air and Si oil vs. the exciting vibration frequency.

Table 5. 1 Comparison between different accelerations and mediums.

Acceleration (g)		0	1	3	5	7	9
FWHM (Hz)	in air	5.23	8.83	10.62	15.27	-	-
	in Si oil	10.01	11.01	18.01	21.80	24.57	27.46
f_r (Hz)	in air	106.4	104.0	100.0	96.0	-	-
	in Si oil	86.4	85.0	83.5	83.0	83.0	83.0
P_{max} (μ W)	in air	-	143	958	2174	-	-
	in Si oil	-	20	97	222	352	462

5.4 Chapter summary

In conclusion, a piezoelectric energy harvester operating in a viscous fluid for high amplitude vibration applications was proposed. For this application condition, two advantages are presented: larger operational bandwidth and higher operational vibration acceleration limit. The resonant frequencies of a bimorph cantilever prototype with a nonpoint proof mass were modeled both in air and in fluid. Experimental results showed that the resonant frequency in air matched well with the model, but in Si oil the measured resonant frequency was lower than the predicted one based on the first model because of the underestimated liquid loading effects due to the large proof mass, however the second method based on experiential method matched the experimental results well.

References

- [1] S. Roundy, P. K. Wright, and J. Rabaey, "A study of low level vibrations as a power source for wireless sensor nodes," *Computer Communications*, vol. 26, pp. 1131-1144, 2003.
- [2] S. Kirstein, M. Mertesdorf, and M. Schonhoff, "The influence of a viscous fluid on the vibration dynamics of scanning near-field optical microscopy fiber probes and atomic force microscopy cantilevers," *Journal of Applied Physics*, vol. 84, pp. 1782-1790, 1998.
- [3] T. Naik, E. K. Longmire, and S. C. Mantell, "Dynamic response of a cantilever in liquid near a solid wall," *Sensors and Actuators A: Physical*, vol. 102, pp. 240-254, 2003.
- [4] C. Vancura, J. Lichtenberg, A. Hierlemann, and F. Josse, "Characterization of magnetically actuated resonant cantilevers in viscous fluids," *Applied Physics Letters*, vol. 87, p. 162510, 2005.
- [5] G. A. Campbell and R. Mutharasan, "Detection of pathogen Escherichia coli O157:H7 using self-excited PZT-glass microcantilevers," *Biosensors and Bioelectronics*, vol. 21, pp. 462-473, 2005.
- [6] R. D. Blevins, *Formulas for natural frequency and mode shape*. Malabar, Florida: Krieger Publishing Company, 2001.
- [7] L. Q. Yao, J. G. Zhang, L. Lu, and M. O. Lai, "Nonlinear dynamic characteristics of piezoelectric bending actuators under strong applied electric field," *Journal of Microelectromechanical Systems*, vol. 13, pp. 645-652, 2004.

CHAPTER 6

DESIGN AND DEMONSTRATION OF MEMS-SCALE POWER GENERATOR PROTOTYPES BASED ON A SI WAFER

6.1 Substrate effects on sol-gel PZT thin film

There are several available methods to grow PZT thin film, such as chemical solution deposition (CSD) which includes sol-gel [1-5] and metal-organic decomposition [6-9], RF/DC magnetron sputtering [10-15], metal-organic chemical vapor deposition (MOCVD) [16-19], ion beam sputtering [20-22], and pulsed laser deposition (PLD) [23, 24]. Among them, sol-gel is the most popular one mainly because of the low cost. Table 6.1 summarizes the characteristics of these methods.

For power generation application, the formation of perovskite structure is very important in the PZT thin film fabrication. Nucleation and growth of perovskite requires a precise stoichiometry, or competing phases with fluorite and pyrochlore structures nucleate. At low temperature, fluorite phase caused by O₂ deficiency; at high temperature, pyrochlore phase caused by heavy Pb loss due to high diffusivity and volatility of Pb / PbO when temp is above 500°C. Activation energy for nucleation of perovskite is larger than for its growth (4.4 vs. 1.1 eV per unit cell), and it increases with Zr content.

Table 6. 1 Comparison of PZT thin film fabrication methods.

Method	Pros and Cons
Chemical Solution Deposition (CSD): sol-gel, metal-organic decomposition	Deposit amorphous thin films at low substrate temperature and followed by post-annealing; low cost.
RF/DC Magnetron Sputtering	Deposit amorphous thin films at low substrate temperature and followed by post-annealing or deposit at high substrate temperature with in-situ crystallization.
Metal-organic chemical vapor deposition (MOCVD)	Deposit at high substrate temperature with in-situ crystallization; Suited for integrated circuit (IC) production.
Ion beam sputtering	Deposit at high substrate temperature with in-situ crystallization.
Pulsed laser deposition (PLD)	Deposit at high substrate temperature with in-situ crystallization.

High-quality PZT films cannot be grown directly on silicon, and buffer layers are needed to prevent interdiffusion and oxidation reactions. For most applications, the PZT film has to be grown on an electrode, such as metal Pt, and metal oxide RuO₂, SrRuO₃, and (La,Sr)CoO₃. Adhesion layers used at the interface between SiO₂ or Si₃N₄ and

bottom electrode. Proper adhesion layer can significantly reduce the PZT film stress, and affect PZT film properties. Possible adhesion layer materials: TiN, TiO₂, Ti, Ta, Cr, ZrO₂, Zr, Ru, etc.

Besides the perovskite structure, the other important parameter affecting the property of PZT thin film is the residual stress. In thin film studies, only biaxial or in plan stress will be considered. Compressive stress increases the switching polarization and coercive field; tensile stress decreases the switching polarization and coercive field. Tensile stress stabilizes domains oriented parallel to the plane of the layers; compressive stress favors polarization alignment perpendicular to the layer. The stretch or contract of PZT thin film lattice constant to match the lattice constant of substrate generates misfit strain, and lead to lattice distortion, dislocation formation, ferroelastic domain wall generation and motion. The elastic properties of PZT thin film can also be affected by the film composition and domain mobility.

By formation process, there are two types of residual stress: intrinsic and extrinsic stresses. Intrinsic stress is generated in film deposition, and caused by film microstructure and lattice defects. Compressive stress is generally generated by ion bombardment. Extrinsic stress is caused by changes in volume or lattice parameter in film, densification, crystallization, and phase transformation during heat treatment.

However, the most important residual stress in PZT thin film at room temperature is the thermal stress. It is caused by different thermal expansion coefficients of the substrate and PZT. Low Zr content exhibits compressive stress, and high Zr exhibits tension stress because the thermal expansion coefficient of film decreases with increasing Zr / (Ti+Zr) ratio and the sign changes at about 0.25.

Table 6. 2 Dependence of the residual stress of PZT thin film on the substrate conditions.

Substrate	Deposition technology	Film thickness (nm)	Stress (Mpa)
Pt(150 nm)/Ti(15 nm)/SiO ₂ (400 nm)/Si	CSD	400	1200
Pt(70 nm)/Ti(4 nm)/SiO ₂ /Si	CSD , annealed 3-layer	220	113
(100)Si	CSD , single layer CSD, >5 layers	82 -	200 -20
Pt(100 nm)/Ti(50 nm)/SiO ₂ (20 nm)/Si	CSD, 3 layers CSD, 10 layers	104 405	228 515
Pt(170 nm)/Ta(20 nm)/SiO ₂ (700 nm)/Si ₂	CSD	500	175
Sapphire	Electron beam evaporation and furnace annealing	300	-30
Pt(100 nm)/Ti(50 nm)/SiO ₂ (500 nm)/SiN _x (100 nm)-membrane	Reactive sputtering, rapid temperature annealing	1000-2000	380
(111)Pt(40 nm)/TiO ₂ (100 nm)/SiO ₂ (500 nm)/Si	Reactive sputtering and furnace annealing	750-1000	-200
(111)Pt(40 nm)/TiO ₂ (100 nm)/SiO ₂ (500 nm)/Si	In-situ crystallization during reactive sputtering	750-1000	80-110
Pt(60 nm)/ZrO ₂ (20 nm)/SiO ₂ (500 nm)/Si	In-situ crystallization during reactive sputtering	700-1200	-170-300
(111)Pt(50 nm)/TiO ₂ (50 nm)/Si ₃ N ₄ (500 nm)/SiO ₂ (200 nm)/Si	In-situ crystallization during reactive sputtering	1000	850±200
(100)Pt(100 nm)/(100)MgO	MOCVD	-	600-1600

The substrates and deposition techniques therefore have a significant influence on the properties of PZT thin films. Table 6.2 lists the dependence of the residual stress of PZT thin film on the substrate and deposition techniques [25].

From literature survey we found that PZT/Pt/Ti/SiO₂/Si is the most widely applied sequence [2, 3, 11-13, 26-32]. Oxygen migrates along the grain boundaries through the platinum film and reacts with the Ti. Ti diffuses and reacts with oxygen and serves as nucleation centers for PZT and facilitates the formation of nucleation sites for perovskite PZT films and improved the adhesion between Pt and SiO₂ [27]. Two ways to improve the Ti out-diffusion: thicker Ti and thinner Pt, but (100) orientation decreases, and also decreases with the preparation temperature of the Pt/Ti layers [12]; thermal treatment in O₂ causes rapid oxidation of Ti and migration of Ti into Pt layer [28].

However, excess Ti diffusion not only gives rise to hillocks leading to short circuit between top and bottom electrodes but decreases the total capacitance of PZT due to the low dielectric constant interfacial layer as shown in Figure 6-1. Hillocks are generated by the volume expansion of the Pt layer due to oxidation of diffused Ti [26]. Hillocks relieve the compressive stress of the Pt films, and the size of hillocks but the density leads to electrical short of the PZT capacitors.

**Excess Ti
diffusion
generates
hillocks**

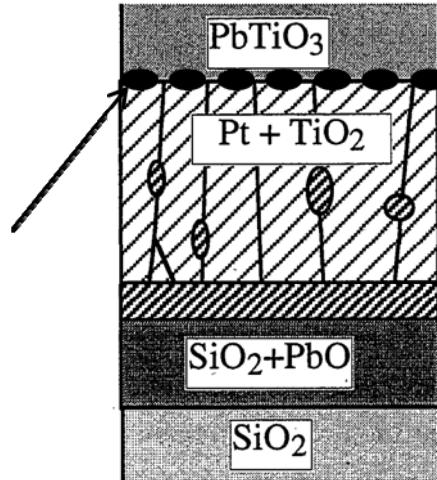


Figure 6- 1 Hillocks generation between bottom and top electrode (Pt) layers [27].

There are several ways to control the Ti diffusion. Kim proposed in 1997 that denser Pt film can control Ti diffusion [13]. As the deposition temperature of Pt increases and the deposition rate decreases, the film becomes dense so that Ti out-diffusion and film deformation are suppressed. Screenivas in 1994 [28] and Nam in 2000 [26] investigated the influence of Ti/Ti thickness ratio on the Ti diffusion activity. Besides, pre-annealing Pt/Ti in Ar atmosphere and decreasing O_2 partial pressure during oxygen annealing will also control the Ti diffusion.

In this study, a multi-layer MEMS-scale piezoelectric cantilever power harvesting device is proposed based on literature survey, as shown in Figure 6-2.

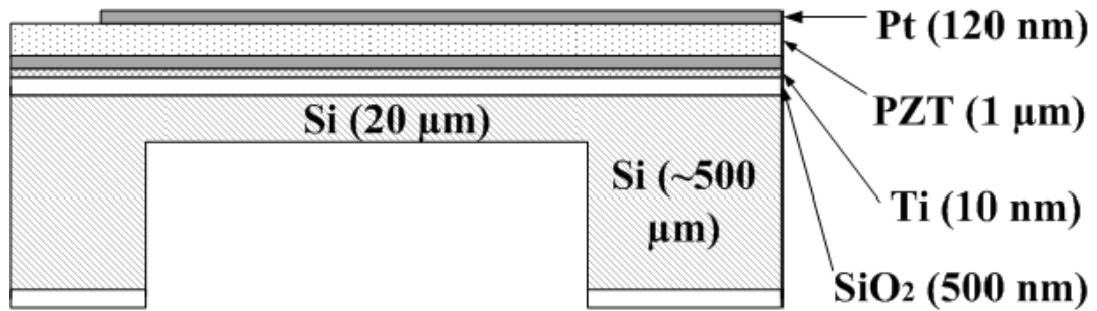


Figure 6- 2 Schematic diagram of the side view of a MEMS piezoelectric power harvesting device.

PZT is deposited by one of the Chemical Solution Deposition (CSD) methods, sol-gel. Although post annealing is required for this amorphous sol-gel PZT thin film and the fabrication process is complex, the cost of this method is very low. Buffer layer Ti is used to grow high-quality PZT films on silicon wafer to prevent interdiffusion and oxidation reactions. For this energy harvesting application, the PZT thin film has to be grown on an electrode. Platinum is used as the top and bottom electrodes because of its high conductivity, high melting point, and high stability in air at high temperature. Silicon dioxide was used to compensate the internal stress. An adhesion Ti layer is used at the interface between SiO₂ and bottom electrode because a proper adhesion layer can significantly improve the adhesion, reduce the PZT film stress, and affect PZT film properties. Pt/PZT/Pt/Ti/SiO₂/Si sequence is applied to MEMS-scale piezoelectric cantilever power harvesting device, as shown in Figure 6-2. Silicon is used as the proof mass, and the supporting layer to improve the mechanical strength of the beam.

6.2 Device design and fabrication

6.2.1 Device design

At the beginning, KOH wet etch was planned to use to release the cantilever structure because of the low cost. But it was finally replaced by the isotropic ICP RIE dry etching due to the complexity of the anisotropic property of wet etching and the hard control on the precise. The design of the proof mass was thereby changed from pyramid to cubic. The thickness of the proof mass (silicon) was fixed by the thickness of the 4" wafer ($\sim 500 \mu\text{m}$). Besides, the thickness of PZT film, and the thickness of Si supporting layer were also fixed at $1 \mu\text{m}$ and $20 \mu\text{m}$ respectively, and other thinner layers were neglected to simplify calculation. Schematic diagram of the simplified configuration of the MEMS-scale PZT cantilever is given in Figure 6-3.

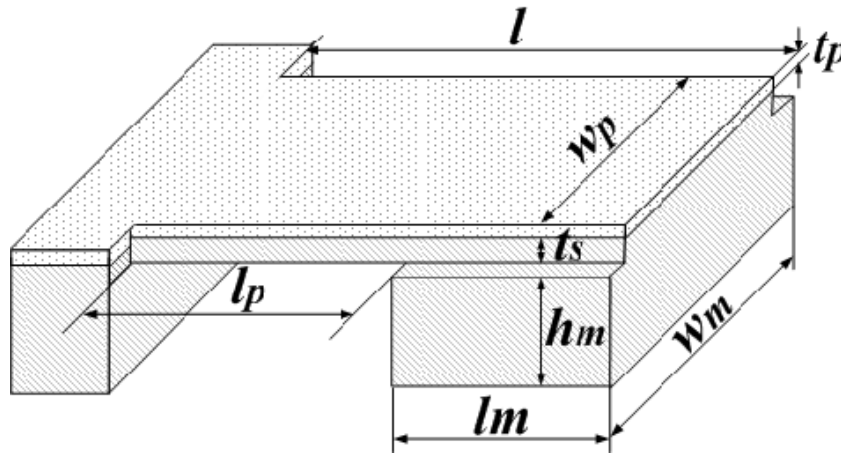


Figure 6- 3 Schematic diagram and notations of the simplified configuration of a piezoelectric power harvesting device.

Here the cantilever is a unimorph configuration, which is different from the bimorph discussed in section 3.1.2.1. Equations (6-1) - (6-4) are used to calculate the resonant frequency of a unimorph cantilever with a proof mass:

$$f_n = \frac{v_n^2}{2\pi} \sqrt{\frac{0.236D_p w}{(l - l_m / 2)^3 [m_e + \Delta m]}} \quad (6-1)$$

$$D_p = \frac{E_p^2 t_p^4 + E_s^2 t_s^4 + 2E_p E_s t_p t_s (2t_p^2 + 2t_s^2 + 3t_p t_s)}{12(E_p t_p + E_s t_s)} \quad (6-2)$$

$$m_e = 0.236mw(l - \frac{l_m}{2}) + mw\frac{l_m}{2} \quad (6-3)$$

$$m = \rho_p t_p + \rho_s t_s \quad (6-4)$$

where the subscript *s* is silicon, and all other parameters are defined as before.

After fabrication and evaluation of the first design as shown in Appendix A, the devices were found with higher output power but low safety factor. The modified dimensions of rectangular cantilevers were designed. The rules of design are the same as before. The resonant frequency was calculated by Equations (6-1). To calculate the safety factor of a device, the unimorph structure as shown in Figure 6-4 (a) was firstly transformed to the form shown in Figure 6-4 (b) because the different Young's modulus between these two materials.

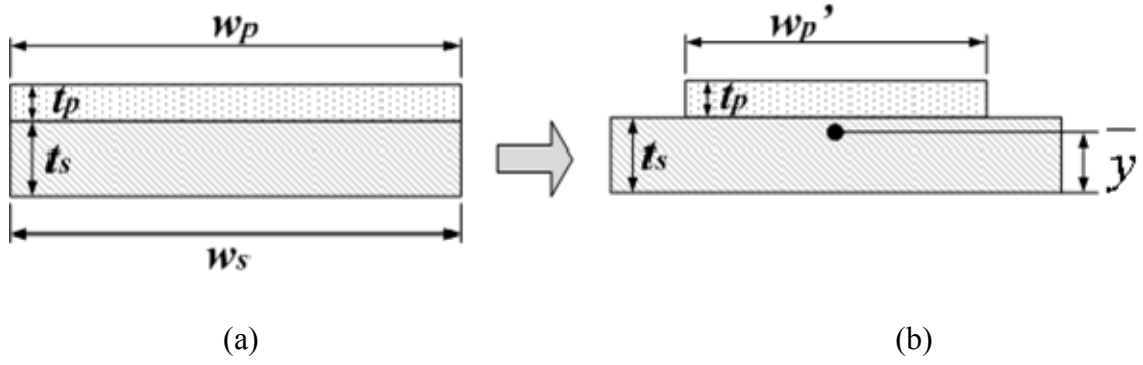


Figure 6- 4 Schematic diagram used to calculate the maximum stress in PZT film.

And then, the safety factor was calculated by:

$$S = \frac{\sigma_{ys}}{\sigma_{max}} = \frac{\sigma_p}{\sigma_p} \quad (6-5)$$

$$\sigma_p = \frac{E_p}{E_s} \sigma_p' = \frac{E_p M (t_p + t_s - \bar{y})}{E_s I} \quad (6-6)$$

$$M = \Delta m a \left(l_p + \frac{l_m}{2} \right) + m_b a \left(\frac{l_p + l_m}{2} \right) \quad (6-7)$$

$$I = \frac{1}{12} w_s t_s^3 + w_s t_s \left(\bar{y} - \frac{t_s}{2} \right)^2 + \frac{1}{12} w_p' t_p^3 + w_p' t_p \left(\frac{t_p}{2} + t_s - \bar{y} \right)^2 \quad (6-8)$$

$$w_p' = \frac{E_p}{E_s} w_p \quad (6-9)$$

$$\bar{y} = \frac{\frac{1}{2} t_s^2 w_s + \left(\frac{1}{2} t_p + t_s \right) t_p w_p'}{t_s w_s + t_p w_p'} \quad (6-10)$$

where S is the safety factor or maximum operational acceleration of the device, σ_{ys} the yield strength or fracture strength of the weakest material (PZT here), σ_{max} the maximum

stress generated in the beam surface at the clamping area, σ_p the maximum stress generated in the PZT film, as shown in Figure 6-5 (a) ($\sigma_p = \sigma_{max}$ here), σ_p' the maximum stress generated in the PZT film as shown in Figure 6-4 (b), M the moment of the cantilever with a proof mass, I the moment of inertia of the cantilever, a the input acceleration, m_b the weight of the cantilever beam without the proof mass, here the proof mass was simplified into a point at the middle of the proof mass, other parameters are the same as before.

One of the difficulties in the modeling and design is the uncertain characteristics of thin film materials. The properties of the two materials used in calculation are listed in Table 6-3. The Young's moduli of both materials vary a lot from different conditions. These values were found from publications, but not verified yet. The yield strengths of two materials are also hard to measure, especially for the PZT film. This yield stress value of the PZT film is actually the property of a bulk PZT material. The real value of the yield stress of PZT thin film should be much lower. Based on the above reasons, the calculation of safety factor will not be accurate. But, it can help to estimate the safety factor change from design to design.

Table 6. 3 The characteristics of materials used for calculation.

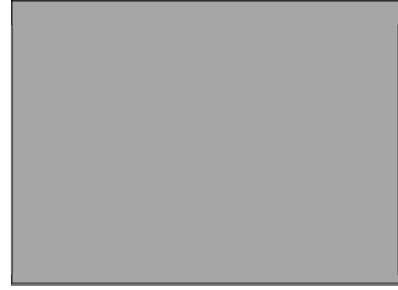
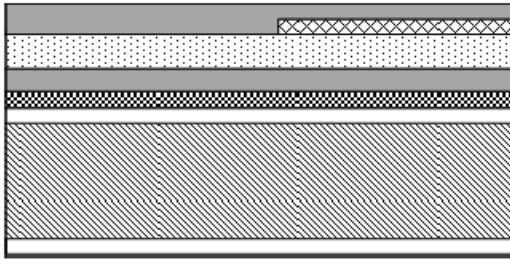
Characteristics	PZT	Si (P-type)
Young's modulus [GPa]	63	62
Mass density [kg/m ³]	7600	2330
Yield (or fracture) strength [MPa]	20*	6900

* The property of bulk PZT material, the strength of PZT film should be lower than this value.

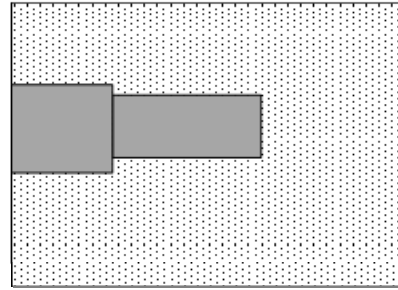
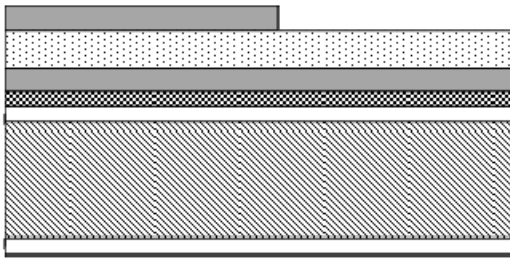
All designed dimensions of micro-cantilevers are listed in Appendix A. All designed masks used to fabricate micro-cantilevers are listed in Appendix B. Appendix C presents the whole wafer pictures of the fabricated first generation micro-cantilevers.

6.2.2 Device fabrication and equipment

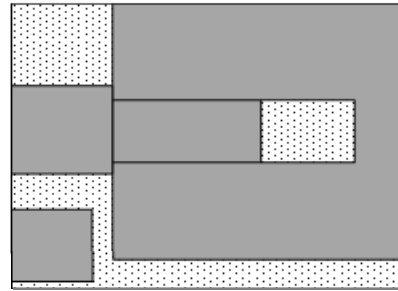
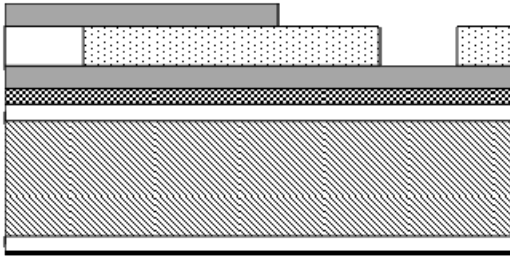
A four-mask process was used to fabricate the PZT cantilever, as shown in Figure 6-5. The fabrication process began with a 100 mm low cost bare silicon wafer. SiO₂ was grown on both sides of the silicon wafer by wet O₂ method. Interlayer Ti and electrode Pt were deposited one after another by magnetron sputtering. PZT was deposited layer by layer using the sol-gel method described in Figure 6-6 to reach a thickness of 1 μm. Commercial PZT sol-gel solution was provided by Inostek, Korea. The top electrode was patterned by the first mask and obtained by liftoff process after Pt deposition on a layer of patterned photo resist (PR). The bottom electrode together with the cantilever structure were patterned by the second mask and etched by inductively coupled plasma (ICP) reactive ion etching (RIE) to create a bare window for easy access during wire bonding. The cantilever structure without bottom electrode was then patterned by the third mask and etched by RIE. The back side proof mass was finally patterned by the fourth mask and the cantilever structure was finally released after back side Si RIE.



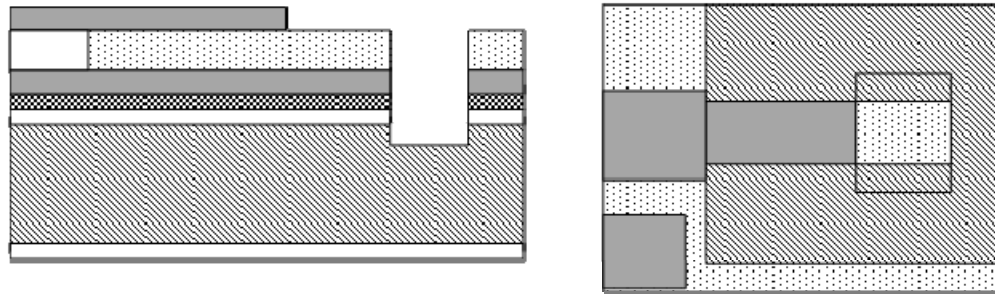
(a)



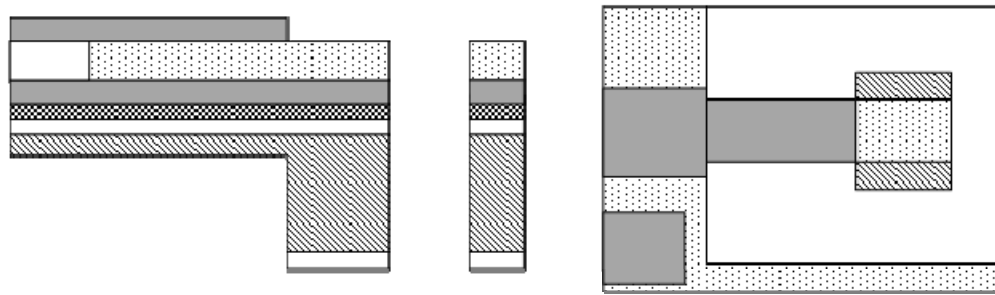
(b)



(c)



(d)



(e)



Figure 6- 5 Fabrication flow chart: (a) multilayer deposition; (b) top electrode patterning by liftoff (mask 1) (c) bottom electrode opening via RIE (mask 2) (d) cantilever patterning by RIE (mask 3) (e) proof mass patterning and cantilever release via backside RIE (mask 4).

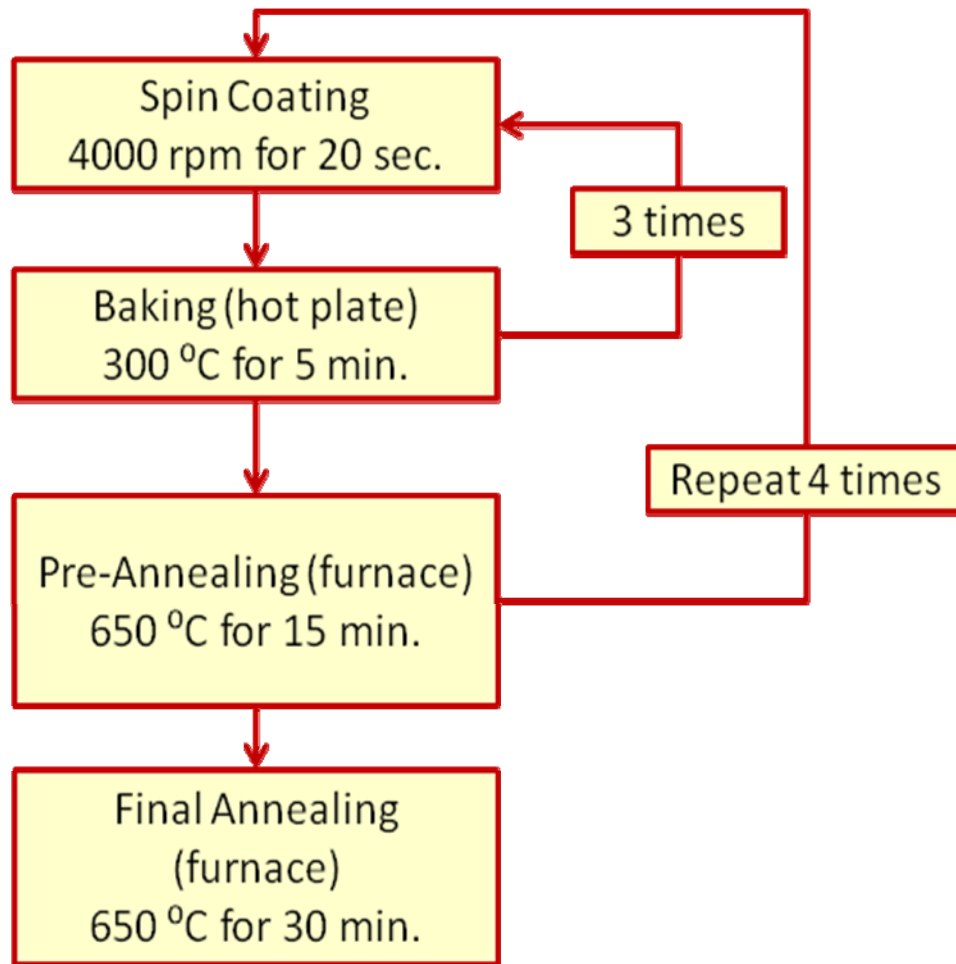


Figure 6- 6 PZT thin film deposition flow chart.

The summary of the proposed detailed processes and experimental parameters are listed in Table 6.4. Some parameters may change according to the equipment availability and experimental conditions.

Table 6. 4 Fabrication details of PZT micro-cantilever power generator.

Material or process	Method	Thickness	Experimental conditions
Si wafer	commercial Czochralski	~550 μm	N/A
SiO ₂	Wet oxidation	500 nm	N/A
Ti Cr	Magnetron sputtering	10 nm 10 nm	400 W (DC), 25 sec, 25 sccm Ar 300 W (DC), 10 sec, 25 sccm Ar
Electrode Pt	Magnetron sputtering	120 nm	100 W (DC), 360 sec, 25 sccm Ar
PZT 52/48	commercial Sol-gel	1 μm	[(4000 rpm, 22 sec, 300 °C, 15 min pyrolysis) 3 times + 650 °C, 15 min pre-annealing] + 650 °C, 30 min final annealing → totally 12 layers
1 st mask: PR 5214 pattern	lithography	1.5 μm	3000 rpm 30 sec, 105 °C soft bake 30 sec, UV exposure 15 sec, 400K (1:3) develop 1.2 min, 120 °C hard bake 30 sec
Electrode Pt	Magnetron sputtering	120 nm	100 W (DC), 360 sec, 25 sccm Ar
Acetone	liftoff	-	Acetone, Methanol, DI water rinse
2 nd mask: cantilever patterning	Lithography	~15 μm	(500 rpm 40 sec, 105 °C soft bake 30 sec) 3 times + UV exposure 180 sec, 400K (1:3) develop 1.2 min, 120 °C hard bake 30 sec
PZT, Ti, and SiO ₂ etching	ICP RIE	~1.75 μm	600W(c), 150W(p), 30sccm(SF ₆), 240 V bias
2 nd mask: cantilever patterning	Lithography	~15 μm	(500 rpm 40 sec, 105 °C soft bake 30 sec) 3 times + UV exposure 180 sec, 400K (1:3) develop 1.2 min, 120 °C hard bake 30 sec
front Si etching	ICP RIE	20 μm	Etching: 600W(coil), 12W(platen), 130 sccm (SF ₆), 13 sccm (O ₂), 13 sec; Passivation : 600W(coil), 0W(platen), C ₄ F ₈ 85 sccm, 7 sec
3 rd mask: back pattern	Lithography	~15 μm	(500 rpm 40 sec, 105 °C soft bake 30 sec) 3 times + UV exposure 180 sec, 400K (1:3) develop 1.2 min, 120 °C hard bake 30 sec
Si etching	Lithography & ICP RIE	~500 μm	Etching: 600W(coil), 12W(platen), 130 sccm (SF ₆), 13 sccm (O ₂), 13 sec; Passivation : 600W(coil), 0W(platen), C ₄ F ₈ 85 sccm, 7 sec; 17 mTorr, 230 V bias

6.3 Evaluation and measurement

The fabricated devices were cleaned, wire bonded, and evaluated. The dimensions of one of the devices were measured using SEM (JEOL 7000 FE).

The piezoelectric property, especially for the hysteresis loop of piezoelectric film of device was characterized by a TF analyzer 2000 measurement system (axiACCT systems), as shown in Figure 6-7. Thorough this test, the quality of the PZT film and the top electrode of a device can be easily estimated since we have already a large amount of data about the piezoelectric properties of the PZT film stated in section 6.1. If there is a signal of short circuit, it is likely the device is bad. If there is a signal of open circuit, the connection of wires should be examined.



Figure 6- 7 TF analyzer 2000 measurement system (axiACCT).

The resonant frequency of device was characterized by the impedance analyzer (Agilent Technologies, 4294A). The 100~200 Hz of resonant frequency is the one of the main target of this project. Due to the complexity of MEMS device and fabrication, the simplified model stated in section 6.2 could show large deviation. Therefore, the model or even the parameters used in the model should be optimized by comparing the experimental results and the calculation.

The output behavior of device was characterized again by the experimental set up shown in Figure 3-15. The output behavior of a device was measured by varying resistance loads, vibration frequency, and vibration acceleration. By varying the resistance loads at certain acceleration, the optimal resistance can be found. By varying the vibration frequency at certain acceleration, the resonant frequency at the vibration acceleration can be found.

6.4 Results and discussion

6.4.1 Designed mask and fabricated PZT micro power generators

In the first generation design, three masks were used. In the second and the third generation design, four masks were used with one more bottom electrode mask for easy access of wire bonding, and bigger bonding area was added to the top electrode for precise calculation of the electrode area. All designed masks are presented in Appendix B.

The following results are measured from one of the fabricated PZT micro-cantilever from the 3rd generation design.

SEM pictures of one of the fabricated cantilever devices are shown in Figure 6-8. From the pictures we can see the clearly defined straight cantilever beam along with the undersized proof mass. The straight beam shows little internal stress, which demonstrates the practicable layer structure of the device and the fabrication process. The undersized proof mass resulted from shrinkage of the photo resist which was used as barrier layer during RIE. A thin layer of SiO₂ may be a better choice for the barrier layer even though it would increase the complexity of fabrication.

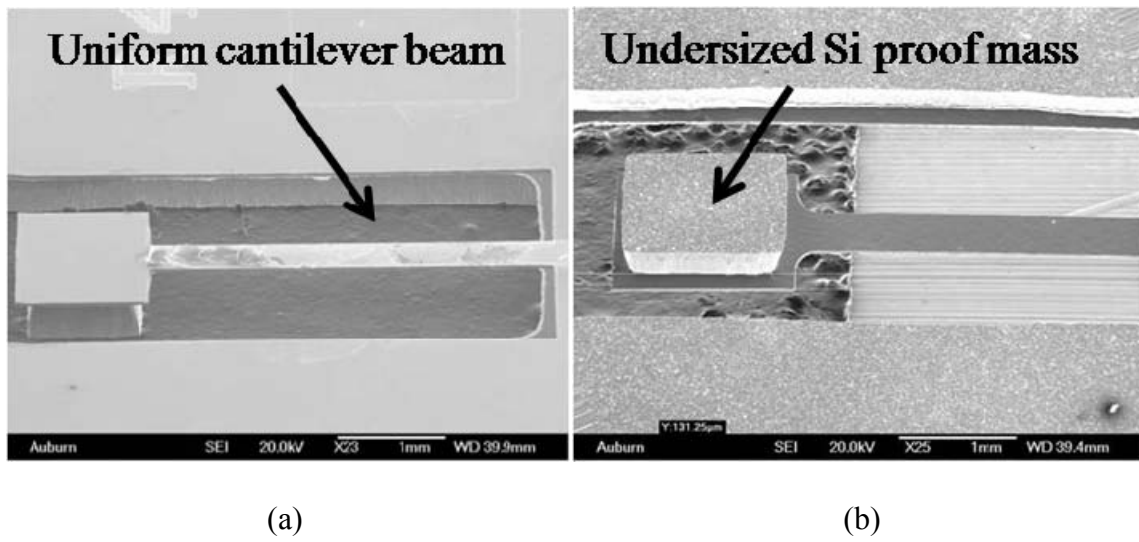


Figure 6- 8 SEM pictures of a fabricated PZT cantilever energy harvesting device: (a) front side; (b) back side.

The measured dimensions of the device and the calculated effective volume are listed in Table 6.5. Both the width and the length of the cantilever beam were uniform and consistent with the designed dimensions, but the width and the length of the proof

mass and the thickness of the supporting Si layer were inconsistent to the design due to the shrinkage of the photo resist and the nonuniform etching rate of the RIE system. The thicker supporting layer and the undersized proof mass will result in a higher resonant frequency. However, a SOI (Silicon on Insulator) wafer is a good choice to precisely control the thickness and uniformity of the supporting Si layer.

Table 6. 5 Measured dimensions and effective volume of the PZT device (μm).

l_p	w_p	t_{PZT}	t_{Si}	l_m	w_m	h_m	$Vol (\text{mm}^3)$
3200	400	1	35	1360	940	456	0.6520

6.4.2 Property of PZT thin film and power output of PZT micro power generators

Figure 6-9 shows the measured polarization versus electric field hysteresis loop of the PZT cantilever device after wire bonding. The remnant polarization was $17.8 \mu\text{C}/\text{cm}^2$ at an electric field of 25 MV/m. This value is same as the value measured before wire bonding. The PZT film retained excellent properties after the long term fabrication process.

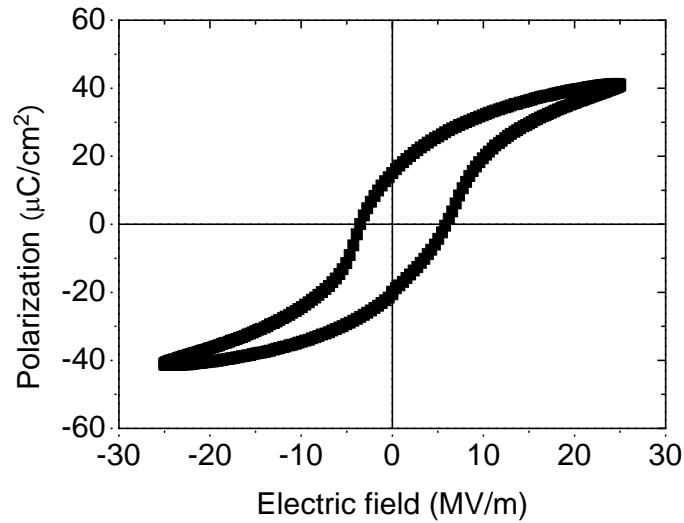


Figure 6- 9 Piezoelectric hysteresis loop measured from the wire-bonded PZT cantilever device.

Figure 6-10 is the measured resonant frequency of the PZT cantilever using the impedance analyzer. The peak of phase angle curve is at 462.5 Hz. The calculated value using the measured dimensions is about 423 Hz, a difference of about 9.4%. This discrepancy is attributed mainly to the simplifications to the model ignoring other thinner layers and assuming perfect adhesion between layers, the effect of the large proof mass on the cantilever stiffness through a point away from the end tip, and the measurement errors of the physical dimensions of the cantilever, especially on the thickness, which is critical to the resonant frequency. Furthermore, the undersized proof mass and the thicker supporting Si layer resulted in a higher resonant frequency than the target design resonant frequency (140 Hz). To reach the targeted resonant frequency, precise

dimension control on the process is crucial. Improved fabrication procedures would minimize the difference between the designed and measured resonant frequencies.

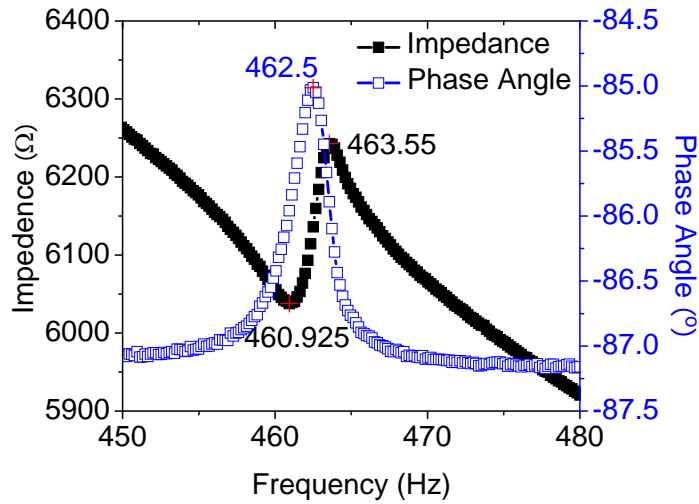


Figure 6- 10 Measured impedance and phase angle of the PZT cantilever vs. frequency.

The Q-factor calculated from the phase angle peak is about 233. A high Q-factor means low energy loss, which is good for an energy converter; however, a high Q-factor also means large sensitivity of the output behavior of a device to the environmental vibration frequency. A little deviation of the vibration frequency from the device's resonant frequency will induce tremendous reduction of the output power. A lower Q-factor will be preferred as long as the output power is high enough to support the application requirements.

Figure 6-11 shows the AC output of the device in its optimal resistive load of 6 kΩ from 1g acceleration at its resonant frequency of 461.25 Hz.

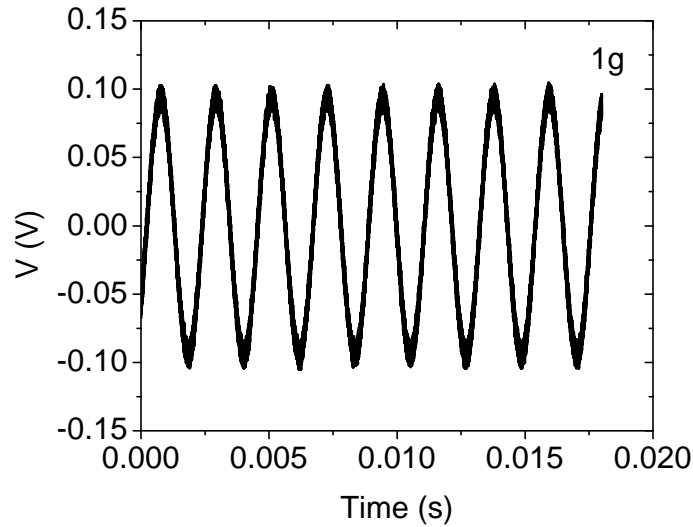


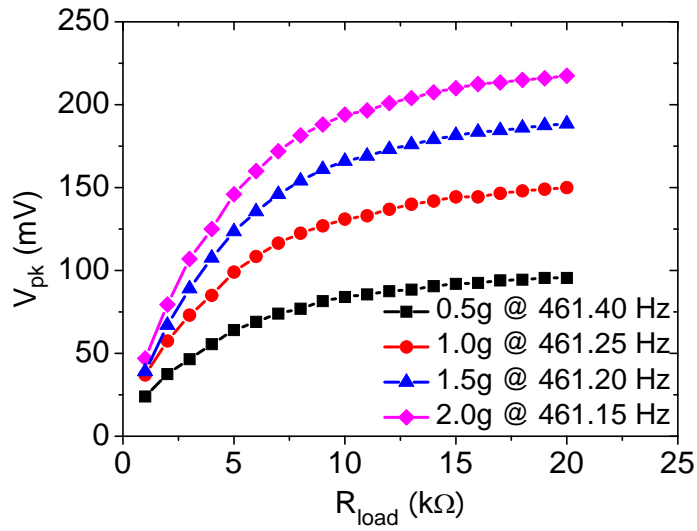
Figure 6- 11 AC output at 1g vibration with a 6 kΩ resistive load.

Figure 6-12 shows the peak voltage ($V_{pk} = V_{pk-pk} / 2$) and average power ($P_{ave} = V_{rms}^2 / R_{load}$) of the device versus the resistive load at 0.5g, 1.0g, 1.5g, and 2.0g accelerations and corresponding resonant frequencies, which were obtained from experiment. The resonant frequency gradually decreases with acceleration amplitude is mainly attribute to the increasing elastic compliance of PZT due to nonlinear effects under large stress [33-35]. The optimal resistive load was found from Figure 6-12 (b), which is the resistance when the maximum power generation is obtained. The optimal

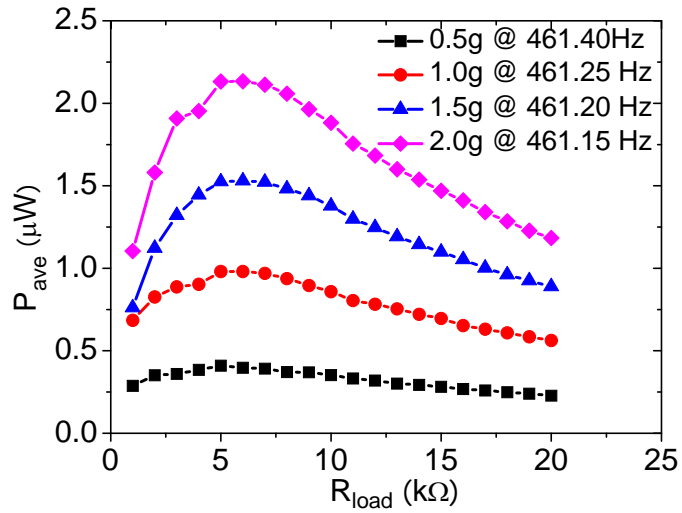
resistance increases slightly with the excitation acceleration amplitude since the mechanical damping of the device increases with stress [34], and the electrical damping must be increased to match the mechanical damping to maximize the output power. Increasing the resistive load is a convenient approach to increasing the electrical damping because the electrical damping is proportional to the resistive load [36].

The maximum output power of 2.15 μW was 3272 $\mu\text{W}/\text{cm}^3$. The power density was calculated using the average power divided by the effective volume of the device, which is the volume of the entire beam and the Si proof mass calculated from the measured data in Table 6.5. The effective volume instead of the operation volume was used for comparison with other power generators in references.

The continuous power requirements for a typical bio MEMS system has been reported to be 10 mW, however; many bio systems may operate with an intermittent power source rather than a continuous one [37]. If an application needs 10 mW of power only once per 80 minutes, for example, the power generated by this PZT cantilever would be sufficient.



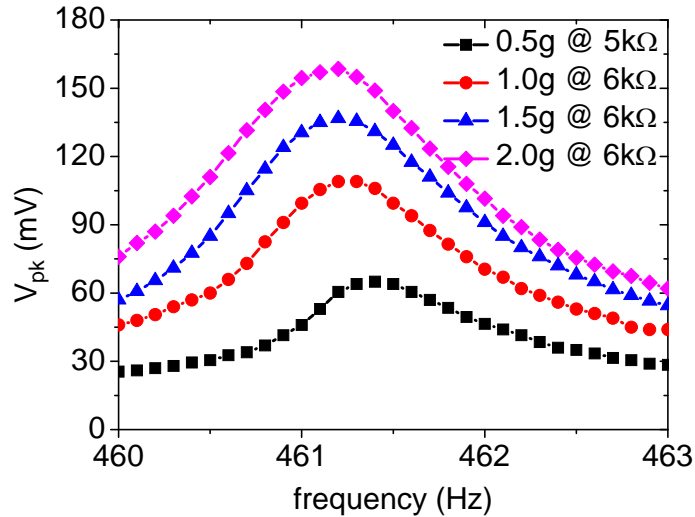
(a)



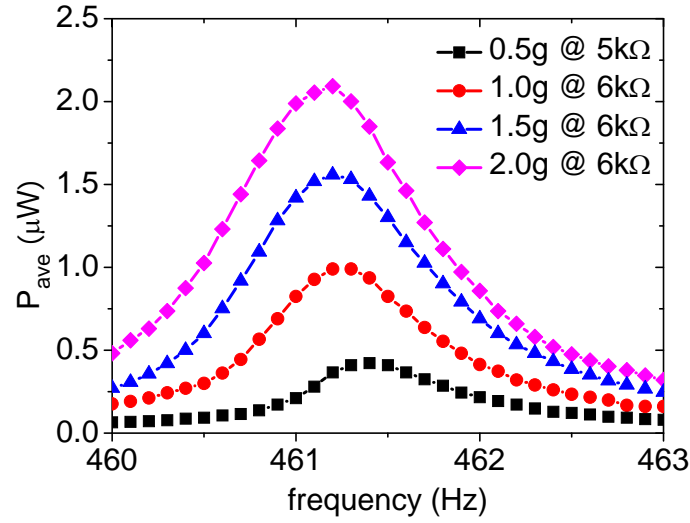
(b)

Figure 6- 12 (a) Peak voltage and (b) average power vs. resistive load.

Figure 6-13 shows the peak voltage and average power of the device versus the vibration frequency at 0.5g, 1.0g, 1.5g, and 2.0g accelerations and corresponding optimal resistive loads obtained from Figure 6-12 (b). The resonant frequencies of this device at different accelerations apparently shifted to lower frequency with increasing exciting vibration amplitude. In Figure 6-13 (a), the V_{pk} is not linearly related to the acceleration amplitude, but increases more and more slowly. This is because of the nonlinear response of PZT under large stress; both the elastic compliance and damping coefficient increase when the stress is sufficiently large while the piezoelectric constant decreases with increasing stress [35]. The power does not increase in a quadratic relationship with the acceleration but increases more and more slowly for the same reason.



(a)



(b)

Figure 6- 13 (a) peak-peak voltage (b) average power vs. vibration frequency.

Besides the output behavior of this device, the damping ratio (ζ) was also calculated at different accelerations. For a damped harmonic oscillator, the mass m , natural angular frequency ω_0 , viscous damping coefficient c , and the damping ratio ζ (defined as the ratio between the damping coefficient c and the critical damping coefficient c_c) are related by $c = 2m\zeta\omega_0$ [36]. A large damping ratio indicates low power conversion efficiency and increased energy loss. The AC outputs of the PZT cantilever were recorded separately immediately after stopping the exciting vibration. The damping ratio can be calculated by [36]:

$$\zeta = \frac{1}{2\pi m} \ln(x_1 / x_2) \quad (6- 11)$$

where x_1 is the amplitude at one point in time and x_2 is a later amplitude measured after n periods of the sinusoidal response. For each acceleration amplitude evaluated, ten segments of the damped waveforms were randomly selected to obtain the amplitudes to be used in calculating the average damping ratios and the results shown in Figure 6-14. The ratio increases with the acceleration due to nonlinearity of PZT under large stress [34].

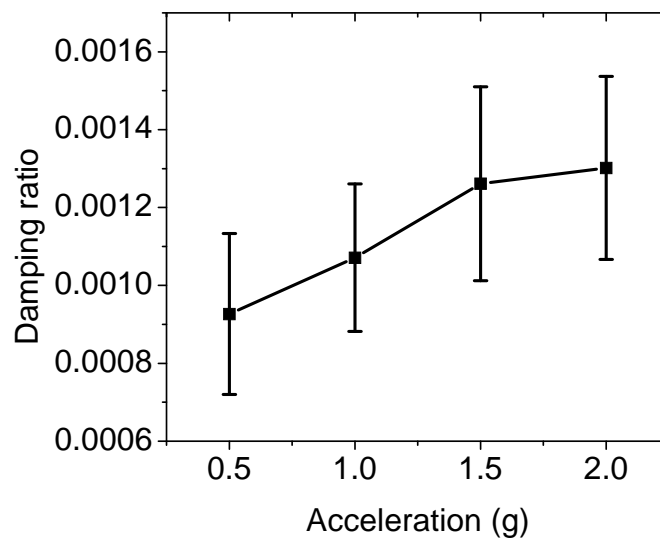
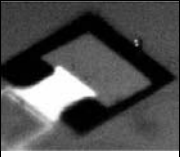
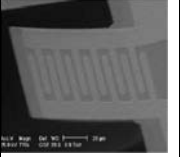

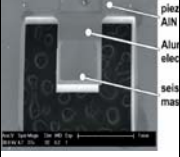
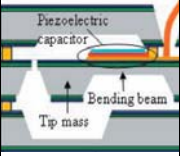
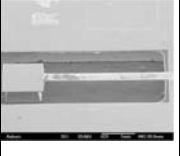


Figure 6- 14 Damping ratio increases with acceleration amplitude.

6.4.3 Comparison with other published MEMS energy harvesting devices

The working conditions, output behaviors, and pictures of this integrated MEMS PZT energy harvesting device together with other published MEMS piezoelectric power generators were list Table 6.4 for comparison.

Table 6. 6 Comparison among MEMS piezoelectric energy harvesting devices.

Author	Device	Effective volume (mm ³)	Power (μW)	Power density (μW/cm ³)	A (g)	f (Hz)	Picture or schematic
Marzecki 2005 [12]	d ₃₁ AlN cantilever	3.8 ^a	0.038	10	0.5	204	
Jeon 2005 [9]	d ₃₃ PZT cantilever	0.027 ^a	1.01	37037 ^a	10.8	13.9k	
Fang 2006 [8]	d ₃₁ PZT cantilever	0.1992 ^a	2.16	10843 ^a	1.0	608	
Marzecki 2007 [13]	d ₃₁ AlN cantilever	>0.552 ^a	1.97	< 3569 ^a	4.0	1368	
Renaud 2007 [14]	d ₃₁ PZT cantilever	1.845 ^a	40	21680 ^a	1.9 ^a	1.8k	
In this study	d ₃₁ PZT cantilever	0.6520	2.15	3272	2.0	462.5	

^a Estimated from data in reference.

6.5 Chapter summary

A MEMS PZT energy harvesting cantilever with an integrated Si proof mass was designed, fabricated, and evaluated. The fabricated device has beam dimensions of about $4.800 \text{ mm} \times 0.400 \text{ mm} \times 0.036 \text{ mm}$ with an integrated Si proof mass with dimension of about $1.360 \text{ mm} \times 0.940 \text{ mm} \times 0.456 \text{ mm}$. The effective volume, beam plus proof mass, is about 0.6520 mm^3 . It produced $160 \text{ mV}_{\text{pk}}$, $2.15 \text{ }\mu\text{W}$, or $3272 \text{ }\mu\text{W cm}^{-3}$ with an optimal resistive load of $6 \text{ k}\Omega$ from 2g acceleration at its resonant frequency of 461.15 Hz .

References

- [1] M.-A. Dubois and P. Muralt, "Measurement of the effective transverse piezoelectric coefficient e_{31} of AlN and $\text{Pb}(\text{Zr}_x\text{Ti}_{1-x})\text{O}_3$ thin films," *Sensors and Actuators A: Physical*, vol. 77, pp. 106-112, 1999.
- [2] X. J. Zheng, Y. C. Zhou, J. M. Liu, and A. D. Li, "Use of nanomechanical fracture-testing for determining the interfacial adhesion of PZT ferroelectric thin films," *Surface and Coatings Technology*, vol. 176, pp. 67-74, 2003.
- [3] L. M. R. Eakins, B. W. Olson, C. D. Richards, R. F. Richards, and D. F. Bahr, "Microstructural characterization and mechanical reliability of interfaces in piezoelectric based microelectromechanical systems," *Thin Solid Films*, vol. 441, pp. 180-186, 2003.
- [4] K. Sameshima, T. Nakamura, K. Hoshiba, Y. Nakao, A. Kamisawa, T. Atsuki, N. Soyama, and K. O, "Preparation of $\text{Pb}(\text{Zr}, \text{Ti})\text{O}_3$ films on Pt/Ti/Ta electrodes by sol-gel process," *Japanese Journal of Applied Physics, Part 1: Regular Papers & Short Notes & Review Papers*, vol. 32, pp. 4144-4146, 1993.
- [5] K. B. Lee, S. Tirumala, and S. B. Desu, "Highly c-axis oriented $\text{Pb}(\text{Zr}, \text{Ti})\text{O}_3$ thin films grown on Ir electrode barrier and their electrical properties," *Applied Physics Letters*, vol. 74, pp. 1484-1486, 1999.
- [6] C.-H. Lin, W.-D. Hsu, and I. N. Lin, "Ferroelectric properties of $\text{Pb}(\text{Zr}_{0.52}\text{Ti}_{0.48})\text{O}_3$ thin films prepared by metal-organic decomposition process," *Applied Surface Science*, vol. 142, pp. 418-421, 1999.
- [7] Y. K. Tseng, K. S. Liu, S. F. Huang, Y. Chi, and I. N. Lin, "Improvement on ferroelectric properties of metal-organic decomposed PZT thin film prepared by using prenucleation layer," Aachen, 2000, pp. 157-164.
- [8] X. J. Zheng, Y. C. Zhou, and H. Zhong, "Dependence of fracture toughness on annealing temperature in $\text{Pb}(\text{Zr}_{0.52}\text{Ti}_{0.48})\text{O}_3$ thin films produced by metal organic decomposition," *Journal of Materials Research*, vol. 18, pp. 578-584, 2003.
- [9] H.-F. Cheng, Y.-C. Lin, C.-H. Lin, and I. N. Lin, "Enhancement on crystallization kinetics of $\text{Pb}(\text{Zr}_{1-x}\text{Ti}_x)\text{O}_3$ thin films prepared by metal-organic decomposition process by the incorporation of nano-powders," Shanghai, China, 2005, pp. 69-79.
- [10] S. Fujii, I. Kanno, T. Kamada, and R. Takayama, "Preparation of c-axis oriented $\text{Pb}(\text{Zr}, \text{Ti})\text{O}_3$ thin films by RF-magnetron sputtering and their dielectric and piezoelectric properties," *Japanese Journal of Applied Physics, Part 1: Regular Papers & Short Notes & Review Papers*, vol. 36, pp. 6065-6068, 1997.

- [11] X.-S. Li, T. Tanaka, and Y. Suzuki, "Preferred orientation and ferroelectric properties of lead zirconate titanate thin films," *Thin Solid Films*, vol. 375, pp. 91-94, 2000.
- [12] H.-J. NAM, H.-H. KIM, and W.-J. L. LEE, "The Effects of the Preparation Conditions and Heat-Treatment Conditions of Pt/Ti/SiO₂/Si Substrates on the Nucleation and Growth of Pb(Zr,Ti)O₃ Films," *Japanese Journal of Applied Physics, Part 1: Regular Papers & Short Notes & Review Papers*, vol. 37, pp. 3462-3470, 1998.
- [13] S.-T. Kim, H.-H. Kim, M.-Y. Lee, and W.-J. Lee, "Investigation of Pt/Ti bottom electrodes for Pb(Zr, Ti)O₃ films," *Japanese Journal of Applied Physics, Part 1: Regular Papers & Short Notes & Review Papers*, vol. 36, pp. 294-300, 1997.
- [14] I. Kanno, S. Fujii, T. Kamada, and R. Takayama, "Piezoelectric properties of c-axis oriented Pb(Zr, Ti)O₃ thin films," *Applied Physics Letters*, vol. 70, pp. 1378-1380, 1997.
- [15] C. C. Mardare, E. Joanni, A. I. Mardare, C. P. M. de Sa, and P. B. Tavares, "The performance of Zr as barrier layer for Pt bottom electrodes in Pb(Zr,Ti)O₃ thin film capacitors," *Thin Solid Films*, vol. 483, pp. 21-26, 2005.
- [16] K. Tokita, M. Aratani, and H. Funakubo, "Substrate effect on the crystal structure and ferroelectricity of low-temperature-deposited Pb(Zr, Ti)O₃ thin films by metalorganic chemical vapor deposition," *Applied Physics Letters*, vol. 82, pp. 4122-4124, 2003.
- [17] M. Aratani, K. Nagashima, and H. Funakubo, "Preparation of Pb(Zr_x, Ti_{1-x})O₃ thin films by source gas pulse-introduced metalorganic chemical vapor deposition," *Japanese Journal of Applied Physics, Part 1: Regular Papers and Short Notes and Review Papers*, vol. 40, pp. 4126-4130, 2001.
- [18] S. H. Choi, B. J. Bae, Y. H. Son, J. E. Lim, D. C. Yoo, D. H. Im, J. E. Heo, S. D. Nam, J. H. Park, C. K. Hong, H. K. Cho, and J. T. Moon, "Study on electrical properties of flattened MOCVD PZT film by CMP process," Shanghai, China, 2005, pp. 215-223.
- [19] Y. Ruan, D. Xie, T.-L. Ren, H.-W. Lin, and L.-T. Liu, "MOCVD technology for PZT thin films," *Nami Jishu yu Jingmi Gongcheng/Nanotechnology and Precision Engineering*, vol. 6, pp. 64-67, 2008.
- [20] R. N. Castellano and L. G. Feinstein, "Ion-beam deposition of thin films of ferroelectric lead zirconate titanate (PZT)," *Journal of Applied Physics*, vol. 50, pp. 4406-4411, 1979.

- [21] I. Kanno, S. Hayashi, T. Kamada, M. Kitagawa, and T. Hirao, "Characterization of Pb(Zr, Ti)O₃ thin films prepared by multi-ion-beam sputtering," *Japanese Journal of Applied Physics, Part 1: Regular Papers & Short Notes & Review Papers*, vol. 33, pp. 574-577, 1994.
- [22] I. Kanno, S. Hayashi, R. Takayama, H. Sakakima, and T. Hirao, "Processing and characterization of ferroelectric thin films by multi-ion-beam sputtering," *Nuclear Instruments & Methods in Physics Research, Section B: Beam Interactions with Materials and Atoms*, vol. 112, pp. 125-128, 1996.
- [23] P. Verardi, M. Dinescu, and F. Craciun, "Pulsed laser deposition and characterization of PZT thin films," *Applied Surface Science*, vol. 154, pp. 514-518, 2000.
- [24] S. Kuchipudi, H.-C. Lee, J.-H. Huang, and I. N. Lin, "Low temperature preparation of Pb(Zr_{0.52}Ti_{0.48})O₃ thin films using pulsed excimer laser annealing process," *Ferroelectrics*, vol. 328, pp. 33-40, 2005.
- [25] G. Suchaneck and G. Gerlach, "Ferroelectric thin films: Deposition, advanced film characterization and novel device concepts," *Ferroelectrics*, vol. 335, pp. 137-148, 2006.
- [26] H.-J. Nam, D.-K. Choi, and W.-J. Lee, "Formation of hillocks in Pt/Ti electrodes and their effects on short phenomena of PZT films deposited by reactive sputtering," *Thin Solid Films*, vol. 371, pp. 264-271, 2000.
- [27] T. Maeder, L. Sagalowicz, and P. Mural, "Stabilized platinum electrodes for ferroelectric film deposition using Ti, Ta and Zr adhesion layers," *Japanese Journal of Applied Physics, Part 1: Regular Papers & Short Notes & Review Papers*, vol. 37, pp. 2007-2012, 1998.
- [28] K. Sreenivas, I. Reaney, T. Maeder, N. Setter, C. Jagadish, and R. G. Elliman, "Investigation of Pt/Ti bilayer metallization on silicon for ferroelectric thin film integration," *Journal of Applied Physics*, vol. 75, p. 232, 1994.
- [29] J. O. Olowolafe, R. E. Jones, A. C. Campbell, R. I. Hegde, C. J. Mogab, and R. B. Gregory, "Effects of anneal ambients and Pt thickness on Pt/Ti and Pt/Ti/TiN interfacial reactions," *Journal of Applied Physics*, vol. 73, p. 1764, 1993.
- [30] K. Tokita, M. Aratani, and H. Funakubo, "Substrate effect on the crystal structure and ferroelectricity of low-temperature-deposited Pb(Zr, Ti)O₃ thin films by metalorganic chemical vapor deposition," *Applied Physics Letters*, vol. 82, pp. 4122-4124, 2003.
- [31] C. C. Mardare, E. Joanni, A. I. Mardare, J. R. A. Fernandes, C. P. M. D. Sa, and P. B. Tavares, "Effects of adhesion layer (Ti or Zr) and Pt deposition temperature on

the properties of PZT thin films deposited by RF magnetron sputtering," *Applied Surface Science*, vol. 243, pp. 113-124, 2005.

- [32] C. Millon, C. Malhaire, C. Dubois, and D. Barbier, "Control of the Ti diffusion in Pt/Ti bottom electrodes for the fabrication of PZT thin film transducers," *Materials Science in Semiconductor Processing*, vol. 5, pp. 243-247, 2002.
- [33] Qing-Ming Wang, Qiming Zhang, Baomin Xu, Ruibin Liu, and L. Eric Cross, "Nonlinear piezoelectric behavior of ceramic bending mode actuators under strong electric fields," *Journal of Applied Physics*, vol. 86, pp. 3352-3360, 1999.
- [34] L. Q. Yao, J. G. Zhang, L. Lu, and M. O. Lai, "Nonlinear dynamic characteristics of piezoelectric bending actuators under strong applied electric field," *Journal of Microelectromechanical Systems*, vol. 13, pp. 645-652, 2004.
- [35] "IEEE standard on piezoelectricity," New York, 1987.
- [36] S. Roundy, "Energy scavenging for wireless sensor nodes with a focus on vibration to electricity conversion," in *Engineering-Mechanical Engineering*. vol. Ph.D. Berkeley, CA: University of California, Berkeley, 2003.
- [37] M. J. Ramsay and W. W. Clark, "Piezoelectric energy harvesting for bio MEMS applications," Newport Beach, CA, 2001, pp. 429-438.

CHAPTER 7
DEMONSTRATION OF MEMS-SCALE PZT POWER GENERATOR PROTOTYPES
BASED ON A SOI WAFER

7.1 Introduction

Two difficulties had ever slowed down the development of MEMS piezoelectric energy harvesting devices: the fabrication of high quality piezoelectric thin film and the tuning of the resonant frequency of the device suitable for certain vibration environment. At the beginning, ZnO thin film was used as the piezoelectric energy harvesting material due to the easiness of fabrication, but the low piezoelectric constant obstructed further development. After high quality Pb(Zr,Ti)O₃ (PZT) thin films have been obtained in energy harvesting device fabrication, it has become the major interest in MEMS technology due to the high electro-mechanical coupling coefficient. However, the tuning of the resonant frequency of a piezoelectric energy harvesting device is rarely studied because of the difficulties in the resonant frequency modeling for multilayer structure and in the dimension precise control of a device during fabrication, which decides the resonant frequency.

In this chapter, we studied a multilayer unimorph thin film PZT cantilever with an integrated Si proof mass based on SOI (silicon on insulator) structure for low frequency vibration energy harvesting application. A Pt/PZT/Pt/Ti/SiO₂/Si/SiO₂ multilayer device

is generated, and the entire effective volume (beam and mass) is about 0.7690 mm^3 . The results are compared with a device fabricated on a Si wafer with the same dimension design as stated in Chapter 6. The difference between the calculated and measured resonant frequency has been decreased to 4.25% due to the precisely controlled thickness of the silicon supporting layer. The measured average power and power density from a resistive load of $16.0 \text{ k}\Omega$ connecting to the device in parallel at the 0.75 g ($g = 9.81 \text{ m/s}^2$) acceleration amplitude and at its resonant frequency of 183.8 Hz are respectively $0.32 \text{ }\mu\text{W}$ and $416 \text{ }\mu\text{W/cm}^3$.

A Pt/PZT/Pt/Ti/SiO₂/Si/SiO₂ multilayer thin film PZT cantilever with an integrated Si proof mass is designed and fabricated based on a SOI wafer for low frequency vibration energy harvesting application. It is necessary to match the resonant frequency with the vibration source to obtain optimal power output. The thickness of the device is the most sensitive factor impacting the resonant frequency of a composite cantilever, and the SiO₂ layer in the SOI wafer can precisely control the thickness of the silicon supporting layer in the cantilever beam. The entire effective volume of the fabricated device is about 0.7690 mm^3 . When excited at 0.75 g acceleration amplitude at its resonant frequency of 183.8 Hz , the AC output measured across a resistive load of $16 \text{ k}\Omega$ connecting to the device in parallel has an amplitude of 101 mV . The calculated average power and power density at the same measurement conditions are respectively $0.32 \text{ }\mu\text{W}$ and $416 \text{ }\mu\text{W/cm}^3$. The results are compared with a device fabricated on a Si wafer with the same dimension design. The difference between the calculated and measured resonant frequency has been decreased to 4.25% due to the precisely controlled thickness of the silicon supporting layer.

The resonant frequency of a vibration energy harvesting device is one of the most important parameter during designing because the maximum output power density is obtained when the vibration frequency matches the resonant frequency of the piezoelectric resonator. It has been reported that the power output will be dramatically reduced when the driving vibration frequency deviates from the resonant frequency [1]. Before designing a device, we have to decide a targeted frequency, which is the vibration frequency of the vibration source which we want to convert the energy into electricity. It has been reported that common environmental vibrations such as those found in a building exhibit moderate amplitudes ($< 1g$), and lower frequencies, typically between 60 and 200 Hz [2]. The targeted vibration frequency in this effort is approximately 142 Hz. A clamped-free cantilever structure with a proof mass at the free end tip was chosen not only because it is much easier to realize a low resonance frequency but also because the cantilever is effective at generating large strains for a given input force compared to other structures, such as all clamped membrane and clamped-clamped bridge. Piezoelectric materials are generally utilized in two modes for energy harvesting, 31 [3-5] and 33 [6]. Although the electro-mechanical coupling coefficient for the 33 mode is larger, we used the 31 mode because this mode more readily realizes lower resonant frequency and can generate larger strain for a given input force.

7.2 Device design, fabrication flow, and measurement

7.2.1 Device design

The schematic of the designed multilayer PZT cantilever energy harvest device is shown in Figure 7-1. The whole structure was based on a SOI wafer. Si at the free end tip was used as the proof mass to decrease the resonant frequency. Si in the whole cantilever beam was used as a supporting layer to improve the mechanical strength of the beam and to prevent the beam from bending in static status due to internal stress. SiO₂ was used as the insulator between bottom electrode Pt/Ti and Si, and to compensate the internal stress. Ti was used as the adhesion layer to improve the adhesion between PZT and Pt. Pt was used as the electrodes.

The dimension design of the device was based primarily on the resonant frequency calculation and pre-decided thicknesses of certain layers. The thickness of the proof mass and the thickness of the Si supporting layer were limited by the commercial 100 mm (4 inch) SOI wafer, approximately 500 and 20 μm respectively. The thickness of PZT thin film was fixed around 1 μm . All other thinner layers, such as Pt, Ti, and SiO₂ were ignored during modeling to simplify the calculation.

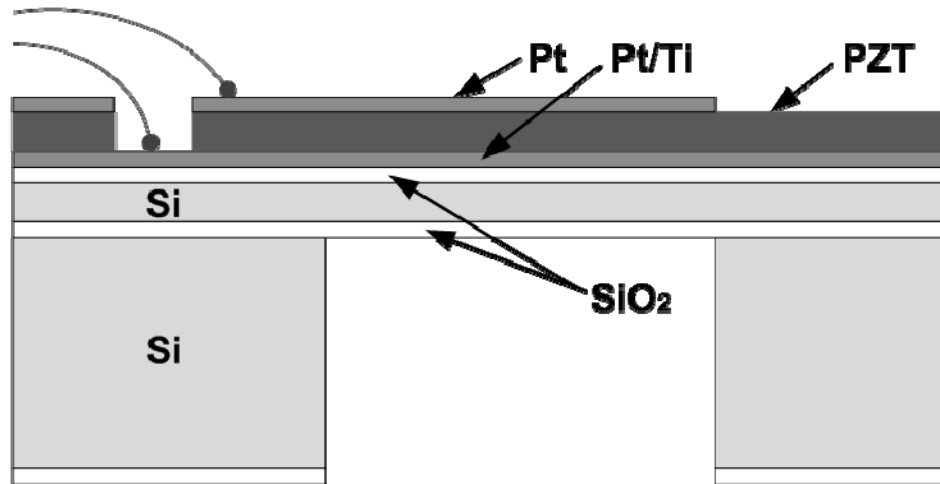


Figure 7- 1 Schematic diagram of the side view of a piezoelectric energy harvesting cantilever based on a SOI wafer.

The resonant frequency of a composite cantilever depends on its dimension when the materials have been decided. The model used to calculate the resonant frequency was based on a simplified unimorph cantilever with a big proof mass at the free end tip, that is, only the thicker PZT layer and the Si supporting layer were considered during the calculation. Equation (6-1) was used to calculate the resonant frequency.

7.2.2 Device fabrication flow

The MEMS fabrication process mainly consists of thin film deposition and etching with pattern. Inductive coupled plasma reactive ion etching (ICP RIE) system for anisotropy etching was used to etch out all layers and to release the cantilever beam with the Si proof mass. A Si supporting layer under the cantilever beam is necessary to

withstand the internal stress and to improve the mechanical strength of the beam. The thickness of this Si supporting layer is the key factor deciding the resonant frequency of a device when other dimensions are fixed because the resonant frequency is highly sensitive to thickness. However, it is hard to precisely control the thickness of Si supporting layer and to balance the etching rate and uniformity during the Si etching by the RIE process. The whole fabrication process was therefore starting based on a silicon-on-insulator (SOI) wafer, and the buried SiO₂ layer was used as an etching stop layer.

The fabrication flow based on the SOI wafer is more complex than that stated in Chapter 6. Four masks were used in the fabrication of MEMS PZT cantilever with a proof mass. The fabrication process began with a 100 mm SOI wafer. The thicknesses of the first silicon layer, the thermal silicon dioxide layer, and the second silicon layer are respectively 20 μm, 500 nm, and 450 μm. A layer about 500 nm thick of SiO₂ was grown on both sides of the SOI wafer by wet O₂ method. The silicon dioxide on the front surface will be used to balance the inertial stress of the PZT film, and the one on the back side surface could be used to mask areas of the surface to prevent damage during the back-side etching. Interlayer Ti (10 nm) and bottom electrode Pt (120 nm) were deposited sequentially by magnetron sputtering without breaking the vacuum. Ti was used for better adhesion between the oxide substrate and the bottom electrode Pt. Totally 13 layers of PZT was coated by sol-gel method to reach the thickness of 1 μm. Each layer was pyrolyzed for 10 minutes at 350 °C, and every three layer were annealed for 15 minutes at 650 °C. The top electrode was obtained by a liftoff process after Pt deposition on a layer of photo resist (PR) patterned by the first mask. With the protection of a thick layer of PR patterned by the second mask, the areas around PZT cantilever

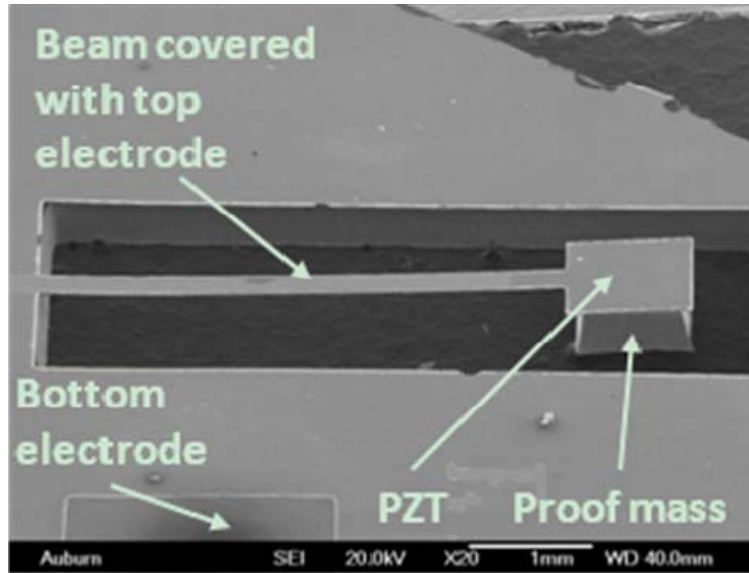
structures were etched by RIE until baring bottom electrode windows for easy access during wire bonding. After covering the areas of the cantilever structure and bottom electrode windows by another layer of PR patterned by the third mask, the areas around PZT cantilever structures were etched by RIE until the buried SiO₂ layer of the SOI wafer was removed, and the cantilever beam was then completely defined. The back side proof mass was patterned by the fourth mask and the areas without needing etching protected by a layer of PR. A Pt/PZT/Pt/Ti/SiO₂/Si/SiO₂ multilayer cantilever structure with an integrated silicon proof mass was finally released after back side SiO₂ and Si RIEs.

7.2.3 Device measurement

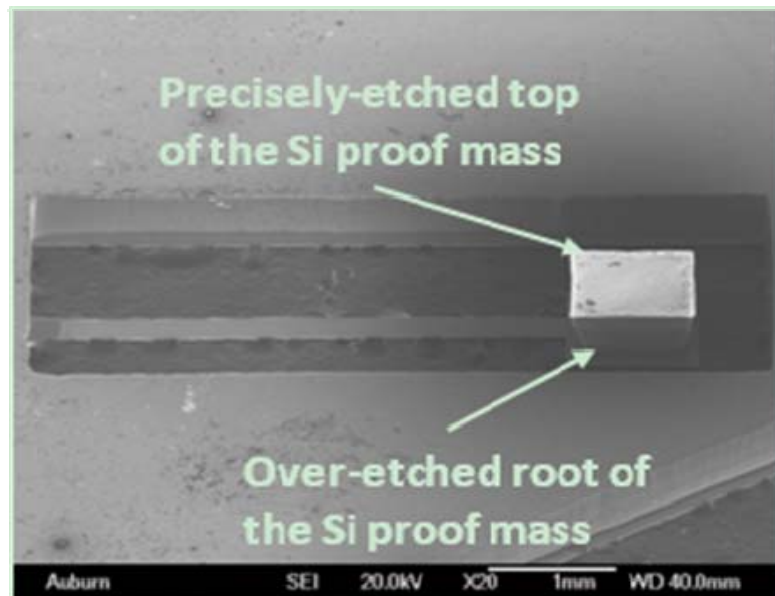
The fabricated devices were cleaned, wire bonded, and evaluated. The dimensions and the appearance of one of the cantilevers were measured using SEM (JEOL 7000 FE). The polarization-electric field hysteresis loop and the resonant frequency were measured using a TF Analyzer 2000 (aixACCT Systems), and an impedance analyzer (Agilent Technologies, 4294A). The output behavior of the device was evaluated using the experimental setup described Figure 3-15. The output voltages of the device at different vibration accelerations, different vibration frequencies, and different resistive loads were then systematically measured. The amplitudes of the output AC voltages were recorded and the corresponding output average powers were calculated.

7.3 Results and discussion

Figure 7-2 shows the 45° view of the fabricated cantilever taken from the (a) front and the (b) back side by SEM. From Figure 7-2 (a) we can see the clearly defined straight cantilever beam is slightly bending up due to internal stress in the PZT film. It is hard to completely eliminate the internal stress in such a long cantilever, and the small curvature of the beam has demonstrated the practicable layer structure of the device and the fabrication process. The top of the proof mass, as shown in Figure 7-2 (b), was more precisely etched when a thin layer of SiO₂ was used as the barrier layer in the back side Si deep etching process. However, the root of the proof mass was over etched due to the inconsistent back side etching. The reactive ion etching is the combination effects of physical ion bombardment and chemical ion reaction for improving the etching rate, but the chemical ion reaction increased the isotropic etching at the root areas with a relatively large bombardment pressure. The over-etched root could be mitigated in the cost of losing some etching rate. The undersized proof mass will decrease the resonant frequency of the cantilever, and the mass deduction of the proof mass should be considered during designing if the undersized proof mass is not completely evitable.



(a)



(b)

Figure 7- 2 SEM pictures of a cantilever (a) front and (b) back side 45° view fabricated on a SOI wafer.

The designed and measured dimensions and calculated volumes of the device are listed in Table 7.1. The volume is the sum of the volume of the cantilever beam and the volume of the proof mass. It has been decreased by 23% due to the undersized proof mass. The measured width and length of the proof mass are averaged values because the proof mass is not a uniform cuboid. The length of the cantilever beam without the proof mass was also prolonged due to the shrunk proof mass. The measured width of the cantilever beam and the thickness of the PZT layer are exactly consistent with the designed value. The thickness of the silicon supporting layer is about 1 μm thicker due to the other layers, such as SiO₂, and Ti/Pt. The undersized proof mass will result in a higher resonant frequency, however the SOI wafer has almost eliminated the gap between the designed and experimental thickness of silicon layer and this will highly decrease the difference between the designed and the experimental resonant frequencies of the device.

Table 7. 1 Dimensions of the cantilever (μm).

	l_p	w_p	t_p	t_s	l_m	w_m	h_m	$Vol. (\text{mm}^3)$
Designed	3200	400	1	20	1600	1200	500	0.9984
Measured	3293	400	1.2	21	1415	1015	506	0.7690

Figure 7-3 presents the measured polarization versus the electric field hysteresis loop of the PZT cantilever device at 25 V amplitudes of applied voltage after wire bonding. The remnant polarization is 28 $\mu\text{C}/\text{cm}^2$ at an electric field of 25 MV/m, and the coercive field is about 5 MV/m at the same electric field. These values are similar to the

values measured before wire bonding. The high saturation polarization and low coercive field show that the PZT film retained excellent properties after the long term of fabrication process.

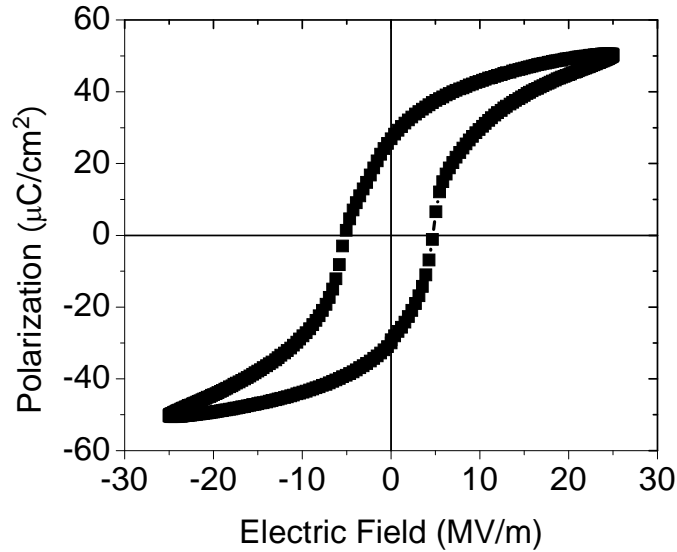


Figure 7- 3 Piezoelectric hysteresis loop measured from the wire-bonded PZT cantilever device.

The measured impedance and phase angle of the PZT cantilever versus the exciting frequency are shown in Figure 7-4. The resonant peak from the phase angle is at 184.16 Hz. This is higher than the designed value, 142 Hz, mainly due to the undersized proof mass. However, this difference (30%) has dramatically decreased comparing with the difference (230%) reported in Chapter 6, where the PZT cantilever was fabricated

based on a Si wafer and the thickness of the supporting silicon layer was hard to precisely control due to inconsistent RIE process. The calculated resonant frequency by Equation (6-1) using the measured dimensions shown in Table 7.1 is about 176.66 Hz, a difference of about 4.25% from the measured value. This discrepancy is mainly attributed to the modeling which simplified a multilayer structure to a two-layer structure and assuming perfect adhesion between layers, and the measurement errors of the physical dimensions of the cantilever, especially on the thickness, which is critical to the resonant frequency. According to these results, it is possible to precisely control the resonant frequency of a PZT cantilever with a big proof mass so long as fixing the back side etching parameters and getting to know the dimension change of the proof mass during the process.

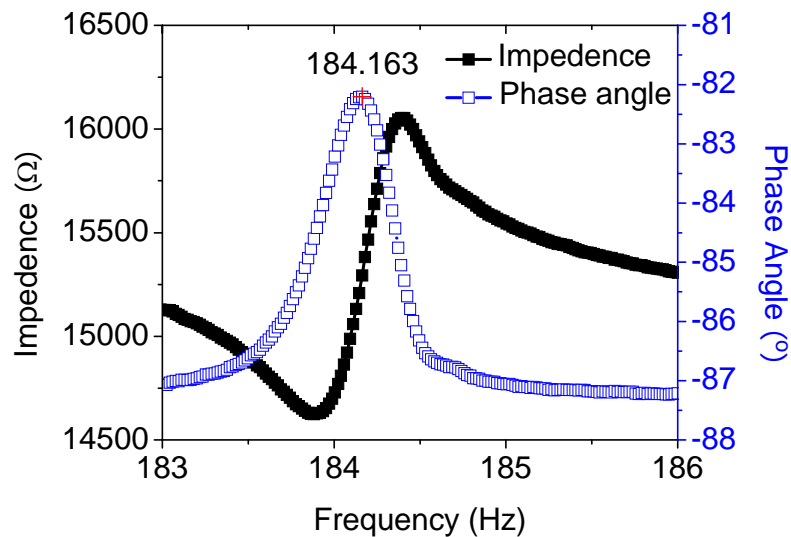
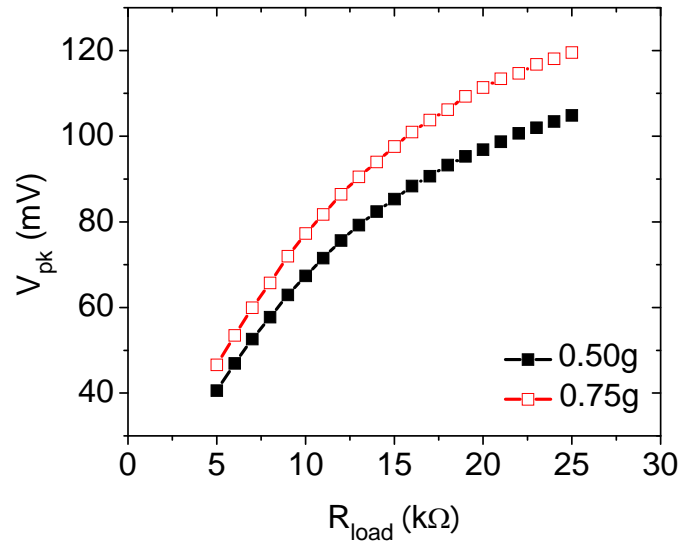


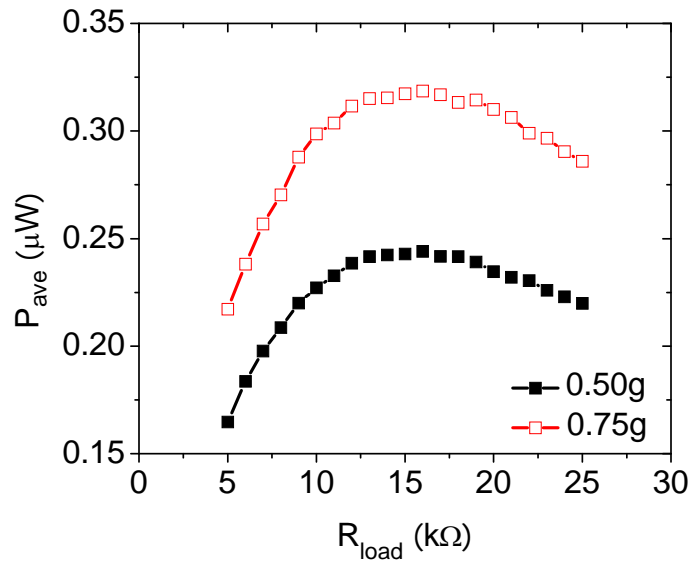
Figure 7- 4 Measured impedance and phase angle of the PZT cantilever vs. frequency.

The Q-factor of this cantilever calculated from the phase angle curve in Figure 7-4 is about 398, which is much higher than the cantilever with the similar dimensions based on a Si wafer reported in Chapter 6. A higher Q-factor device generally has higher amplitude at the resonant frequency, and lower energy loss, which is good for an energy converter. However, a higher Q-factor device also means that its response falls off more rapidly when the frequency deviated from the resonance. This high sensitivity to the vibration frequency is a demerit for energy harvesting devices because a tiny deviation of the vibration frequency from the device's resonant frequency will induce tremendous reduction of the output power. A lower Q-factor will be preferred as long as the output power is high enough to support the application requirements.

The measured peak voltage and the calculated average power versus resistive load at 0.50 g and 0.75 g accelerations and measured corresponding resonant frequencies, 184.0 and 183.8 Hz are shown in Figure 7-5. The peak voltage increases more and more slowly with the increasing resistive load, and the average power therefore appears a maximum value at certain resistive load which is named the optimal resistive load. The measured optimal resistive loads for these two conditions are both 16 k Ω , where the maximum average powers are individually 0.24, and 0.32 μ W, and the corresponding peak voltages are 88, and 101 mV.



(a)

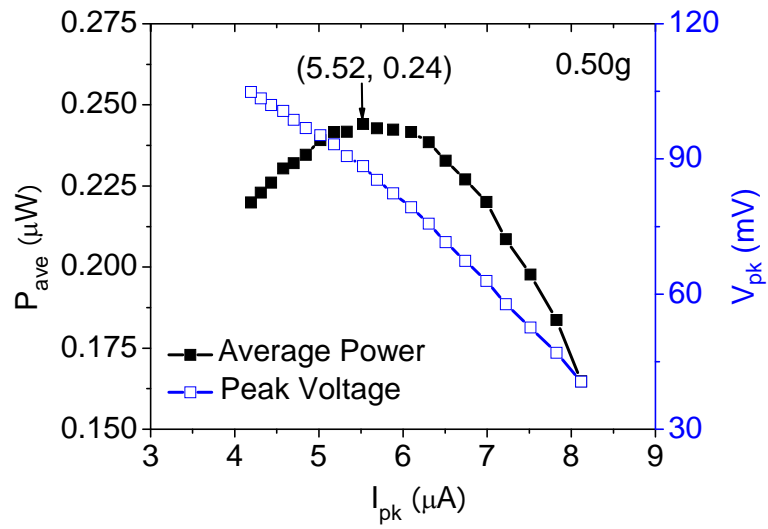


(b)

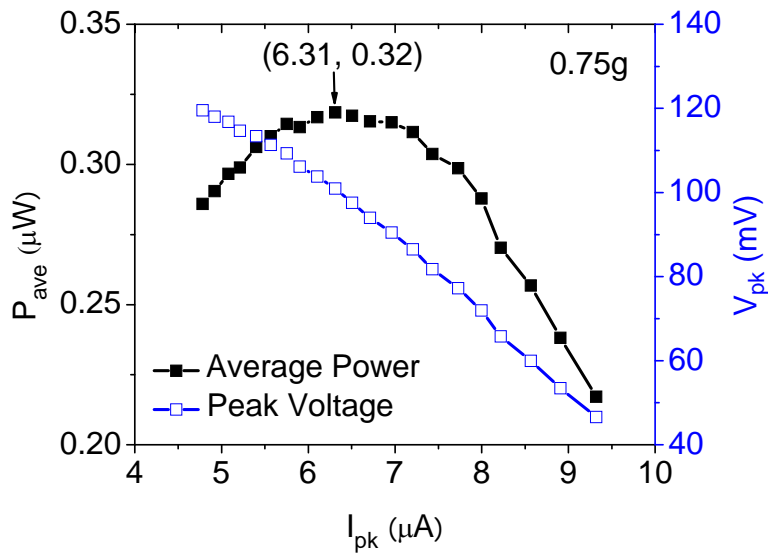
Figure 7- 5 (a) Peak voltage and (b) average power vs. resistive load at 0.50, and 0.75g acceleration amplitudes.

The output current is one of the most important parameters for a power generating device because it is hard to boost up a very low current to an applicable value. The output peak current was then calculated and its relationships with the peak voltage and average power were shown in Figure 7-6. The optimal output peak currents of this device at 0.50g and 0.75g acceleration amplitudes are 5.52, and 6.31 μA . An integrated voltage multiplier could boost up the energy generated by the device to store in a supercapacitor and use to supply power to an electronic device having a short period of activity [3].

Figure 7-7 presents the output voltage amplitude and the average power generated on the optimal resistive load versus the vibration frequency at 0.50, and 0.75g acceleration amplitudes. The Q-factor of the device directly decided the sharpness of the trend curve, that is, the frequency span where the device could be usable. The higher Q-factor of this device comparing with the device reported in Chapter 6 corresponds to a narrower applicable frequency range, but the energy loss of this device is smaller. We can also see that the resonant frequencies, the peak frequencies in Figure 7-7 at 0.50g and 0.75g acceleration amplitudes are respectively 184.0 and 183.8 Hz. The apparent shift of the resonant frequency to lower value with increasing exciting vibration amplitude mainly attribute to the increasing elastic compliance of PZT due to nonlinear effects under large stress [5].

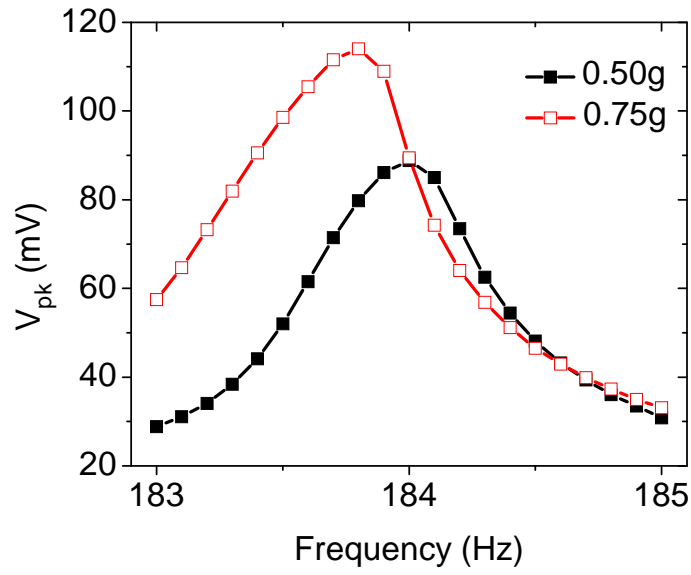


(a)

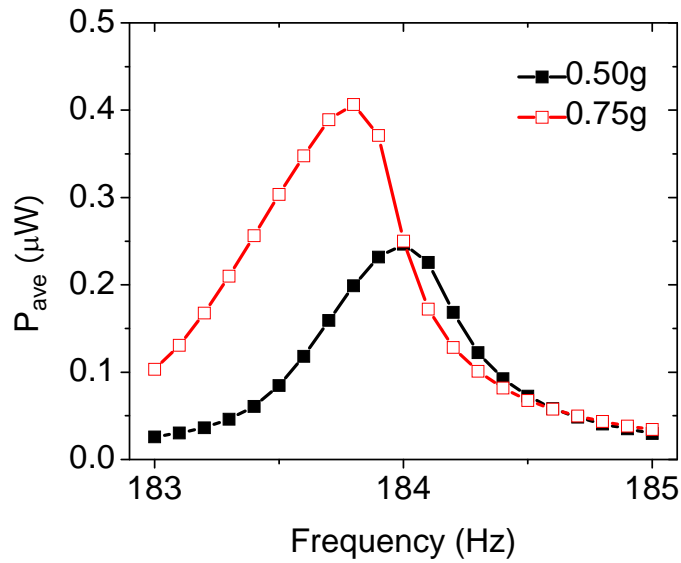


(b)

Figure 7- 6 Peak voltage and average power vs. current at (a) 0.50, and (b) 0.75g acceleration amplitudes.



(a)



(b)

Figure 7- 7 (a) Peak voltage and (b) average power vs. exciting vibration frequency at 0.50, and 0.75g acceleration amplitudes.

7.4 Chapter summary

A MEMS PZT cantilever with an integrated Si proof mass is designed and fabricated on a SOI wafer, and a Pt/PZT/Pt/Ti/SiO₂/Si/SiO₂ multilayer device is generated for low frequency vibration energy harvesting. The integrated Si proof mass at the free end tip of the cantilever is used to decrease the resonant frequency of the device. The SiO₂ layer in the SOI wafer is used to precisely control the thickness of the silicon supporting layer in the cantilever beam because thickness is the most sensitive factor impacting the resonant frequency. The thin film PZT generated by sol-gel has a thickness of around 1.0 μm. The fabricated power generator has a beam dimension of 4800 μm × 400 μm × 22 μm, and a proof mass dimension of around 1415 μm × 1015 μm × 506 μm. The entire effective volume (beam and mass) is about 0.7690 mm³. When excited at 0.75 g ($g = 9.81 \text{ m/s}^2$) acceleration at its resonant frequency of 183.8 Hz, the AC output measured across a resistive load of 16 kΩ connecting to the device in parallel has an amplitude of 101 mV. The calculated average power and power density at the same measurement conditions are respectively 0.32 μW and 416 μW/cm³. The difference in the resonant frequency between the calculated value and the measured one has been decreased to 4.25% due to the precisely controlled thickness of the silicon supporting layer.

References

- [1] S. Roundy, E. S. Leland, J. Baker, E. Carleton, E. Reilly, E. Lai, B. Otis, J. M. Rabaey, P. K. Wright, and V. Sundararajan, "Improving power output for vibration-based energy scavengers," *IEEE Pervasive Computing*, vol. 4, pp. 28-36, 2005.
- [2] S. Roundy, P. K. Wright, and J. Rabaey, "A study of low level vibrations as a power source for wireless sensor nodes," *Computer Communications*, vol. 26, pp. 1131-1144, 2003.
- [3] M. Marzencki, Y. Ammar, and S. Basrour, "Integrated power harvesting system including a MEMS generator and a power management circuit," *Sensors and Actuators A: Physical*, vol. In Press, Corrected Proof.
- [4] M. Renaud, K. Karakaya, T. Sterken, P. Fiorini, C. Van Hoof, and R. Puers, "Fabrication, modelling and characterization of MEMS piezoelectric vibration harvesters," *Sensors and Actuators A: Physical*, vol. In Press, Corrected Proof.
- [5] D. Shen, J.-H. Park, J. Ajitsaria, S.-Y. Choe, H. C. Wickle, and D.-J. Kim, "The design, fabrication and evaluation of a MEMS PZT cantilever with an integrated Si proof mass for vibration energy harvesting," *Journal of Micromechanics and Microengineering*, vol. 18, p. 055017, 2008.
- [6] Y. B. Jeon, R. Sood, J. H. Jeong, and S. G. Kim, "MEMS power generator with transverse mode thin film PZT," *Sensors and Actuators, A: Physical*, vol. 122, pp. 16-22, 2005.

CHAPTER 8

CONCLUSIONS AND FUTURE WORK

8.1 Conclusions

Bimorph PZT power generator in bulk scale was optimized and designed based on commercial PZT-5H bender targeting 100 Hz and above 1g acceleration amplitude vibration environment. The fabricated power generator has dimensions of $25.2 \times 3.2 \times 0.391 \text{ mm}^3$, a end tip proof mass dimensions of $3.2 \times 3.0 \times 3.0 \text{ mm}^3$, and an effective volume of 0.0564 cm^3 . This power generator prototype having an estimated safety factor of 10 can produce $3.1 V_{pk}$, $259 \mu\text{W}$, or $4592 \mu\text{W}/\text{cm}^3$ with an optimal resistive load of $75 \text{ k}\Omega$ from 1g acceleration at its resonant frequency of 97.6 Hz. To overcome the high fragility of PZT, substitute piezoelectric materials (MFC and PVDF) and alternative operational ambient for power generators were investigated for high vibration amplitude applications. MFC- and PVDF-based prototype have been demonstrated the potentials to operate at very high acceleration amplitudes only due to their high strength and lower power output. Vibrating PZT-based cantilever in a denser medium is an option to improve safety factor in the cost of losing power output and also suitable to operating in very high acceleration amplitudes.

Based on literature survey, a multilayer structure in Pt/PZT/Pt/Ti/SiO₂/Si sequence is applied to MEMS-scale piezoelectric cantilever power generator based on a

Si wafer. Silicon is used as the proof mass, and the supporting layer to improve the mechanical strength of the beam. The fabricated device has a beam dimensions about $4.800 \times 0.400 \times 0.036 \text{ mm}^3$ and an integrated Si mass dimensions about $1.360 \times 0.940 \times 0.456 \text{ mm}^3$, which can produce $160 \text{ mV}_{\text{pk}}$, $2.15 \text{ }\mu\text{W}$, or $3272 \text{ }\mu\text{W}/\text{cm}^3$ with the optimal resistive load of $6 \text{ k}\Omega$ from $2g$ ($g = 9.81 \text{ m/s}^2$) acceleration at its resonant frequency of 461.15 Hz . To precisely control the resonant frequency of the power generator, SOI wafer substitutes for Si wafer. The fabricated power generator with the same designed dimensions as the Si wafer based device has a resonant frequency as low as about 170 Hz . The difference between the calculated and measured resonant frequency has been decreased to 4.25% .

8.2 Future work

For MEMS-scale piezoelectric power generators, the lower power output and lower mechanical strength are still the most important issues. Improving power output and safety factor will be the future work.

8.2.1 Power output improvement

The power output of vibration-based power generator is significantly sensitive to the vibration frequency. Most vibration sources have a changing vibration frequency. Design a cantilever array with consecutive resonant frequencies matching the environmental range will make the power generator work effectively all the time, and the

power output will be highly improved. If the power output still not satisfies certain application, cantilever array at each resonant frequency will help to improve it.

It has been proposed that tapered cantilever beam can obtain a constant strain along the cantilever [1]. With this design, the maximum operational strain of PZT can be evenly distributed over the beam length, and more than twice energy could be produced than rectangular cantilever having the same volume of PZT [2].

Composite power generator will be another study direction for improving the power output. For example, a piezoelectric-magnetostrictive composite power generator as described in [3] can produce much higher voltage generation efficiency per generator volume.

8.2.2 Safety factor improvement

As stated in previous section, tapered cantilever has an evenly distributed strain. This will not only increase the power output, but also improve the safety factor by decreasing stress concentration.

Si oil medium proposed in this study has a very high density, and may not suitable for MEMS-scale cantilever power generator application. A less dense insulate medium such as pressed gas chamber could be a better option to low output MEMS-scale cantilever power generators.

References

- [1] N. M. White, P. Glynn-Jones, and S. P. Beeby, "A novel thick-film piezoelectric micro-generator," *Smart Materials and Structures*, vol. 10, pp. 850-852, 2001.
- [2] S. Roundy, E. S. Leland, J. Baker, E. Carleton, E. Reilly, E. Lai, B. Otis, J. M. Rabaey, P. K. Wright, and V. Sundararajan, "Improving power output for vibration-based energy scavengers," *IEEE Pervasive Computing*, vol. 4, pp. 28-36, 2005.
- [3] A. Bayrashev, W. P. Robbins, and B. Ziaie, "Low frequency wireless powering of microsystems using piezoelectric-magnetostrictive laminate composites," *Sensors and Actuators A: Physical*, vol. 114, pp. 244-249, 2004.

APPENDIX A

Table A.1: the 1st generation design

w_p (μm)	l_p (μm)	w_m (μm)	h_m (μm)	l_m (μm)	f_r (Hz)
100	900	100	500	300	97
	1200	0	0	0	1022
	500	100	500	500	99
	1000	0	0	0	1472
	900	200	500	200	96
	1100	0	0	0	1216
500	500	500	500	500	99
	1000	0	0	0	1472
	1900	1000	500	1000	10
	2900	0	0	0	175
	300	1000	500	2000	10
	2300	0	0	0	278
	1300	2000	500	1000	10
1000	750	500	500	500	99
	1250	0	0	0	942
	1700	1000	500	1500	10
	3200	0	0	0	144
	900	1000	500	2000	10
	2900	0	0	0	175
	2200	1500	500	1000	10
	1300	1500	500	1500	10
	2800	0	0	0	188

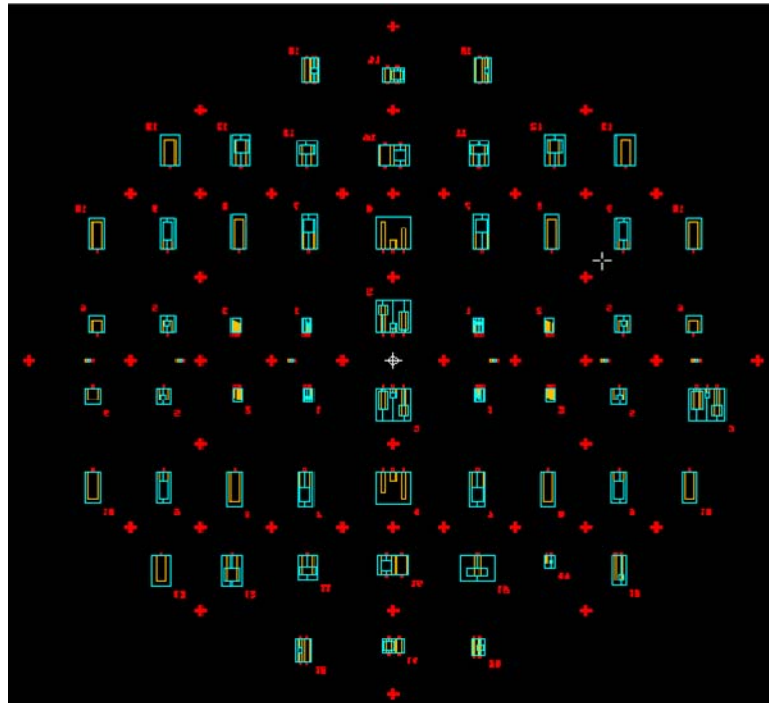
Table A.2: The 2nd design (rectangular cantilever)

w_p (μm)	l_p (μm)	l (μm)	w_m (μm)	h_m (μm)	l_m (μm)	f_r (Hz)
500	2100	4100	2000	500	2000	99
	2600	4600				83
	3100	5100				71
	3400	4900	1500	500	1500	101
	4100	5600				82
	4800	6300				69
	2500	4500	1500	500	2000	99
	3100	5100				82
	3700	5700				70
1000	3200	5200	2000	500	2000	98
	3800	5800				83
	4400	6400				71
	2000	4500	2500	500	2500	97
	2500	5000				83
	3000	5500				72
	1600	4600	2000	500	3000	96
	2100	5100				82
	2600	5600				71
	2000	5000	1500	500	3000	97
	2600	5600				82
	3200	6200				70
	2600	5600	1000	500	3000	100
	3300	6300				83
	4000	7000				71

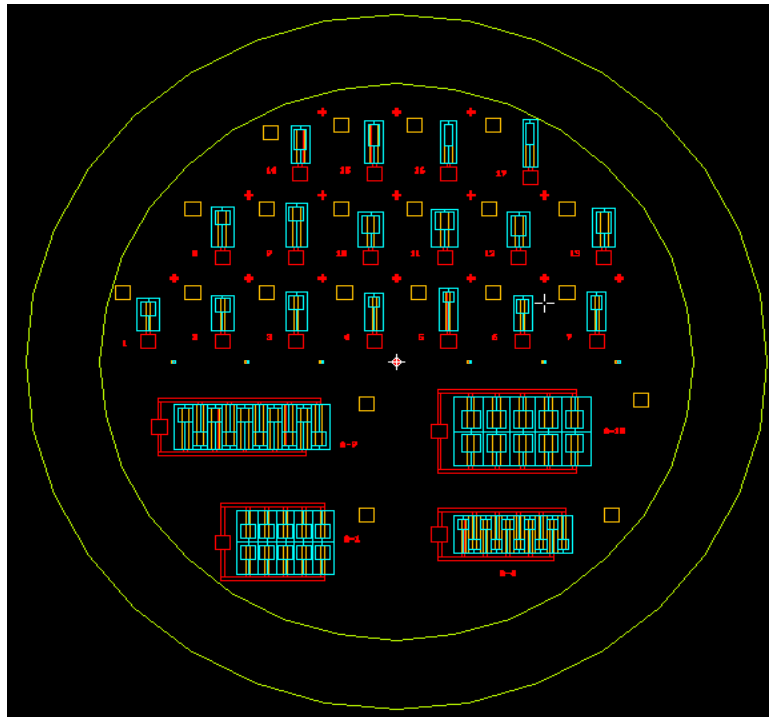
Table A.3: The 3rd design

w_p (μm)	l_p (μm)	l_m (μm)	l (μm)	w_m (μm)	h_m (μm)	f_r (Hz)
400	4100	1200	5300	1200	500	100
	3200	1600	4800	1200	500	101
	2800	1600	4400	1600	500	100
300	3600	1200	4800	1200	500	101
	4100	1200	5300	900	500	100
	2700	1500	4200	1500	500	99
	2900	1500	4400	1300	500	99
	3100	1500	4600	1100	500	100
200	4700	800	5500	800	500	100
	3800	1000	4800	1000	500	99
	4100	1000	5100	800	500	101
	3000	1200	4200	1200	500	101

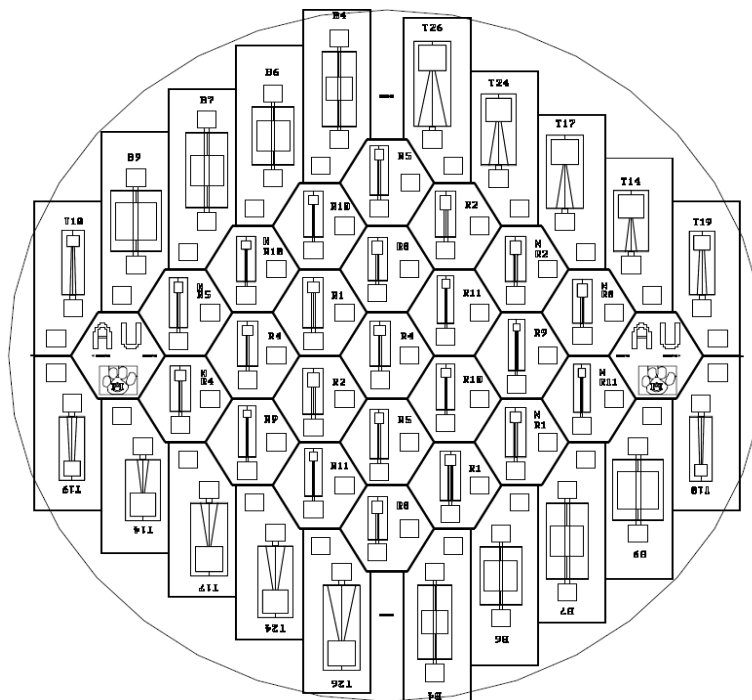
APPENDIX B



Mask of the 1st generation design

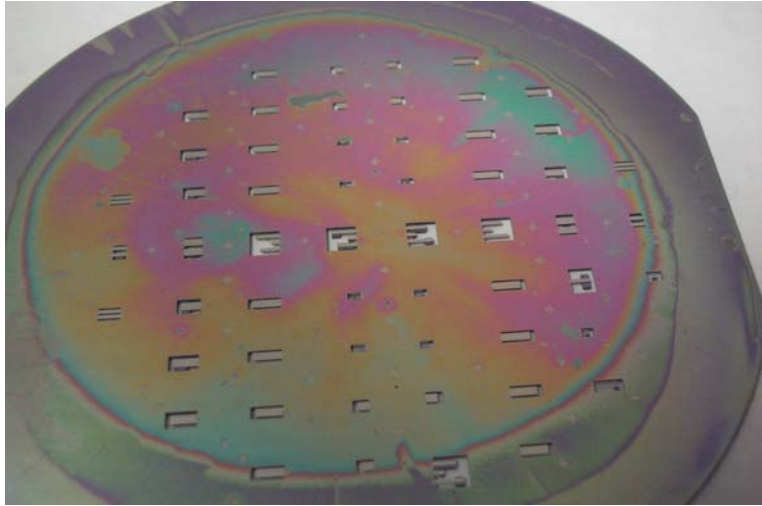


Mask of the 2nd generation design

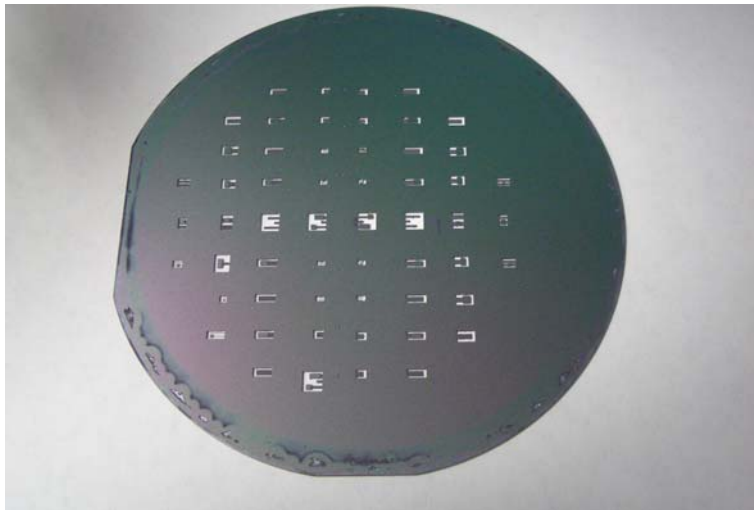


Mask of the 3rd generation design

APPENDIX C



(a)



(b)

Pictures of the fabricated wafer: (a) front view and (b) back view.